Bose-Einstein Condensation in Microtraps on Videotape

Christopher David James Sinclair

Thesis submitted in partial fulfilment of the requirements for the degree of Doctor of Philosophy of the University of London and the Diploma of Membership of Imperial College.

Imperial College London

University of London

December 2005

Abstract

Bose-Einstein Condensation in Microtraps on Videotape

C. D. J. Sinclair

The preparation of the first Bose-Einstein condensate in a permanently-magnetised microtrap is described. A piece of videotape is recorded with a 100 μm pitch magnetic pattern. By applying an external magnetic bias field a long guide is formed whose ends are closed with the field of two wires perpendicular to the guide.

Rubidium-87 atoms are loaded from a low-velocity intense source into a magneto-optical trap formed close to the surface of the videotape. The atoms are captured by the magnetic field of a current-carrying wire and loaded into one of the videotape microtraps where they are cooled to quantum degeneracy by radio-frequency evaporation.

Ultracold atoms trapped by the videotape are used to measure the homogeneity of the confining potential. In addition, the lifetimes for atoms to remain trapped near the videotape surface are measured and found to be long compared with those reported close to metallic wires. The observed reduction in lifetime as the surface is approached is in good agreement with a recent model of thermally induced spin relaxation due to a thin gold layer on the videotape surface.

Acknowledgements

First, thanks to my principle investigator Ed Hinds for his excellent supervision. I have learned much from his approach to all aspects of physics and his enthusiasm and patience make him the ideal supervisor.

Thanks to Anne Curtis for her constantly cheerful nature and optimistic outlook that make working in the lab all the more pleasant and for providing continued encouragement during the latter stages.

Thanks to Brenton Hall, who I worked with during the first 18 months, for his dedication to the experiment and for sharing his sizeable experience.

Thanks to Isabel Llorente-García for all her hard work on various aspects of the experiment during her first year.

Thanks to Ben Sauer, Stefan Eriksson and Fernando Ramírez-Martínez for assistance in the lab and to Jony Hudson for computing advice. Thanks to Jon Dyne for his outstanding mechanical skills and to Bandu Ratnasekara for electronics support. Thanks also to Jocelyn Retter.

All of the members of CCM past and present make it a fun place to work - and there are now more than can reasonably be listed! Special mention in particular must go to Paul Condylis and Daniel Sahagún Sánchez with whom I have shared various houses, labs, offices and their good company from day one.

Finally, thanks to all family and friends for their encouragement and support throughout.

Contents

1 Introduction **11**

1.1 Experimental Approach 13

1.2 Outline of the Thesis 14

2 Background Material **15**

2.1 The Stern-Gerlach Force 15

2.2 Permanent Magnetic Microtraps 17

2.2.1 A Periodically Magnetised Thin Film 17

2.2.2 Producing Microscopic Magnetic Waveguides 19

2.2.3 Confinement in the Z-Direction 21

2.3 Bose-Einstein Condensation 22

2.3.1 Phase Space Density 22

2.3.2 Degeneracy in a Non-Interacting Bose Gas 22

2.3.3 The Weakly Interacting Condensate 24

2.4 Condensate Expansion 26

2.5 Summary 27

3 Experimental Apparatus **28**

3.1 Lasers and Optics 28

3.1.1 Diode Lasers 28

3.1.2 Doppler-Free Spectroscopy 29

3.1.3 The Reference Laser 30

3.1.4 High Power Tapered Amplifier Laser 30

3.1.5 The Frequency Offset Lock 32

3.1.6 Repump Lasers 34

3.1.7 AOMs and Fibre Coupling 36

3.2 The Ultrahigh Vacuum System 38

3.2.1 The Main Vacuum Chamber 39

3.3 Computer Control 40

3.3.1 Control Hardware 41

3.3.2 Structure of the Control Software 42

3.3.3 Graphical User Interface . . . 43
3.3.4 Synchronisation with Imaging Software . . . 43
3.3.5 Computer Control of RF Evaporative Cooling . . . 45
3.4 The Videotape Atom Chip . . . 46
3.5 Generation of Magnetic Fields . . . 48
3.5.1 Magnetic Field Coils . . . 48
3.5.2 Magnetic Field Control . . . 48
3.6 Absorption Imaging . . . 49
3.6.1 Imaging System . . . 50
3.6.2 Double Imaging Technique . . . 51
3.7 Summary . . . 53

4 Low Velocity Atom Source for a Mirror-MOT 54
4.1 Laser Cooling . . . 54
4.1.1 Slow Atomic Beams . . . 55
4.2 The Low Velocity Intense Source of Atoms (LVIS) . . . 56
4.2.1 The LVIS Vacuum System . . . 57
4.2.2 LVIS Extraction Mirror . . . 57
4.2.3 Pressure Differential . . . 59
4.2.4 Low Conductance Aperture By-Pass . . . 60
4.2.5 LVIS Magnetic Fields . . . 61
4.2.6 The LVIS Atom Source . . . 61
4.2.7 Operation and Testing of the LVIS . . . 62
4.2.8 Beam Divergence . . . 63
4.3 The Mirror MOT . . . 65
4.3.1 The Mirror-MOT in Practise . . . 65
4.3.2 Fluorescence Measurements . . . 66
4.3.3 Loading the Mirror-MOT from the LVIS . . . 66
4.3.4 Mirror-MOT Lifetime . . . 68
4.4 The Mirror-MOT Temperature . . . 68
4.4.1 Sub-Doppler Cooling . . . 70
4.5 Moving the Mirror-MOT Closer to the Surface . . . 72
4.6 Summary . . . 72

5 Loading a Videotape Microtrap 74
5.1 The Atom Chip Wire Trap . . . 74
5.1.1 Temperature of a Thermal Cloud . . . 76
5.2 Optical Pumping . . . 77
5.2.1 Optical Pumping Timing Sequence . . . 77
5.3 Recapture in a Magnetic Trap . . . 78

5.4 Evaporative Cooling Background . . . 83
5.4.1 Collision Rates and Evaporation Timescales . . . 83
5.4.2 Forced RF Evaporative Cooling . . . 84
5.5 Compression of the Magnetic Trap . . . 84
5.5.1 Determination of the Centre Wire Position . . . 89
5.6 Evaporative Cooling in the Compressed Magnetic Trap . . . 90
5.7 Transfer into a Videotape Microtrap . . . 91

6 Microtrap Properties and BEC **95**
6.0.1 Measurement of the Surface Field . . . 95
6.0.2 Probing the Videotape Trap Frequencies . . . 96
6.1 Axial Confinement in the Videotape Microtraps . . . 101
6.1.1 The Influence of Gravity on the Axial Field Gradient . . . 101
6.1.2 The Axial Confining Potential . . . 103
6.2 Bose-Einstein Condensation . . . 104
6.2.1 Evaporation and Detection . . . 104
6.2.2 Free Expansion of the Condensate . . . 105
6.3 Condensate Properties . . . 106
6.3.1 Data Processing . . . 106
6.3.2 Comparison with Theory . . . 108
6.3.3 Condensate Properties . . . 110
6.4 Discussion . . . 111

7 Atom-Surface Effects **112**
7.1 Part 1: Fragmentation . . . 112
7.1.1 Observation of Fragmentation . . . 113
7.1.2 Obtaining the Fragmentation Potential . . . 114
7.1.3 Depth of the Videotape Fragmentation Potential . . . 115
7.1.4 Surface Quality of the Videotape Material . . . 115
7.1.5 Origin of the Videotape Fragmentation . . . 117
7.1.6 Discussion . . . 121
7.2 Part 2: Spin-Flip Lifetime near the Surface . . . 122
7.2.1 Thermal Fluctuations and Spin-Flips . . . 122
7.2.2 Loss Mechanism . . . 123
7.2.3 Experimental Measurements Close to Videotape . . . 124
7.2.4 Technical Noise . . . 126
7.2.5 Adjusting the Axial Bias Field . . . 127
7.2.6 Evaporation Losses at Low Trap Depth . . . 129
7.2.7 Comparison with Theory for Thermal Spin-Flips . . . 130
7.3 Conclusion . . . 132

8 Conclusions and Outlook **134**
8.1 Conclusion 134
8.2 Future Directions 135

A Rubidium Structure **137**

B Achieving Ultra-High Vacuum **138**

Bibliography **141**

List of Figures

2.1 Zeeman shifts for the ground state of ^{87}Rb. 16
2.2 A periodically magnetised thin film. 18
2.3 Contours of constant magnetic field above the magnetised surface. 20
2.4 Cross-sections in x and y of the videotape field magnitude. 20
2.5 Videotape field magnitude cross sections with an added axial field. 21
2.6 The z-component of magnetic field above two wires. 22

3.1 Polarisation spectroscopy set-up. 30
3.2 Polarisation spectrum of the ^{87}Rb $F = 2 \rightarrow F'$ transition. 31
3.3 The principal components of the tapered amplifier diode laser. 31
3.4 Schematic of the offset lock. 33
3.5 Optical arrangement for the repump light. 35
3.6 Polarisation spectrum of the ^{87}Rb $F = 1 \rightarrow F'$ transition. 36
3.7 Overview of the fibre coupling system and repump combination optics. 37
3.8 Photograph of the main vacuum chamber. 39
3.9 Schematic of the control hardware. 42
3.10 A screen-shot of the user-interface. 44
3.11 The face of the videotape atom chip 47
3.12 Schematic cross-section through the atom chip. 47
3.13 FET control circuit diagram 48
3.14 Schematic diagram of the imaging arrangement. 51
3.15 Schematic diagram of the reflection imaging technique. 52

4.1 The operating principle of the LVIS. 56
4.2 A schematic diagram of the LVIS construction. 58
4.3 Cross-section of the LVIS mirror assembly. 59
4.4 Cross-section illustrating the aperture by-pass. 60
4.5 Demonstration of the effect of LVIS misalignment. 64
4.6 Schematic of a mirror-MOT. 65
4.7 Loading the mirror-MOT from the LVIS. 67
4.8 An image of the mirror-MOT fluorescence. 68

4.9 Decay curve of the mirror-MOT. 69
4.10 Ballistic expansion of the Mirror-MOT. 70
4.11 Number and temperature dependencies of mirror-MOT cooling. 71
4.12 Ballistic expansion of the cooled Mirror-MOT. 72

5.1 Magnetic field lines of a current-carrying wire plus bias field. 75
5.2 Magnetic field strengths of the wire + bias guide for $I = 15\,\mathrm{A}$ and $B_x = 20\,\mathrm{G}$. . 76
5.3 Timing sequence of the optical pumping stage. 79
5.4 Potential of the wire trap used to recapture the MOT. 80
5.5 Radial centre-of-mass oscillations in the re-capture trap. 81
5.6 Axial centre-of-mass oscillations in the re-capture magnetic trap. 82
5.7 Absorption image of a cloud recaptured in the magnetic trap. 82
5.8 Timing sequence for magnetic trap compression. 85
5.9 Magnetic potential of the compressed trap. 86
5.10 Absorption image of a compressed magnetic trap. 86
5.11 Radial profile of a compressed magnetic trap. 88
5.12 Contours of constant field in the compressed magnetic trap. 88
5.13 The height at which the magnetic trap forms *vs* current in the wire. 89
5.14 Absorption images of the compressed magnetic trap during evaporative cooling. 91
5.15 Timing sequence for transfer into a videotape microtrap. 92
5.16 Magnetic field contours during transfer into a videotape microtrap. 93

6.1 Dependence of videotape trap height on the bias field. 96
6.2 Response of the cloud temperature to a time-dependent modulation. 98
6.3 Measured microtrap radial frequency *vs* bias field. 99
6.4 Deviation of the microtrap transverse potential from a harmonic oscillator. . . 100
6.5 Schematic illustration of the effect of a slightly tilted atom chip. 102
6.6 Position of the cloud during expansion in a waveguide. 102
6.7 Oscillation of a $1\,\mu$K thermal cloud in the axial potential. 104
6.8 Absorption images during evaporative cooling in the microtrap. 105
6.9 Free expansion of a thermal cloud and partial condensates. 106
6.10 Axial profiles of bimodal distributions during condensate formation. 109

7.1 Fragmentation of a thermal cloud as the temperature is lowered. 114
7.2 Fragmentation potentials for three different distances from the videotape. . . . 116
7.3 Fragmentation potential of a 250 nK cloud. 116
7.4 Atomic force microscope scan of a sample of videotape. 117
7.5 Cross sections through videotape AFM scans. 118
7.6 The z component of the magnetic field plotted above a circular recess. 119
7.7 Collective B_z field plotted for increasing distance. 120
7.8 An example of a lifetime measurement. 125

7.9 The lifetime of atoms trapped in a videotape microtrap *vs* height. 126
7.10 Lifetime of atoms in a videotape trap with a 12 G axial field. 128
7.11 Temperature as a function of the applied axial bias field. 129
7.12 Temperature in the trap versus hold time. 130
7.13 Comparison of measured lifetimes with the thermal spin-flip theory. 132

List of Tables

1 Some physical constants of use. 10

3.1 Table summarising the control hardware 41
3.2 CCD Camera chips 51

4.1 A table summarising some reported LVIS set-ups. 63

6.1 Condensate properties 110

7.1 Comparison between reports of $\Delta B/B$ 121

Quantity	Symbol	Value
Bohr Magneton	μ_B	$9.27 \times 10^{-24}\,\mathrm{Am}^2$
Plank constant	h	$6.63 \times 10^{-34}\,\mathrm{Js}$
Reduced Plank constant	$\hbar$	$1.05 \times 10^{-34}\,\mathrm{Js}$
Permeability of Vacuum	μ_0	$4\pi \times 10^{-7}\,\mathrm{NA}^{-2}$
Boltzmann constant	k_B	$1.38 \times 10^{-23}\,\mathrm{JK}^{-1}$
Bohr radius	a_0	$0.53 \times 10^{-10}\,\mathrm{m}$
Atomic Mass Unit	amu	$1.66 \times 10^{-27}\,\mathrm{kg}$

Table 1: Some physical constants of use [1].

Chapter 1

Introduction

The ability of atomic physicists to precisely control matter has undergone a revolution in recent times, largely driven by the development of laser cooling and trapping. Perhaps most significantly, this led directly to the first realisation of Bose-Einstein condensates (BEC) in 1995 [2–4], representing an important milestone and bringing the everyday and the quantum worlds closer together. The study of BEC has since proliferated into a vast field, stimulating developments in areas such as atom interferometry [5], atom lasers [6], precision measurements [7] and degenerate Fermi gases [8] to name only a few.

At the low energies achieved in laser cooling and BECs, the wavelike nature of atoms becomes significant, leading to the field of atom optics in which de Broglie matter waves are manipulated with atom optical elements in analogy with the manipulation of light waves in classical optics. Many components for atom optics have now been implemented [9] including mirrors, lenses, beam-splitters, and gratings for cold atoms. The possibility of miniaturising and integrating such components onto a common substrate leads naturally to the idea of an 'atom chip' which might combine sources of matter waves with components that manipulate and guide them round tiny quantum circuits, much like electrons on a silicon microchip [10]. Magnetic and optical forces are very well suited for trapping and manipulating the magnetic or electric dipole moment of neutral atoms and the required field sources can be integrated onto the substrate. Such a device might form the basis of a quantum computer if individual atoms could be suitably controlled and made to interact with each other [11] or coupled to the light field of miniature cavities on the chip [12]. Atom interferometers capable of making measurements of small perturbations with exquisite sensitivity might also be fashioned from an atom chip [13, 14].

Magnetic field sources on atom chips are usually microscopic conducting elements patterned onto the surface, creating complex magnetic potentials by controlling the path of electric currents [15]. This technology benefits from the established fabrication techniques developed in the microchip industry. The resulting magnetic traps and guides offer high magnetic field gradients and curvatures, permitting tight confinement of atom clouds within a few micrometers of the substrate surface and elaborate potential shapes such as adjustable double-wells for

interferometry.

Combining the compact and versatile nature of atom chips with Bose-Einstein condensates as a coherent source of matter waves is therefore a natural progression. BEC was first produced on micro-fabricated atom chips by two groups in Germany in 2001 [16, 17]. Since then many other chip condensates have followed [18–24] and these have been accompanied by reports of many interesting developments including, among others, atom conveyor belts [25], studies of non-linear dynamics [26], and even BEC in a portable vacuum cell [24]. It has also been shown that miniature-scale atomic clocks [27] and magnetometers [28] can be constructed, further adding to the toolbox of devices for miniature atom optics. Advances towards interferometry have also followed, including the realisation of a Michelson interferometer on a chip [23] and recently the splitting of a BEC in a controlled manner [29].

The task of developing atom chips into practical working devices involves not only the implementation of the underlying ideas but also, critically, dealing with the numerous inevitable experimental challenges encountered along the way, both technical and fundamental in origin. For instance, a number of effects that are apparently unique to atom chips have been widely observed, including reduced trap lifetimes close to the surface [19–21, 30, 31], fragmentation of condensates and thermal clouds into lumps [20, 22, 30, 32–34] and increased heating rates [16]. The presence of fragmentation has been attributed to field components in the potential produced by deviating current paths in the conductors, an effect that could possibly be reduced by refinement of the manufacturing process. The observed reduction in lifetime in the vicinity of the surface has been predicted [35], and shown, [31, 36] to be caused by atomic spin relaxation induced by near field radiation due to thermal fluctuations in the bulk of the conducting material. This latter effect is more fundamental in origin than the technical artifact of fragmentation but can reduce trap lifetimes to just hundreds of milliseconds within $10\,\mu$m of a typical micro-fabricated conductor. Both fragmentation and spin-flip loss mean that it is necessary to work far from the surface if these effects are to be minimised, preventing full exploitation of the available tight confinement and intricate potentials. However, from another perspective, it is conceivable that these effects could be reduced or eliminated if currents and conductors could be discarded completely. Clearly atom chips based on microscopic conductors are powerful devices but not without some notable drawbacks.

To further develop atom chips in way that might transcend some of the wire-based chip limitations, one could easily conceive of borrowing from the field of permanent magnet materials, which have already played a major role in manipulating cold atoms. For example, magnetic mirrors for cold atoms have previously been demonstrated using audio tape [37], floppy disk [38,39], videotape [40–42], hard disk [43] and magneto-optical film [44]. Cold atoms dropped onto the mirror are reflected due to the interaction of the atoms magnetic dipole moment with the large magnetic field gradients present near the surface and focussed to a spot over centimeter distances. It is possible to harness these same magnetic field gradients to form guides and traps for cold atoms on the scale of microns [45]. For example, a piece of videotape periodically magnetised in-plane can be adapted to produce an array of waveguides for cold atoms simply

with the addition of a uniform magnetic field. This is significant because permanently magnetised materials contain no real currents that might deviate from their intended path and do not necessarily contain large amounts of conducting materials, immediately highlighting the possible suitability for their use on atom chips.

There are other notable advantages motivating the use of permanent magnets on atom chips based on more positive reasoning. There is no power dissipation in a permanent magnet and the formation of the traps themselves are greatly simplified, removing the need to control currents in conductors. Many individual traps can be written onto a small area making the system easily scalable. Significantly, the confinement can be very tight indeed, providing transverse oscillation frequencies of many tens or hundreds of kilohertz, making investigations of low-dimensional systems possible, including the regime of fluctuating phase, 1D condensates and even Tonks gases [46].

In an attempt to take advantage of these benefits, permanent magnetic materials have now been incorporated onto atom chips. The first demonstration of trapping in this way was performed with videotape [47, 48]. In addition, cold atoms have since been loaded into traps formed by FePt film [49] and multi-layer magneto-optical film [50]. In Ref. [49] spark erosion is used to to produce magnetic patterns with both in plane and out-of-plane magnetisation. The approach in Ref. [50] is to uniformly magnetise a TbGdFeCo multi-layer film and produce a magnetic trap along the edge of the film by applying a uniform magnetic field.

Videotape provides the basis for the magnetic traps described in this thesis. Videotape has consistently proved very successful as a material for atom optics, not only for its favourable magnetic properties and ease of recording but also for more specific reasons such as its compatibility with ultra-high vacuum [51].

Just as conducting atom micro-chips have advanced to the point of making Bose-Einstein condensates, it is also a natural progression to combine miniature permanent magnetic materials with BEC to determine their ongoing suitability for atom chips and as a further means of establishing their place in atom optics. Bose-Einstein condensates have now been achieved in two types of permanent-magnet microtraps, those based on videotape [52] and on a TbGdFeCo film [50,53]. The production of the first Bose-Einstein condensate on a permanently magnetised atom chip is the subject of this thesis.

1.1 Experimental Approach

The approach to producing BEC adopted in this work has many aspects in common with other BEC experiments, involving stages of laser cooling, magnetic trapping and evaporative cooling. The central element of the magnetic trapping stage is the array of microtraps formed on periodically magnetised videotape by the application of a uniform bias field. Trapping sufficiently many atoms at high initial phase space density to produce BEC in the small volume microtraps that form close to the surface involves tackling some specific experimental considerations, building on the original demonstration of magnetic trapping with videotape [47]. The atom chip

used in these experiments was constructed for the work in [47], carried out at the University of Sussex.

The experimental strategy is to begin with a large sample of laser-cooled rubidium-87 atoms, trapped a few millimeters from the atom-chip surface. A low velocity source of atoms, spatially separated from the main atom-chip vacuum chamber, permits large loading fluxes and ultra high vacuum. The atoms are then loaded from the magneto-optical trap into a purely magnetic trap formed by a macroscopic current-carrying wire mounted behind the atom chip. This trap is compressed and a stage of rf evaporative cooling is performed. The pre-cooled cloud is then loaded into a videotape microtrap by manipulating the external fields while the current in the wire is reduced to zero. Once in the videotape microtrap, further rf evaporation cools the cloud to BEC.

The ability to achieve ultracold temperatures and excellent vacuum-limited lifetimes also allows the magnetic field homogeneity to be probed with good sensitivity using cold atoms and allows the lifetime of trapped atoms to be investigated with good resolution for the first time. These are both important tasks for establishing the long term suitability of videotape for atom chip experiments.

1.2 Outline of the Thesis

This rest of this thesis is structured as follows. Chapter 2 contains some background material, providing an introduction to the videotape microtraps and a brief description of Bose-Einstein condensation. The experimental apparatus is then described in Chapter 3, which includes details of the laser system, vacuum system and computer control. Chapter 4 then concerns the low velocity intense source of atoms that was constructed to load a mirror-MOT. Chapter 5 concerns capturing the atoms in a wire-based magnetic trap, cooling them and loading them into a videotape microtrap. This is followed by a determination of the properties of the videotape microtraps, the realisation of BEC and consideration of the condensate properties in Chapter 6. An investigation into the homogeneity of the videotape waveguides and the trap lifetime near the atom chip surface follows in Chapter 7. Finally, Chapter 8 concludes the thesis with a summary and a discussion of ideas for future work.

Chapter 2

Background Material

2.1 The Stern-Gerlach Force

Neutral atoms with a magnetic moment can be trapped and guided by static magnetic field gradients. At the ultracold temperatures achieved by laser cooling and evaporative cooling, the energy shifts due the interaction of an atomic magnetic moment with a modest magnetic field are sufficient to compete with the thermal kinetic energy. For example, a magnetic field of 10 G is energetically equivalent to 670 μK for ^{87}Rb. Alkali metals are well suited to magnetic trapping due to the large magnetic moment of the unpaired electron. The ground state Hamiltonian of an alkali atom with total electronic angular momentum **J** and total nuclear angular momentum **I** can be written as

$$\hat{H} = \frac{A_{\mathrm{hfs}}}{I+\frac{1}{2}}\mathbf{I}\cdot\mathbf{J} - \boldsymbol{\mu}\cdot\mathbf{B} \tag{2.1}$$

where the first term represents the ground state hyperfine interaction with ground state splitting A_{hfs} and the second term represents the interaction of the atomic magnetic moment $\boldsymbol{\mu}$ with an external magnetic field **B**. The atomic magnetic moment has contributions from both the nuclear and electronic momentum

$$\boldsymbol{\mu} = -(g_I\mu_I\mathbf{I} + g_J\mu_B\mathbf{J}) \tag{2.2}$$

where g_I and g_J are the nuclear and electronic Landé g-factors and μ_B is the Bohr magneton. For the ground state of ^{87}Rb, $g_J = 2$. In the case of zero orbital angular momentum the energy shift due to an external field can be conveniently expressed by the Breit-Rabi formula [54]

$$E = -\frac{A_{\mathrm{hfs}}}{2(2I+1)} + (-1)^F \times \frac{1}{2}A_{\mathrm{hfs}}\sqrt{1+\frac{4m_F}{2I+1}x+x^2} \tag{2.3}$$

where

$$x = \frac{(g_I+g_S)\mu_B B}{A_{\mathrm{hfs}}} \tag{2.4}$$

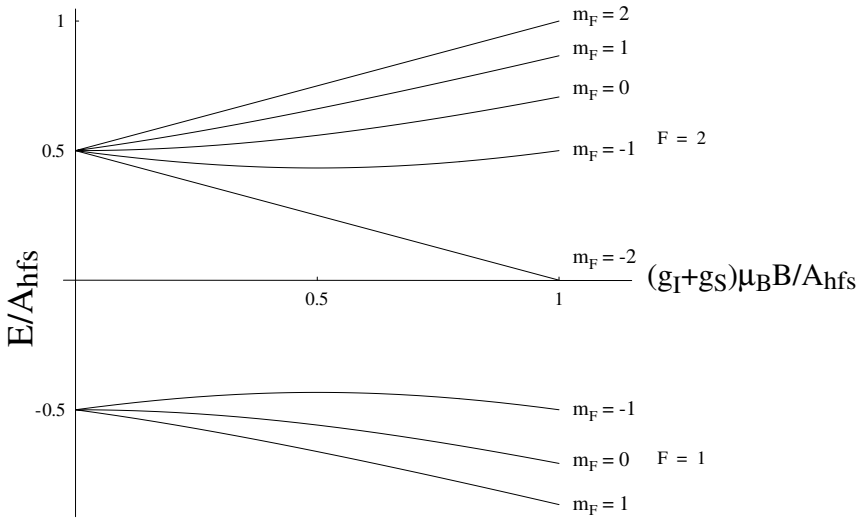

Figure 2.1: The Breit-Rabi diagram showing the Zeeman shift for the ground state of ^{87}Rb normalised to the hyperfine splitting. The sub-levels are labelled according to their m_F number in low field where the splitting is linear.

The Breit-Rabi formula describes the Zeeman shift of the ground state of rubidium in which $J = S = \frac{1}{2}$. The level splitting is shown in Figure 2.1. In low magnetic field ($\lesssim 300\,\mathrm{G}$) the Zeeman shift is linear and Equation 2.3 simplifies to

$$\Delta E = m_F g_F \mu_B |B|, \tag{2.5}$$

where we denote the energy shift relative to the zero field ground state by ΔE. In Equation 2.5 the g_F term is an effective g-factor given by

$$g_F = \frac{g_J(F(F+1) + J(J+1) - I(I+1) + \frac{\mu_N}{\mu_B} g_I(F(F+1) - J(J+1) + I(I+1))}{2F(F+1)} \tag{2.6}$$

Since $\mu_N \ll \mu_B$ the second term can be neglected and g_F becomes $\pm\frac{1}{2}$ for the $F = 2$ and $F = 1$ ground states of ^{87}Rb.

It can also be seen from Figure 2.1 that it possible to distinguish between states for which the energy is raised in the presence of a small magnetic field and those for which the energy is lowered. States for which the energy is raised are known as 'weak field seeking' states and will be attracted to a magnetic field minimum. The $|F, m_F\rangle = |2, 2\rangle$, $|2, 1\rangle$ and $|1, -1\rangle$ states are weak-field seeking states of ^{87}Rb and can be magnetically trapped. The most strongly interacting of these is the $|2, 2\rangle$ state, which has a moment one Bohr magneton and is the state primarily used in the experiments in this thesis.

The force responsible for attracting weak field seeking atoms to a magnetic field minimum

is proportional to the magnetic field gradient since,

$$\mathbf{F} = -\boldsymbol{\nabla} E = -g_F m_F \mu_B \boldsymbol{\nabla} |\mathbf{B}| \tag{2.7}$$

and is known as the Stern-Gerlach force. The modulus of the magnetic field therefore defines a potential in the frame of an atom.

In order to preserve the spin state in a magnetic trap the total magnetic field must not go to zero. Regions of low or zero magnetic field are unsuitable for manipulating cold atoms in practice since an atom can undergo a Majorana spin-flip into an un-trapped state and become lost from the trap. The adiabatic condition requires that the rate of change of the field direction, θ, must be slower than the precession frequency of the magnetic moment, the Larmor frequency ω_L [55]:

$$\frac{d\theta}{dt} < \omega_L = \frac{\mu_\zeta B}{\hbar}, \tag{2.8}$$

where μ_ζ is the magnetic moment. The inequality in Equation 2.8 is violated in regions of low magnetic field. This condition must be considered when constructing potentials for magnetic trapping to ensure that the Majorana spin-flip rate is not a limiting factor on the trap lifetime.

2.2 Permanent Magnetic Microtraps

In the previous section it was shown that the interaction of the intrinsic magnetic moment of an atom induces a linear shift of its energy in small magnetic fields and that there exist states of ^{87}Rb that are attracted to regions of low magnetic field. Provided the spin adiabatically follows the field an atom in these sates can be confined in a magnetic trap by the Stern-Gerlach force. In the following section, a specific realisation of magnetic confinement will be described, that of a microscopic magnetic waveguide formed by a periodically magnetised thin film.

2.2.1 A Periodically Magnetised Thin Film

The form of the spatially varying magnetic field produced by thin magnetised film such as videotape will be presented here. The presentation follows methods given in References [39, 45] and [9].

Consider a sample of thickness b, magnetised in the x-direction and lying in the x-z plane with its upper surface at $y = 0$ as illustrated in Figure 2.2. The magnetisation in Figure 2.2 is periodic with a wavelength of λ. We assume that the dimensions of the sample are longer in the $\hat{x}$ and $\hat{z}$ directions than many times the period of magnetisation to eliminate the influence of edge effects. The cyclic magnetisation can be written in a Fourier series as

$$M = \frac{1}{2} \sum_{n=0}^{\infty} M_n e^{inkx} + c.c. \tag{2.9}$$

where $k = \frac{2\pi}{\lambda}$ and c.c. denotes the complex conjugate.

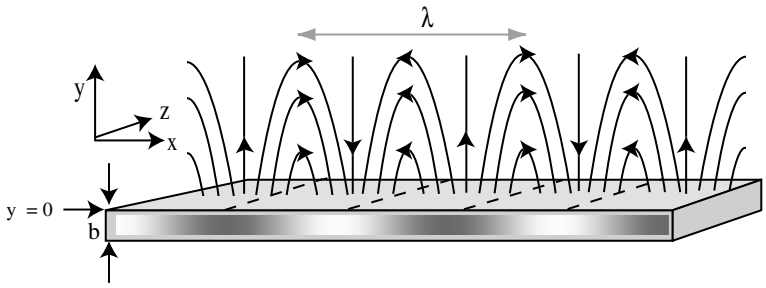

Figure 2.2: A film with a periodic magnetisation in the x-direction of wavelength λ. The varying magnetisation is depicted by varying grey-scale on the front edge. The cyclic pattern of magnetic field lines is shown above the surface.

The magnetic field above a magnetised surface can be described by a scalar potential $\phi(r)$, which is related to the magnetisation $\mathbf{M}(r')$ by equation (5.100) of Reference [56]

$$\phi(r) = -\frac{\mu_0}{4\pi}\int_V \frac{\boldsymbol{\nabla'}\cdot\mathbf{M}(r')}{|r-r'|}d^3r' + \frac{\mu_0}{4\pi}\oint_S \frac{\boldsymbol{n'}\cdot\mathbf{M}(r')}{|r-r'|}d^2r' \tag{2.10}$$

where n' is normal to the surface and V and S are the volume and surface of the material respectively. For in-plane magnetisation in the x-direction and with $\boldsymbol{n'}$ in the y-direction the scalar potential becomes

$$\phi(r) = \frac{\mu_0}{4\pi}\int_V \frac{\partial M/\partial x'}{|r-r'|}d^3r'. \tag{2.11}$$

Combining Equations 2.11 and 2.9 and assuming uniform magnetisation in the sample gives

$$\phi(r) = \frac{\mu_0}{8\pi}\sum_{n=0}^{\infty} inkM_n \int_V \frac{e^{inkx'}}{|r-r'|}d^3r' + c.c. \tag{2.12}$$

The volume integral in Equation 2.11 can be evaluated using standard methods by separating it into its Cartesian coordinates (see Appendix A of Ref. [39] and [57]). After some algebraic manipulation of the solution the x and y magnetic field components given by $B = -\nabla\phi$ are

$$\begin{pmatrix} Bx \\ By \end{pmatrix} = \sum_{n=0}^{\infty} B_n e^{-nky} \begin{pmatrix} -\cos(nkx+\delta_n) \\ \sin(nkx+\delta_n) \end{pmatrix} \tag{2.13}$$

where B_n is the magnetic field of the nth harmonic at the surface of the sample and δ_n is the phase of the magnetisation. Due to the exponential term in Equation 2.13, high order harmonics decay rapidly with increasing distance y from the surface. The magnetic field B_n of the nth harmonic at the surface in Equation 2.13 is given by

$$B_n = \frac{1}{2}(1-e^{-nkb})\mu_0|M_n| \tag{2.14}$$

where $|M_n|$ is the magnitude of magnetisation. For a periodic magnetisation with a single

$n = 1$ component of $\mathbf{M} = M_1 \cos(kx)\hat{\mathbf{x}}$, the phase δ_n in Equation 2.13 is zero and the only field contribution is due to the fundamental, $n = 1$. We can re-write Equation 2.13 as

$$\begin{pmatrix} Bx \\ By \end{pmatrix} = \frac{1}{2}\mu_0 M_1 (1 - e^{-kb}) e^{-ky} \begin{pmatrix} -\cos(kx) \\ \sin(kx) \end{pmatrix} \tag{2.15}$$

The term $(1 - e^{kb})$ can be understood by considering the magnetisation to be due to two current sheets $\mathbf{K} = \mathbf{M} \times \mathbf{n}'$ on the upper and lower surfaces. Applying Ampère's law shows that the upper sheet creates a field of $\frac{1}{2}\mu_0 M_1$ at the surface. This is partially cancelled by the exponentially decaying field due to the current sheet on the lower surface. Thus this field suppression term can be considered as a finite size effect when the wavelength λ is much larger than the thickness b.

The above results hold true for the magnetised tape used in the experiments in this thesis. Videotape recorded with a periodic magnetisation of wavelength $\sim 100\,\mu$m and a magnetic layer thickness b of $3.5\,\mu$m was used. In this case any higher order harmonic contributions than the fundamental recording frequency decay away within a few microns of the surface. The physical dimensions of the recorded tape were much larger than the recorded wavelength, allowing the edge effects to be neglected at the centre of the tape.

2.2.2 Producing Microscopic Magnetic Waveguides

The magnetic field due to a periodic magnetisation along $\hat{x}$ in the x-z plane was derived above and shown to decay exponentially with increasing distance from the surface. This is the same potential used to form magnetic mirrors for cold atoms [37, 41, 43, 44]. In order to form microscopic traps it is a simple extension to apply a uniform magnetic field in the x-y plane. The applied field periodically cancels the spatially varying field of the magnetised film, forming an array of field zeros above the surface of the film, spaced by λ. This is similar to the process of combining uniform magnetic fields with current-carrying structures to 'bias' the field and form local minima above the structure [15]. Therefore, we will call the uniform field B_{bias}.

The perpendicular distance from the surface y_0 at which the zero occurs is given by the y-component of field in Equation 2.15, meaning that B_{bias} given by

$$B_{bias} = B_1 e^{-ky_0} \tag{2.16}$$

produces a zero at y_0. Contours of constant magnetic field magnitude before and after application of B_{bias} are shown in Figure 2.3. The exponentially decaying field of a magnetised film with $B_1 = 110\,\text{G}$ and $\lambda = 100\,\mu$m is shown in Figure 2.3(a). In Figure 2.3(b) a bias field B_{bias} of 10 G is applied in the $-\hat{x}$ direction. The contours of constant field corrugate to form an array of field zeros. A Taylor expansion of the field to first order about the field minimum at

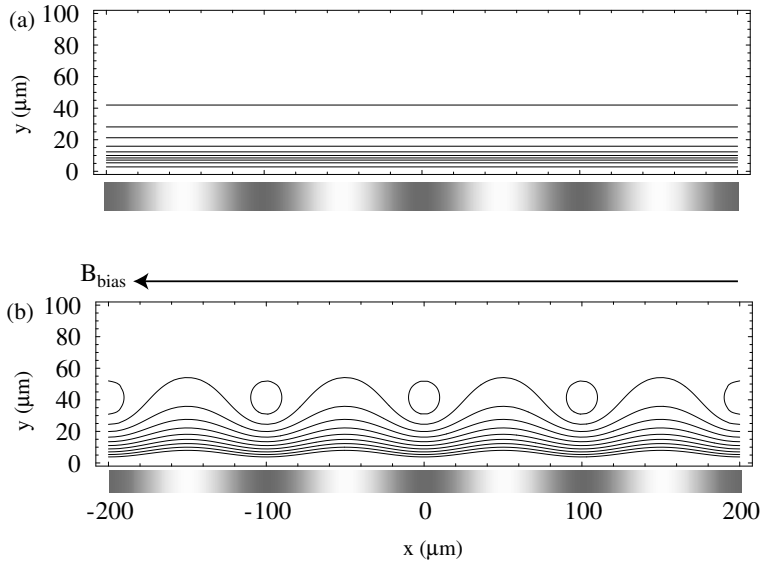

Figure 2.3: Contours of constant magnetic field above the magnetised surface. The periodic magnetisation of the sample is depicted in grey-scale. In (a) the field decays exponentially with distance y above the surface. In (b) a uniform magnetic bias field B_{bias} is applied, forming regions of field minima above the surface. Here $B_1 = 110\,\mathrm{G}$, $B_{bias} = 10\,\mathrm{G}$, and $\lambda = 100\,\mu\mathrm{m}$.

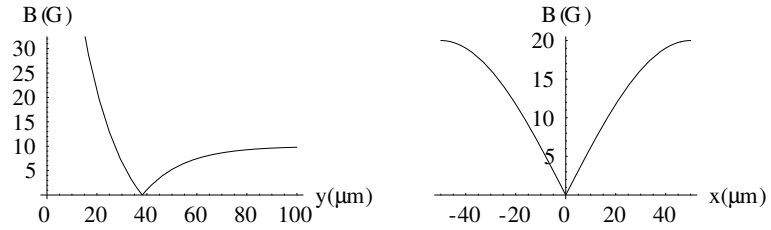

Figure 2.4: Cross sections of magnetic field magnitude in the x and y directions. $B_1 = 110\,\mathrm{G}$, $B_{bias} = 10\,\mathrm{G}$, and $\lambda = 100\,\mu\mathrm{m}$.

(x_0, y_0) gives

$$\begin{pmatrix} Bx \\ By \end{pmatrix} = -kB_{bias} \begin{pmatrix} y - y_0 \\ x - x_0 \end{pmatrix} \tag{2.17}$$

This is the form of a symmetric quadrupole field with a field gradient of kB_{bias}. At the centre of the minimum the field has cylindrical symmetry. The tubes of field minima can be considered as microscopic waveguides in which ultra-cold atoms can be confined in a line along z. These are similar to the macroscopic quadrupole guides formed by current carrying bars in magnetic traps with Ioffe-Pritchard geometry [58].

Cross sections of the field magnitude through the centre of the guides are shown in Figure 2.4, representing the potential seen by an atom. It can be seen from these cross-sections that the field is linear near the centre of the guide and goes to zero at the centre. The depth of

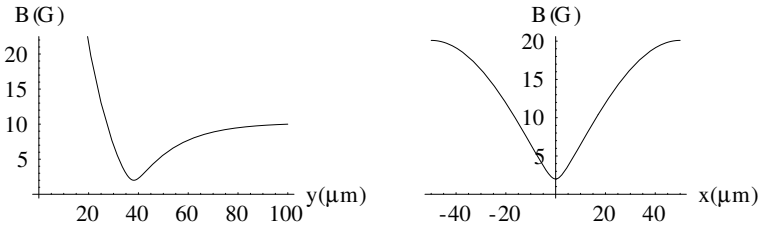

Figure 2.5: Cross sections of magnetic field magnitude in the x and y directions with an additional field of 2 G added along the z-direction. $B_1 = 110\,\mathrm{G}$, $B_{bias} = 10\,\mathrm{G}$, and $\lambda = 100\,\mu\mathrm{m}$.

the potential in the y-direction is equal to the applied field, B_{bias}. An additional field must be applied along the z-direction to prevent the total field from going to zero at the trap centre and reduce the probability of Majorana spin-flips. This has the additional effect of changing the curvature of the guide, creating trap potentials that can be described by a parabolic function close to the centre. The effect of adding field B_z along the axis of the cylinder is shown in Figure 2.5. In contrast to the cross-sections shown in Figure 2.4, the potential is rounded near the bottom and does not go to zero. The central part of the potential is harmonic for small-amplitude atomic oscillations with an oscillation frequency of

$$f = \frac{1}{2\pi} k B_{bias} \sqrt{\frac{\mu_\zeta}{m B_z}} \tag{2.18}$$

where m is the atomic mass and μ_ζ is the atomic magnetic moment.

2.2.3 Confinement in the Z-Direction

The tubes of magnetic field minimum offer a confining potential for cold atoms in two dimensions and are strictly-speaking atom guides. To form an atom *trap* in three dimensions, additional confinement must be provided. In the experiments described in this thesis the confinement in the z-direction is provided by current carrying wires behind the surface of the magnetised tape. Two parallel wires orientated along the x-direction and carrying current in the same direction form a field that rises to a maximum above each wire. The field minimum midway between the wires provides nominally harmonic confinement along z.

The z-field produced by two wires is shown in Figure 2.6. The combination of the field produced by these wires and the 2D waveguides forms an array of miniature atom traps close to the surface of the film. For wire separations and heights on the order of millimeters, the harmonic frequency in the z-direction (axial) is much less than the transverse (radial) waveguide frequency for an applied bias field B_{bias} of a few Gauss. This is a convenient way of forming Ioffe-Pritchard microtraps with high aspect ratios in which the radial trapping frequency is much greater than that in the axial direction.

It has been shown that an array of two dimensional quadrupole guides for cold atoms can be formed with a periodically magnetised film and external magnetic fields and that these can be

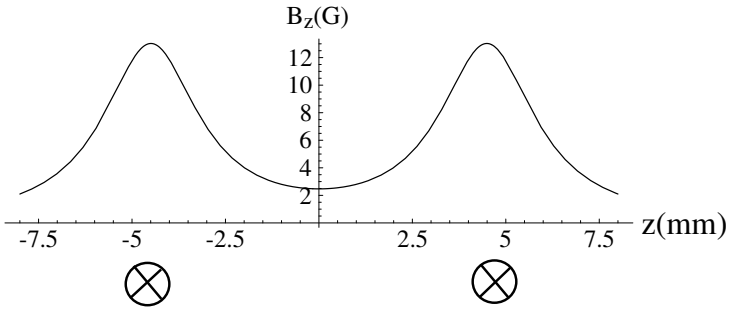

Figure 2.6: The z-component of magnetic field above two wires at a height $y = 1.5\,\text{mm}$ carrying current into the page. This method is used to provide confinement in z. In this example the separation is 9 mm and the current is 10 A.

extended to form long thin atom traps. Subsequent chapters describe the experimental reality of working with such traps but first, one other essential aspect is introduced - the phenomenon of Bose-Einstein condensation.

2.3 Bose-Einstein Condensation

In this section Bose-Einstein condensation will be briefly introduced by outlining how condensation occurs and the influence of inter-particle interactions on the quantum description of the system.

2.3.1 Phase Space Density

The thermal de Broglie wavelength of a particle with mass m at temperature T is defined as

$$\lambda_{\text{dB}} = \frac{h}{\sqrt{2\pi m k_B T}} \tag{2.19}$$

The phase space density of an ensemble of particles with a peak number density n_0 is

$$\text{PSD} = n_0 \lambda_{\text{dB}}^3 = n_0 \left(\frac{h}{\sqrt{2\pi m k_B T}} \right)^3 \tag{2.20}$$

An intuitive picture of Bose-Einstein condensation can be formulated by considering that at high density and low temperature the de Broglie matter waves begin to overlap and interfere constructively. However, a more full description is obtained by considering the statistical properties of a collection of bosons.

2.3.2 Degeneracy in a Non-Interacting Bose Gas

The quantum statistics of an ideal gas of Bosons are described by the Bose-Einstein distribution. The distribution can be obtained from first principles in the framework of the grand canonical

ensemble [59, 60]. The average occupation number of a quantum state $\langle n_i \rangle$, given by the Bose-Einstein distribution function is

$$\langle n_i \rangle = \frac{1}{e^{\beta(\epsilon_i - \mu)} - 1} \tag{2.21}$$

where ϵ_i is the energy of the i^{th} state, μ is the chemical potential and $\beta = \frac{1}{k_B T}$. Bose-Einstein condensation is characterised by a macroscopic occupation of the single-particle ground state ϵ_0 which occurs in the limit $\mu \to \epsilon_0$. The occupancy of the ground state N_0 and the excited states N_{ex} is obtained here following a method similar to [61] and [62]. By integrating Equation 2.21 for total number and explicitly retaining the ground state, the number of atoms is given by

$$N = N_0 + N_{ex} = N_0 + \int_0^\infty \rho(\epsilon) \frac{1}{e^{\beta(\epsilon - \mu)} - 1} d\epsilon \tag{2.22}$$

where the integral over exited states is weighted by the density of states in phase space $\rho(\epsilon)$. The density of states of a gas confined in an external potential $V(\mathbf{r})$ differs from that of a gas in a box [59]. Bagnato *et. al.* [63] calculated the influence of ground state occupancy in various power law potentials of which the three-dimensional harmonic oscillator potential is a special case. We consider the harmonic oscillator potential because of its relevance to a Bose gas in a Ioffe-Pritchard geometry trap. For the potential

$$V(\mathbf{r}) = \frac{1}{2} m(\omega_x^2 x^2 + \omega_y^2 y^2 + \omega_z^2 z^2) \tag{2.23}$$

the energy levels are given by

$$\epsilon(n_k) = \sum_{k=1}^{3} (n_k + \frac{1}{2}) \hbar \omega_k \tag{2.24}$$

where $n_k \geq 0$. It can be shown [62] that the density of states for Equation 2.24 is given by

$$\rho(\epsilon) = \frac{\epsilon^2}{2(\hbar \bar{\omega})^3} \tag{2.25}$$

where $\bar{\omega}$ is defines the geometric mean of harmonic frequencies as $\bar{\omega} = (\omega_1 \omega_2 \omega_3)^{1/3}$. In the calculation to obtain Equation 2.25 the zero-point energy is not included. The treatment is therefore only valid for energies large compared to the harmonic level spacing, $\epsilon > \hbar\omega$. Substitution of the density of states into Equation 2.22 allows calculation of the critical temperature T_c at which macroscopic ground state occupation commences. This is defined as the point at which all atoms only just remain in the excited states and the Bose-Einstein function goes to a maximum at $\mu = 0$. The integral for excited state occupation then takes the form

$$N_{ex} = \frac{(k_B T_c)^3}{2(\hbar \bar{\omega})^3} \int_0^\infty \frac{x^2}{e^x - 1} dx \tag{2.26}$$

where we have made the substitution $x = \frac{\epsilon}{k_B T_c}$. The integral in x is given by $\Gamma(3)\zeta(3)$ where $\Gamma(\alpha)$ and $\zeta(\alpha)$ are the gamma and Riemannn zeta functions. A rearrangement of Equation

2.26 gives an expression for the critical temperature

$$k_B T_c \approx 0.94 \hbar \bar{\omega} N^{1/3} \tag{2.27}$$

where $\Gamma(3) = 2$ and $\zeta(3) = 1.202$. By considering that $N = N_0 + N_{ex}$, an expression giving the condensed fraction for $T < T_c$ is also obtained

$$\left(\frac{N_0}{N}\right) = 1 - \left(\frac{T}{T_c}\right)^3 \tag{2.28}$$

which differs from the expression for a gas in box only by the magnitude of the exponent. The phase space density (PSD) at which condensation occurs is given by

$$\text{PSD} = \zeta(3) = 1.202 \tag{2.29}$$

which is in agreement with the intuitive picture that that condensation occurs when the thermal de Broglie wavelength becomes of the order of the inter-particle spacing.

It is worthwhile noting a significant restriction of the above approach that is of relevance when considering highly anisotropic trapping potentials (i.e. $\omega_{1,2} \gg \omega_3$). The condition that the ground state energy is greater than the harmonic level-spacing $\hbar\omega$ was required to derive the above results, a condition not fulfilled for large $\omega_{1,2}$. The case of an ideal gas in a highly anisotropic potential is considered in Reference [64] in which the authors point out that condensation formation is a much more complex process. Condensation in highly anisotropic potentials is of significant theoretical and experimental interest. However, for the conditions employed in this thesis, a 3D approach will be adequate to describe the system.

2.3.3 The Weakly Interacting Condensate

In most realistic scenarios the ground state wavefunction of a harmonically confined Bose gas deviates from that of the quantum harmonic oscillator ground state due to inter-particle interactions.

Inter-particle interactions for a spin-polarised alkali gas in a hyperfine ground state can be described by a scattering pseudo-potential characterised by the scattering length a. For ^{87}Rb the scattering length is positive and gives rise to repulsive interactions. The Gross-Pitaevskii (GP) equation [43] describes the spatio-temporal evolution of the condensate wavefunction $\psi(r,t)$ in an external potential $V(r,t)$

$$i\hbar \frac{\partial}{\partial t}\psi(r,t) = \left(-\frac{\hbar^2}{2m}\nabla^2 + V(r,t) + g|\psi(r,t)|^2\right)\psi(r,t) \tag{2.30}$$

where the interaction due to the scattering term is described by the coupling constant

$$g = \frac{4\pi\hbar^2 a}{m} \tag{2.31}$$

and the wavefunction can be expressed as

$$\psi(r,t) = \psi(r)e^{-\frac{i\mu}{\hbar}t} \tag{2.32}$$

satisfying the particle number normalisation condition, $N = \int \psi(r)^2 dr$ such that $|\psi(r)^2|$ is the number density.

A solution of Equation 2.30 for $\psi(r,0)$ in the zero-temperature limit can be obtained using the Thomas-Fermi approximation [65]. For a sufficiently large atom number, the kinetic energy term can be neglected compared to the inter-particle interaction potential. Thus the physical size of the ground state in the external potential $V(r,0)$ is determined by the balance between repulsive internal interactions and the external confinement. The square of the solution [55] of the Gross-Pitaevskii equation

$$|\psi(r)|^2 = n(r) = \text{Max}\left[\frac{\mu - V(r)}{g}, 0\right] \tag{2.33}$$

describes the ground state density in the Thomas-Fermi approximation and has discontinuous boundaries at $V(r) = \mu$. For the harmonic oscillator potential of Equation 2.23 the condensate wavefunction extends to a radius

$$R_i = \sqrt{\frac{2\mu}{m\omega_i^2}}. \tag{2.34}$$

in each direction, referred to as the Thomas-Fermi radius. The ground state density then becomes

$$|\psi|^2 = \frac{\mu}{g}\left(1 - \sum_{i=1}^{3}\left(\frac{r_i}{R_i}\right)^2\right) \tag{2.35}$$

for spatial coordinate r_i. An expression for the chemical potential can be obtained using Equation 2.35 and the atom number normalisation condition so that,

$$N = \int |\psi|^2 d^3r = \frac{\mu}{g}\frac{8\pi}{15}\left(\frac{2\mu}{m\bar{\omega}^2}\right)^{3/2} \tag{2.36}$$

where $\bar{\omega}$ is once again the geometric mean of trap frequencies, giving the chemical potential as

$$\mu = \left(\frac{15\hbar^2 m^{1/2} N\bar{\omega}^3 a}{2^{5/2}}\right)^{2/5} \tag{2.37}$$

With knowledge of the trap parameters, scattering length and the condensate number, relevant properties such as physical size and chemical potential can be calculated in the Thomas-Fermi approximation.

2.4 Condensate Expansion

In order to model the dynamical behaviour of a condensate in a confining potential or in free expansion a solution of the time dependent Gross-Pitaevskii equation must be sought. This can be achieved numerically, however, the situation may be considered analytically in the Thomas-Fermi regime using the scaling approach developed by Castin and Dum [66] and Kagan, Surkov and Shlyapnikov [67]. Their method is developed by first considering the evolution of a classical gas at zero temperature in a time-dependent harmonic potential with an initial Thomas-Fermi density distribution that is the steady state of the quantum system. The time-dependent scaling parameters in each dimension, $\lambda_i(t)$ in the i_{th} dimension, are then obtained by considering the total force experienced by a particle in the gas and using this in the Newtonian equation of motion. They then go on to demonstrate that the scaling factor solution obtained is also a solution of the GP equation. The method is particulary helpful because the subsequent evolution of a condensate with initial size $R_i(0)$ in a time-dependent potential is described completely by a set of coupled differential equations of which the scaling factors $\lambda_i(t)$ are solutions. This is significantly simpler than obtaining a full numerical solution to the time-dependent GP equation.

The dimensions of a condensate propagating in the time-dependent harmonic potential

$$U(\mathbf{r},t) = \frac{1}{2}\sum_{i=1,2,3} m\omega_i^2(t)r_i^2 \tag{2.38}$$

are modified by the scaling parameters $\lambda_i(t)$ which are given by the solution of

$$\ddot{\lambda}_i = \frac{\omega_i^2(0)}{\lambda_i(t)\lambda_1(t)\lambda_2(t)\lambda_3(t)} - \lambda_i(t)^2\omega_i^2(t) \quad (i=1,2,3) \tag{2.39}$$

with the initial condition $\lambda_i(0) = 1$. The initial confining potential and thus condensate is usually cigar shaped with radial symmetry and $\omega_r(0) > \omega_z(0)$ and aspect ratio $\epsilon = \omega_z(0)/\omega_r(0)$. In the case of free expansion, all of the trap frequencies go to zero at time $t = 0$. It is convenient to scale the time by the radial frequency to work with a dimensionless time $\tau = \omega_r t$. The equations in 2.4 reduce to

$$\frac{d^2\lambda_r(\tau)}{d\tau^2} = \frac{1}{\lambda_r(\tau)^3\lambda_z(\tau)} \qquad \frac{d^2\lambda_z(\tau)}{d\tau^2} = \frac{\epsilon^2}{\lambda_r(\tau)^2\lambda_z(\tau)^2} \tag{2.40}$$

which have the solutions [66, 68]

$$\lambda_r(\tau) = \sqrt{1+\tau^2} \qquad \lambda_z(\tau) = 1 + \epsilon^2\left(\tau\arctan\tau - \ln\sqrt{1+\tau^2}\right) \tag{2.41}$$

The expansion is greatest in the radial direction corresponding to the release of the condensate mean field energy from the tight trapping dimension, with comparatively little expansion in the z-direction.

2.5 Summary

The first part of this chapter introduced the interaction between an atomic magnetic moment and an external magnetic field. The principle of magnetic trapping in microscopic waveguides formed by a periodically magnetised film was described. It was shown that at low temperature a collection of Bosons will undergo the phase transition to Bose-Einstein condensation. Having introduced these essential ideas, the following chapters now give an account of the experimental system, providing further necessary background theory as and when required. This begins with a description of the experimental apparatus in the next chapter.

Chapter 3

Experimental Apparatus

In this chapter the laser system and optics required to produce the appropriate beams for cooling, trapping and imaging ensembles of ultracold ^{87}Rb atoms are outlined. The ultra-high vacuum system is then introduced, the computer control system used to coordinate the experiment is described followed by a description of the atom chip, magnetic field control and absorption imaging arrangement.

The laser system, optics and vacuum system described in these sections are all mounted on a $1.5 \times 3\,\mathrm{m}$ tapped Melles-Griot optical table floating on compressed air.

3.1 Lasers and Optics

The following sections contain a description of the laser system used in the experiments, followed by an outline of the optical components used to manipulate the light. Details are given of the four lasers that provide light necessary for operating the *two* magneto-optical traps that are themselves described in Chapter 4. For the purposes of this chapter they will simply be referred to as the 'LVIS-MOT' and the 'mirror-MOT'. The methods used to tune and stabilise the frequencies of each of the lasers are given, followed by a description of how the beams are subsequently manipulated by fibre-optics, acousto-optic crystals, mirrors, beam-splitters and waveplates.

3.1.1 Diode Lasers

Trap light for alkali atom traps is typically provided by titanium-sapphire lasers or solid-state diode lasers. Ti:Sapph lasers are capable of generating high power (0.5-1 W) in the near infra-red with reasonably coarse wavelength tunability. However, they are expensive and can require a considerable investment of time to align and maintain. Coarse tunability was not required in the work described here and diode lasers were used exclusively as the source of light. Low power (50 mW) laser diodes are readily available at a number of suitable wavelengths for cooling alkali metals. A notable exception is the case of sodium where it is still necessary to use dye lasers.

Recent advances in diode technology allow the production of output powers up to 1 W at costs commercially competitive with Ti:Sapph lasers.

One of the principal requirements of a laser cooling system is a stable output with a narrow linewidth. A free running laser diode has a linewidth of several hundreds of MHz rendering it unsuitable for selectively exciting atomic transitions with natural linewidths of a few MHz. However, it is possible to reduce the linewidth well below that of a bare diode using an external cavity configuration [69, 70], the so-called external cavity diode laser (ECDL). The diode cavity is extended to tens of millimeters by placing a grating after the diode and reflecting the first order diffracted beam back into the laser diode. Small adjustments to the grating position allows the frequency to be tuned. The frequency can be stabilised by providing active feedback to the grating position and in combination with feedback to the laser current and temperature, linewidths below 1MHz can be achieved.

In the experiments described here, four diode lasers are employed to provide light at several different frequencies. A 'reference ECDL' provides a stable oscillator signal as well as light for optical pumping. A 'master' repump ECDL and an injection locked 'slave' repump diode laser provide repump light for the MOTs. To achieve the high intensities needed for trapping the large numbers of atoms necessary for BEC a high power commercial "tapered amplifier " system (Section 3.1.4) is used as the main trapping laser for the MOTs. They are described in further detail in the following sections. First, the methods of generating zero-crossing signals for the laser locks by Doppler-free spectroscopy will be introduced.

3.1.2 Doppler-Free Spectroscopy

Sub-doppler hyperfine features can be obtained from vapour cells at room temperature using techniques including saturated absorption spectroscopy [71] and polarisation spectroscopy [72]. Polarisation spectroscopy is advantageous because of its higher signal to noise and dispersive line shapes which provide convenient features for locking the laser frequency. Polarisation spectroscopy works by detecting small rotations in the linear polarisation of a weak probe beam caused by birefringence in an atomic vapour induced by a circularly polarised pump beam. The set-up for a polarisation spectrometer is shown in Figure 3.1. The incoming laser light is split into a strong pump and weak probe beam. The pump beam is circularly polarised by a quarter-wave plate and the probe beam is linearly polarised. The pump and probe beams are overlapped in the vapour cell. A polarising beam-splitter cube (PBC) is used to analyse the probe beam after transmission through the cell by measuring the relative transmission in each arm. Initially, when off resonance, the probe polarisation is set such that equal intensities are transmitted into each photodiode. As the laser is scanned through an atomic resonance, as well as the usual saturation effects, the birefringence of the medium rotates the polarisation of the probe beam by a small angle. This results in different intensities being transmitted to each photodiode. The difference of the two signals is taken using a differential amplifier. The resulting signal has a dispersive shape [73] which is used as the error signal for locking the laser.

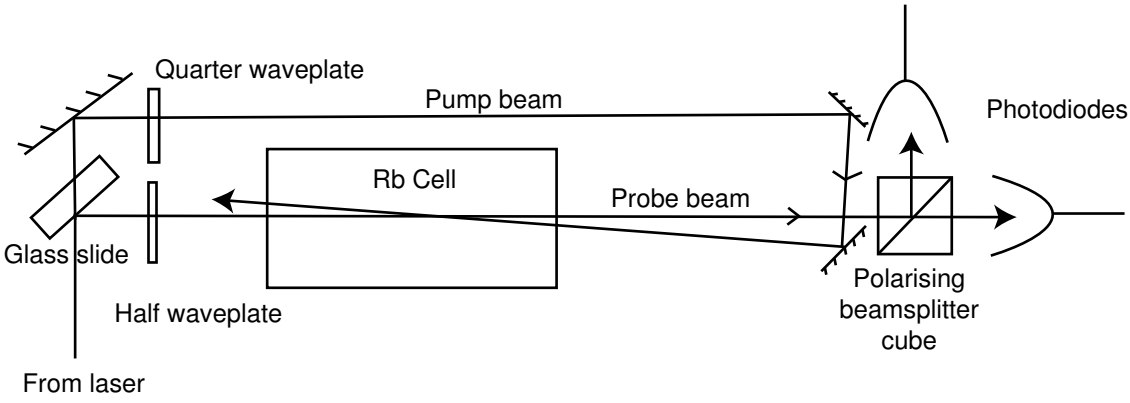

Figure 3.1: Polarisation spectroscopy set-up.

3.1.3 The Reference Laser

The reference laser is an ECDL similar to the design described in Reference [74]. It is locked to the $F = 2 \rightarrow F' = 3$ ^{87}Rb cycling transition using a dispersive zero-crossing signal generated by a polarisation spectrometer such as that shown in Figure 3.2. (The ^{87}Rb level scheme is shown in Appendix A.) A piezo-electric transducer mounted on the ECDL grating allows fine adjustment of the position. A 10 Hz triangular ramp (BK Precision 3010 Function Generator) is sent to the piezo to scan it periodically so that the saturation and polarisation absorbtion spectra can be observed. When locked, the feedback is split into a slow integral component and a differential component with faster response. The slow integral component is suited to correcting dc drifts by feeding back to the ECDL grating via the piezo driver. The 'fast' feedback is applied to the laser diode injection current. It is possible to lock the reference laser all day under quiet conditions. A beat signal is obtained by overlapping a small fraction of the reference beam with a test beam from the TA100 master oscillator and is used in the offset locking scheme (Section 3.1.5) to provide an error signal for the TA100 trap laser. The reference laser is also used to provide light for optical pumping after a double pass through an acousto-optic modulator (AOM). The profile of the output beam is elliptical with its major axis in the horizontal plane and an aspect ratio of approximately 2:1. An anamorphic prism pair is used to convert the beam aspect ratio from elliptical to circular.

3.1.4 High Power Tapered Amplifier Laser

A *Toptica TA100* laser produces high output power trapping light for the MOTs by combining a stabilised "master oscillator" external cavity diode laser and a tapered amplifier chip for achieving high powers. The operational components are shown in Figure 3.3. The master oscillator module contains the laser diode, collimating lens, the feedback grating and beam steering

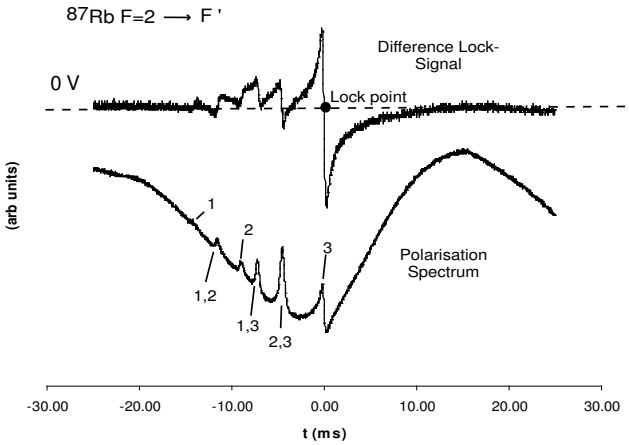

Figure 3.2: Polarisation spectrum of the ^{87}Rb $F = 2 \rightarrow F'$ transition. The lower trace is the signal recorded by one of the photodiodes. The upper-trace is the difference signal between the two photodiodes. This provides the dispersive zero-crossing for the lock. The features are labelled by their F' value.

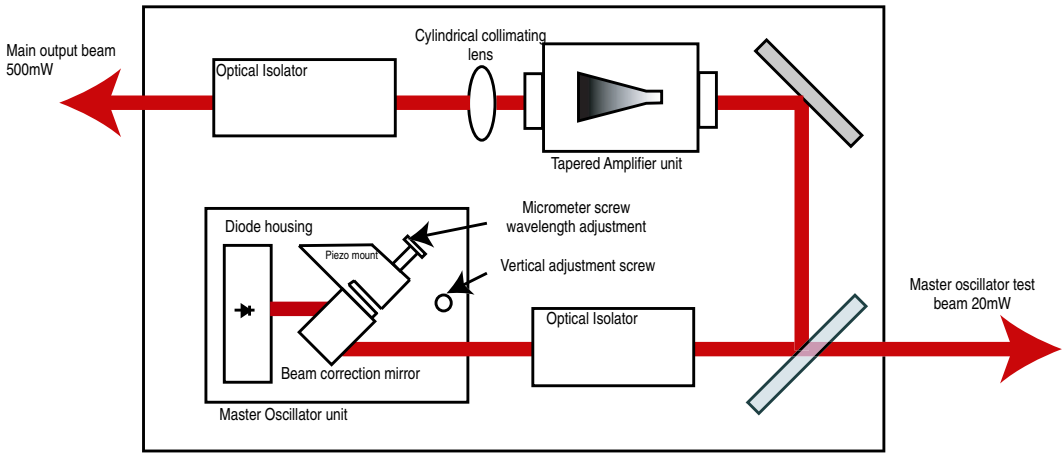

Figure 3.3: The components of the tapered amplifier diode laser.

correction mirror. The brass diode housing is cooled by a thermoelectric peltier element. Typically the master oscillator is operated with an injection current of 80-100 mA at a temperature set point of $21 - 24°$C.

The mode-hop-free tuning range of the master oscillator piezo scan is ~ 6 GHz. The control module incorporates a feed forward which adds a small offset to the current in proportion to the piezo scan to increase the mode-hop-free tuning range.

After passing through a 60 dB optical isolator the master oscillator is steered into the tapered amplifier unit by two mirrors. The first is a partially reflecting mirror which decouples part of the beam and sends it out of the back of the laser housing. This beam provides a low power output which is used to monitor the frequency and to generate the feedback signal to lock the master oscillator. A second steering mirror couples the seed beam into the back facet of the tapered amplifier chip.

The tapered amplifier chip operates at a current of 2A and a peltier element stabilises the temperature at 19.9 °C. The front and rear facets of the amplifier chip are anti-reflection coated to prevent lasing without seeding. The mode of the amplifier is completely determined by the master oscillator beam.

The rapidly diverging output beam from the amplifier is collimated by a cylindrical lens immediately after the amplifier output and a subsequent optical isolator protects the amplifier chip from optical feedback. The output of the TA100 is a vertically polarised, collimated beam with a nominal power of 500 mW.

The absolute output power is very sensitive to the alignment of the seed beam into the tapered amplifier chip. To maintain optimal output power the alignment was regularly adjusted with the mirror micrometer screws while monitoring the amplifier output with a power meter.

3.1.5 The Frequency Offset Lock

The TA100 laser is locked to the reference laser using a frequency offset lock method similar to that described in References [75] and [71]. The method stabilises one laser frequency relative to another by comparing the beat signal between the two with a local oscillator frequency. Changing the value of the local oscillator frequency changes the offset frequency between the two lasers, thereby allowing relative detuning of one laser from the other. The reference laser provides a stable reference frequency, in our case resonant with the $F = 2 \rightarrow F' = 3$ transition in ^{87}Rb.

Figure 3.4 shows the offset locking scheme. Part of the TA100 test beam is overlapped with a beam picked off from the reference laser on a fast rf photodiode as shown in Figure 3.4 (a). The beat signal (f_{beat}) from the photodiode is mixed with a local oscillator signal (f_{LO}) generated by a voltage controlled oscillator (VCO), as shown in Figure 3.4(b). The output of the mixer has two components, $f_{LO} + f_{beat}$ and $f_{LO} - f_{beat}$. This signal is passed through a 90 MHz low pass filter to remove the $f_{LO} + f_{beat}$ component and the remaining signal $\Delta f = f_{LO} - f_{beat}$ is split into two parts by an rf power splitter chip. One part of the signal

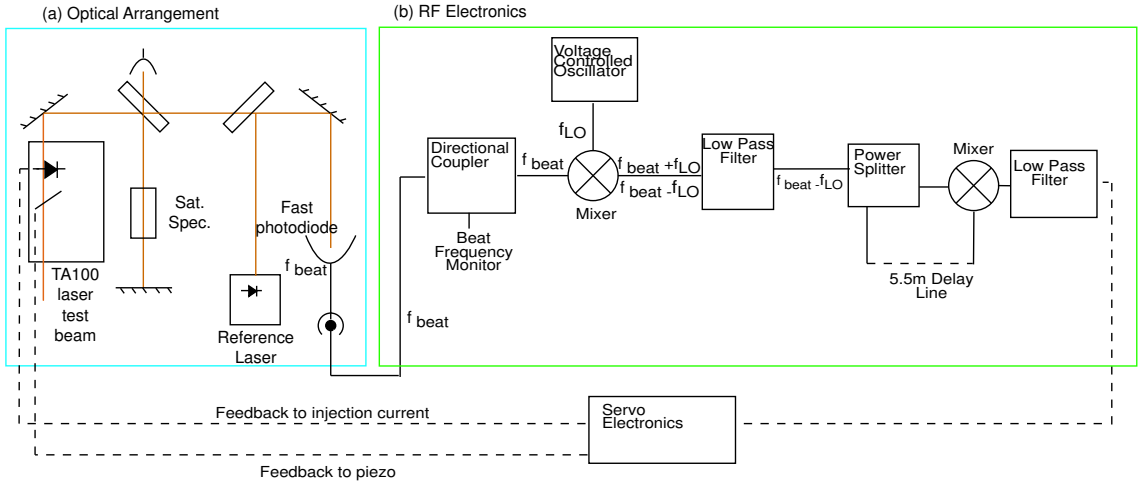

Figure 3.4: Offset Lock Schematic. Optical components are shown in part (a). RF electronic components are shown in part (b).

is sent through a 5.5 m long coaxial cable delay line which introduces a phase shift. The two signals are recombined by a mixer. The component at twice the frequency is blocked by a low pass filter. The remaining output has a cosine shape with a period determined by the delay in the coaxial cable. The delay in 1 m of cable is ~ 5 ns [75] and so 5.5 m of cable produces a cosine with zero crossing separated by 36 MHz. The zero crossings are used as the error signal for the TA100 servo loop with a capture range of ~ 18 MHz. The fringes have a broad envelope determined by the bandwidth of the 90 MHz low pass filter.

The absolute frequency of the TA100 laser compared to the reference laser is determined by the number of complete 36 MHz fringes traversed between resonance and the lock point plus the frequency difference $|f_{LO} - f_{beat}|$. AOMs in the trap beams permanently red-detune the laser output by -92 MHz so the lock point is chosen to shift the frequency to the blue as compensation. The usual lock point corresponded to $|f_{LO} - f_{beat}| = 25.5$ MHz.

Once locked, the laser can be detuned to the desired frequency by altering the local oscillator frequency, resulting in a corresponding change in f_{beat}. The local oscillator frequency required to produce a detuning of δ from the atomic resonance is $f_{LO}\,(\mathrm{MHz}) = \delta + 92\,\mathrm{MHz} + 25.5\,\mathrm{MHz}$. e.g. for a detuning of $\gamma = -12$ MHz, the VCO frequency is set to 105.5 MHz.

The error signal generated by the offset lock is applied to the injection current of the TA100 master oscillator diode and the piezo on the master oscillator grating. The TA100 current feedback allows modulation in the range of dc to 16 kHz with 1 V input corresponding to 10 mA [76]. A direct BNC input is provided on the current control module (DC110) to allow external modulation. No such input was provided on the module which controlled the piezo stack voltage (SC110). Some modification of the system was required to allow custom modulation of the piezo. A computer analog interface module with a single BNC connector and a 25-pin sub-D connector was used as the input and the series of jumpers on board were set

according to the manufacturers instructions to connect the analog interface to the laser SC110 scan module via the backplane of the control rack. Once set, the BNC connector on the analog interface module was configured as an input for piezo modulation. The voltage applied to this input was added to the voltage generated by the scan module. Therefore, for full user-control, the offset and amplitude of the scan module must be set to zero. An input voltage of 100 mV to the input scans the laser by ~ 1 GHz - the approximate width of the Doppler broadened $F = 2 \rightarrow F'$ transition.

3.1.6 Repump Lasers

The trapping light is tuned to the $F = 2 \rightarrow F' = 3$ hyperfine transition. Off-resonant excitation to hyperfine levels other than $F' = 3$ excited state can result in a decay into the $F = 1$ ground state which does not respond to the trapping light, effectively halting the cooling and trapping process. To reengage these atoms in the cooling cycle they must be returned to the $F = 2$ state with repump light. Compared with trapping light, relatively little repump power is required for efficient operation of a MOT (a few mW or less). However, to ensure that repump power was not a limiting factor in the optimising the combined LVIS and mirror-MOT system and to compensate for the reduction in power due to fibre coupling, two repump lasers are used to increase the available power. The lasers are used in the master/slave arrangement. The master repump laser is an ECDL locked to a polarisation spectrometer. The output from the slave laser of 21 mW is sufficient to operate both the LVIS and mirror-MOTs even after subsequent losses due to an AOM and optical fibre. The master/slave arrangement is shown in Figure 3.5. The slave repump laser does not require a grating to provide optical feedback. The seed laser beam from the master laser is sufficient to determine the mode of the slave laser. Small adjustments to the slave injection current and seed beam input alignment help to increase the mode-hop-free tuning range.

It can be useful to be able to control the repump intensity in a MOT independently of the trapping light. An AOM was installed in the repump beam to allow intensity control by varying the rf power applied to the AOM. A benefit of using an AOM is that the master laser can be locked to a spectral feature with a steep slope and the slave laser output can be shifted back on resonance with the $F = 1 \rightarrow F' = 2$ repump transition using the AOM. Lenses are used to focus the repump beam into the AOM (Gouch and Housego M080-1F-GH2) and to re-collimate it afterwards. All but the first diffracted order are blocked with beam blocks and the remaining beam is steered into the repump fibre coupler with a pair of mirrors.

Part of the output beam from the slave laser is picked off by an optical flat and sent to a saturated absorption spectrometer. This provides a spectrum with which to compare the polarisation spectrum of the master laser. The spectra of the master and slave lasers can be seen in Figure 3.6. The repump laser arrangement could be greatly simplified in future by using a single diode laser operating at higher power and locked to a polarisation spectrometer.

Various optical elements manipulate the profile, intensity and polarisation of the beams in

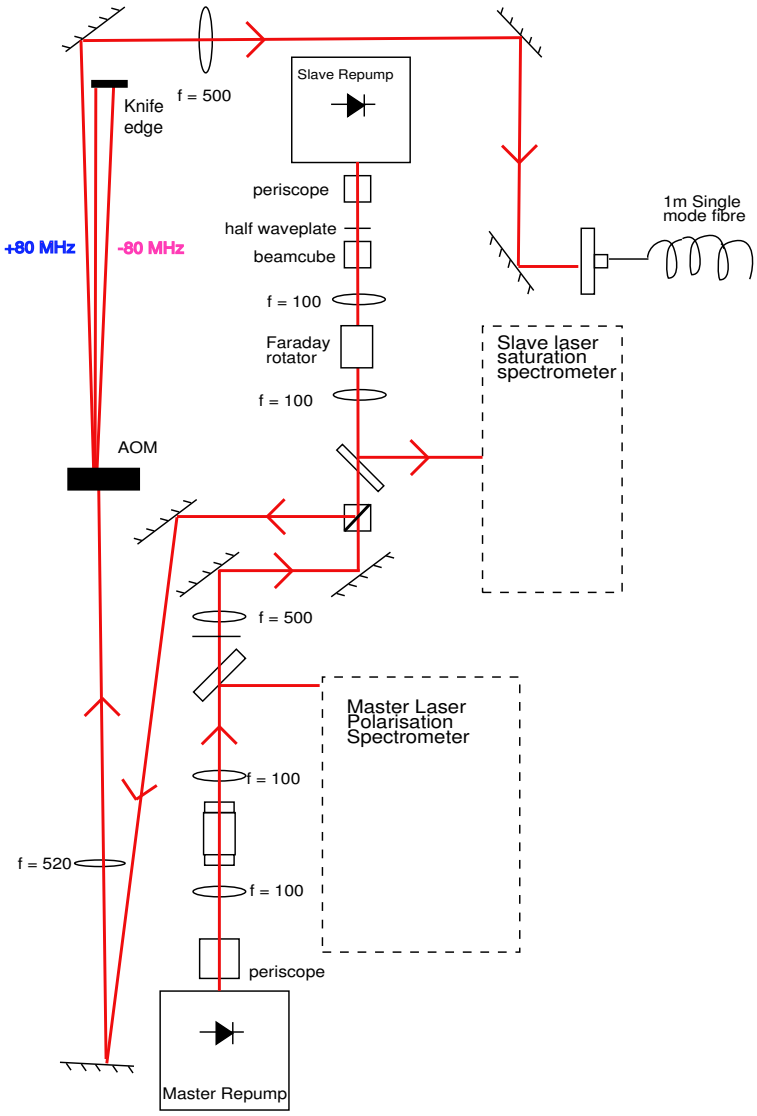

Figure 3.5: Repump Master/Slave Optics. Focal lengths are given in mm.

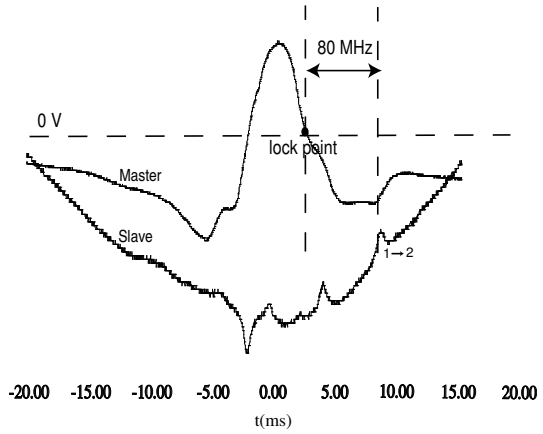

Figure 3.6: Polarisation spectrum of the ^{87}Rb $F = 1 \rightarrow F'$ transition (upper trace) and saturated absorption spectrum (lower trace).

order form the MOTs and they are described next.

3.1.7 AOMs and Fibre Coupling

Separate control of the intensity and frequency of the trap light in the LVIS-MOT and mirror-MOT is necessary. Therefore, the 500 mW output of the TA100 amplifier is split into a 400 mW LVIS beam and a 100 mW mirror-MOT beam so that each can be manipulated independently.

Both trap beams are focused into their respective AOMs to act as fast attenuators that allow the light to be extinguished in a few microseconds. In order to maximise the transmitted laser power, large focal length lenses ($f = 400$ mm) were used to focus the light to a waist in the AOM crystal (NEC C2817A) and re-collimate it afterwards. The bare crystal transmits over 80 percent of the input power without any applied rf signal. A total of 70 percent of the input power can be directed into the first diffracted order by adjusting the angle between the crystal and the laser beam. The remaining diffracted orders are blocked. The intensity of the transmitted light can be varied by changing the rf power applied to the AOM crystal. An rf attenuator with four preset VCO levels is used to vary the rf power during an experimental sequence. The rf is then amplified (Motorola CA2832) before being applied to the AOM crystal.

Optical fibres are used to spatially filter the mode profile of each trapping beam and minimise drifts of the beam alignment in the MOTs. Single mode fibres for 780 nm (OFR FCS-780-FC/APC2) are used for the LVIS and mirror-MOT beams. The fibre for the LVIS beam is polarisation maintaining (ECPP-780-1-FC/APC2) to avoid undesirable drifts in the intensity of the probe beam which is picked off after the fibre. A half-wave plate before the fibre port ensures that the angle of linear polarisation is rotated to propagate along the principal axis of the fibre. Commercial fibre ports (OFR HCP PAF-X-11-780) (effective focal length 11 mm) containing a single lens are used to couple the collimated beams into the fibre core. The construction of the ports allows fine adjustment of the lens in the vertical plane as well as

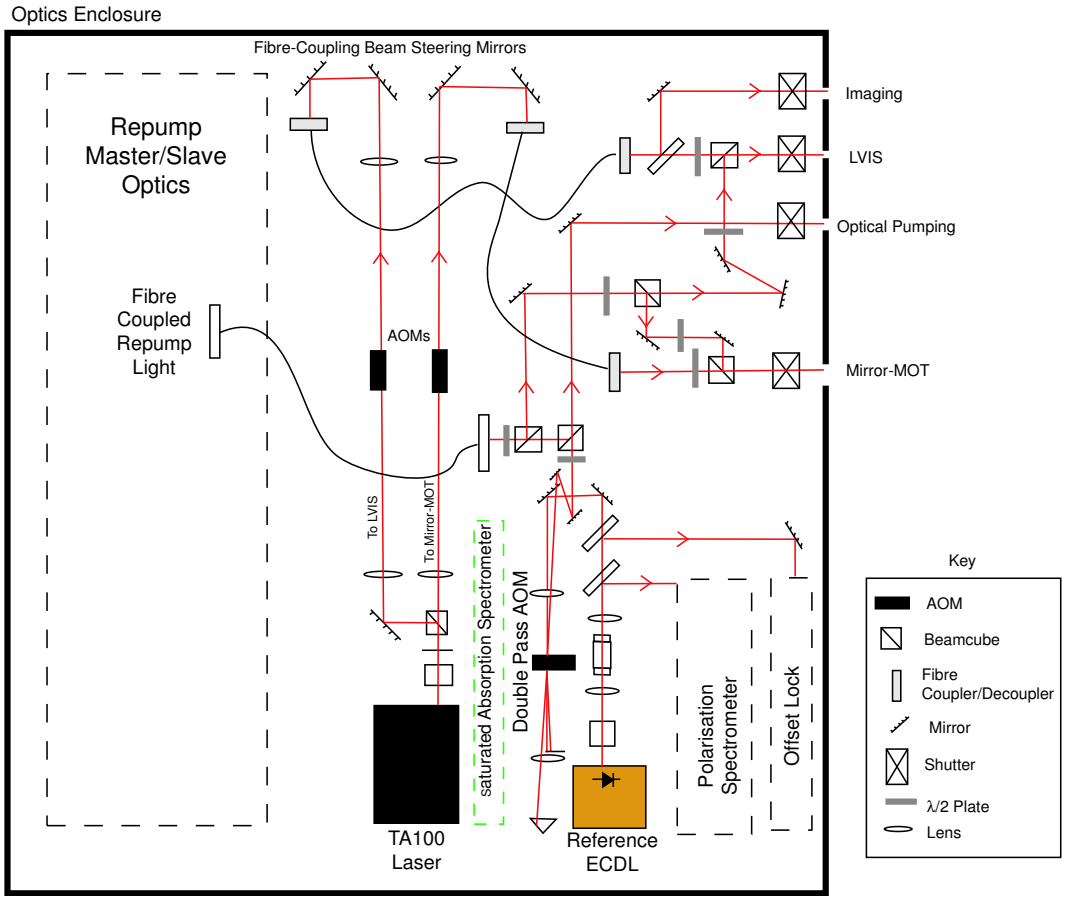

Figure 3.7: Overview of the fibre coupling system and repump combination optics. The optical pumping AOM double pass is also shown.

tilt and yaw using spring loaded grub screws on the back plate. The fraction of light coupled through the fibres is usually about 50% with up to 60% possible if particular attention was paid to the alignment of the tilt plate and collimation of the input beam. In daily operation, fine adjustment of the grub screws was not necessary and good alignment could be achieved using the pair of steering mirrors before each coupler. The optical arrangement showing the fibre-coupling of the LVIS and mirror-MOT beams and their combination with repump light is shown in Figure 3.7.

A pair of steering mirrors couples the repump light from the slave repump laser into a fibre (OFR FCS-780-FC/APC2) that does not maintain polarisation. Although MOTs are generally insensitive to the profile of repump light, fibre coupling was chosen to minimise drifts in the position of the beam.

The reduction in laser power available to operate the MOTs as a result of fibre coupling the trap and repump light was deemed acceptable in view of the resulting stability of the position of each MOT. Well defined MOT position and stability are essential for efficient transfer from the MOT to a magnetic trap. In normal operation, regular alignment of the steering mirrors

is necessary on a daily basis to maximise the transmitted power. This process of adjusting coupling into the fibre is preferable to drifts in beam position within the MOTs due to beam pointing instability.

After propagation through the 1 m fibres, single snap-on collimators (OFR CFC-5-780) transform the light into 1 mm diameter beams with a specified divergence of < 1 mrad.

At this stage the LVIS and mirror-MOT trap beams are combined with repump light using half-waveplates and polarising beam-splitter cubes as shown in Figure 3.7. Some of the repump light is split off on a PBC to be combined with the optical pumping beam. Part of the LVIS trap beam is split off using an optical flat immediately after the fibre decoupler to act as an imaging beam.

Although AOMs attenuate the trap light considerably there is still some leakage due to scattering in the crystal when the rf is removed. Even very small amounts of resonant light can significantly reduce magnetic trap lifetimes. Mechanical shutters (Newport 846) are therefore used to completely block the light in each beam. Rising and falling TTL edges are converted into current pulses to operate the shutters. The shutters are placed on Sorbothane sheets in order to damp mechanical vibrations which perturb and even unlock the lasers. Ideally, the shutters would be suspended above the table to remove mechanical coupling to the lasers entirely. After careful monitoring of the laser behavior during shutter activation this step was not considered necessary.

Most of the optics are contained within a 150×150 cm matte black enclosure to minimise the possibility of stray light and to protect the lasers from acoustic vibrations. The lid of the box is split into six removable sections to allow ease of access to the optics within.

The imaging beam, LVIS and mirror-MOT beams (composed of trap light combined with repump light) and optical pumping beams leave the box through four 8 mm diameter holes in the side. Both the LVIS and mirror-MOT beams have to be expanded, split and polarised correctly in order to form their respective MOTs. The LVIS beam is expanded by a telescope to a diameter of 35 mm. The beam is then split into three beams using two 50 mm polarising beamsplitter cubes and associated half-waveplates. Large gold mirrors then direct each beam to its appropriate position at the LVIS chamber. The mirror-MOT beam is expanded with a telescope to a diameter of 2.5 mm, split into four beams with one-inch PBCs and directed to the main vacuum chamber with gold mirrors.

3.2 The Ultrahigh Vacuum System

Achieving ultrahigh vacuum (UHV) is of great importance in a BEC apparatus. The quality of vacuum ultimately determines the time available for evaporative cooling in a magnetic trap. Reconciling UHV with the need to collect a large number of atoms is a challenge that must be met in every BEC apparatus. Two vacuum systems were constructed, tested and ultimately combined to meet these requirements. The main UHV chamber and vacuum components are described in this section and the procedures for achieving UHV are given in Appendix B.

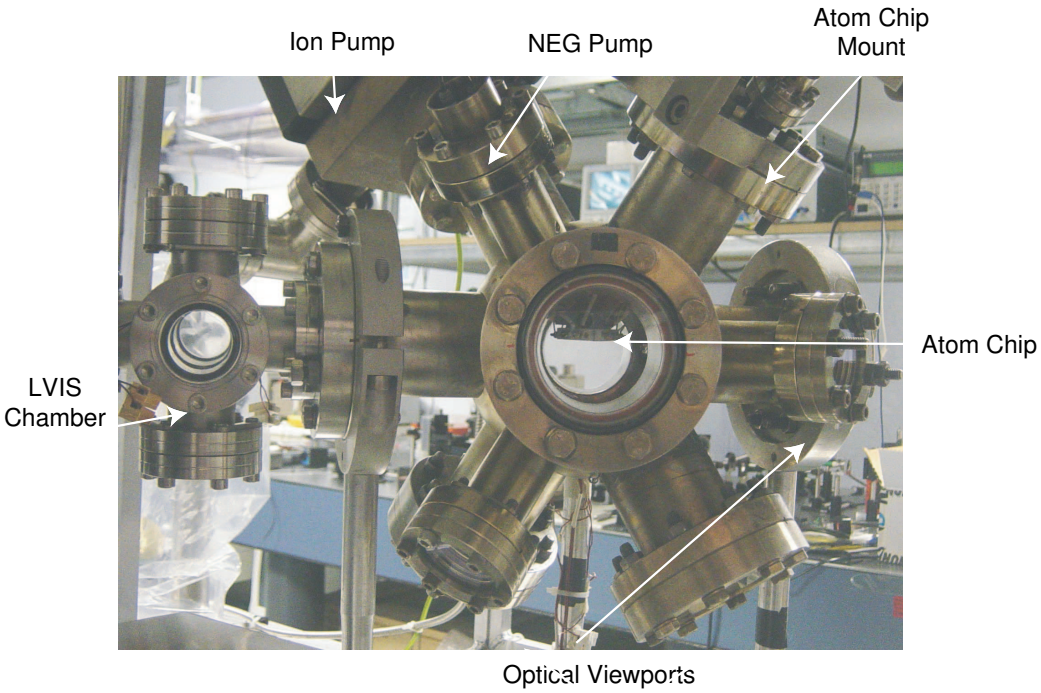

Figure 3.8: The main vacuum chamber with all external coils and optics removed. To the left, part of the LVIS vacuum system can be seen without the main gate valve in place. The silhouette of the atom chip at the centre of the chamber is visible.

3.2.1 The Main Vacuum Chamber

The central component of the vacuum system is what will be referred to as the 'main chamber'. It houses the atom chip, vacuum pumps and optical windows and is made from stainless steel. The geometry is based on a six-inch diameter sphere with fourteen cylindrical ports emerging from the sphere. Six $2\frac{3}{4}''$ long ports with $2\frac{3}{4}''$ flanges are centered on the faces of an imaginary cube and eight $2\frac{1}{2}''$ long tubes with $4\frac{1}{2}''$ flanges emerge from the vertices of the cube. At the end of each tube is a conflat knife edge flange. Copper gaskets are used in all of the conflat connections.

A photograph of the main chamber is shown in Figure 3.8. The chamber has been stripped of all external paraphernalia in the photograph. The main components attached to each port are listed below,

- The "LVIS" chamber based on two six-way crosses (described in Chapter 4) is connected to the main chamber via one of the six large tubes.
- The atom chip mount is attached to a large port on top of the chamber.
- The dispenser mount and feed-through flange used for early experiments without the LVIS is attached to a large port.

- A Star cell (60 l/s) ion pump is attached via a T-piece containing an all metal gate valve used to connect bellows to the chamber for rough pumping. The pump is controlled by a Perkin Elmer Ultek ion pump controller.
- A six inch nipple housing a Varian UHV-24 ionisation gauge operated by a Varian L8350301 Multi-Gauge controller is attached to one of the small ports.
- A non-evaporable getter pump (NEG) (SAES Sorb-AC MK5) [77] was mounted on a small port.
- The remaining eight of the fourteen flanges housed quartz windows for optical access. The four windows normally used for introducing trap light to the chamber were anti-reflection coated.

The chamber was mounted on aluminium posts with its lowest point 17 cm above the optical table to allow optical access from below. To achieve ultra-high vacuum, the chamber was baked each time it was opened to atmosphere, details of which are given in Appendix B.

3.3 Computer Control

An integrated computer control system was developed to oversee the various timing, switching, triggering and ramping tasks necessary for synchronising experimental cycles and data retrieval.

The three main components of the control system were:

1. Hardware to generate signals
2. Software to compile commands, control the hardware and interface with external programs
3. A graphical user interface

Several options were available to combine these elements. The primary concern was reliability and repeatability of timing controls. Software timing using Pascal running under DOS has been shown previously to be reliable for producing trains of TTL pulses with 50 μs resolution [36,47]. However, the main drawbacks included very limited flexibility in the user interface and absence of direct control over analog signals. It has become common practice in modern labs to use the National Instruments (NI) LabView software in combination with NI hardware, often running under Microsoft Windows. National Instruments hardware is readily available and easily configurable. Running in a windows based environment was also appealing because of the ease of use of windows applications in contrast with command-line operating systems. However, by using LabView the user is obliged to sacrifice some degree of control to the operating system: an unfortunate necessity since windows systems are notorious for becoming unpredictable in timing-critical applications. A suitable compromise was to use custom written software that communicated directly with NI hardware through low-level driver commands. By

Part	Purpose of Board	Notes
NI PCI-6534	Digital Pattern Generator	32×5V digital outputs, 2×32 MB of onboard memory.
NI PCI-6713	Analog Output	$8 \times$ 12-bit analog outputs
NI PCI-6524E	Multipurpose Analog I/O	$8 \times$ analog inputs to record analog signals
NI PCI-GPIB	GPIB Controller	GPIB bus communicates with SRS DS345 function generator
Princeton PCI	Camera Interface	Serial CCD camera interface

Table 3.1: Table describing the control hardware installed in the lab PC.

ensuring that all timing signals were generated by the hardware and not the software, such a configuration could be used under windows without any significant compromise.

The programming language chosen was Sun Microsystems' Java Software Development Kit (see for examle [78]). Java is an object orientated language with a large number of useful extension packages available as open source. It is also platform independent, providing potential for distribution of the control software to other architectures. The National Instruments hardware was controlled using the "NIDAQ" drivers written for the C programming language [79]. The low-level routines written in C were translated into Java code using the Java Native Interface (JNI).

3.3.1 Control Hardware

A *Viglen Genie* 2.5 GHz 512 MB RAM PC running Microsoft Windows XP Pro with 5 available PCI slots was used as the main control computer.

Four main tasks had to be fulfilled by the hardware. (1) TTL switching was required for AOMs, shutters, laser frequency etc. (2) Arbitrary voltage ramps were required to control the current in wires and coils used to generate magnetic fields in the system. (3) The generation of arbitrary rf signals was needed for evaporative cooling. (4) Synchronisation with the CCD camera for triggering and data readout was also required.

The PCI hardware boards used to perform the required tasks are listed in Table 3.1 and a guide to the computer hardware is shown in Figure 3.9. The principal component in the control system is the PCI-6534. The board is run as a digital pattern generator and its onboard clock defines the timing for all experimental operations. The 32 MB onboard memory allows digital patterns to be downloaded to the device and stored until triggered. This means it is not necessary to access the computer's memory during the execution of large digital patterns, therefore maintaining timing integrity. An update interval of 20 μs was chosen for the digital patterns. This offers a compromise between resolution and pattern length. The resolution should be large enough that all tasks can be performed with sufficient accuracy but small enough to fit the whole experimental cycle onto the onboard memory of the pattern generator. A 32

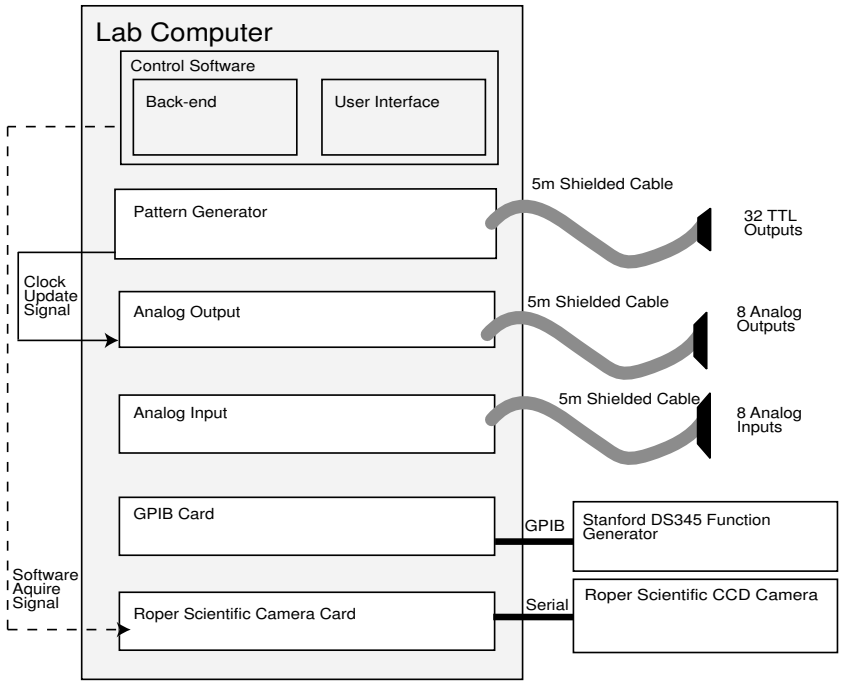

Figure 3.9: Schematic of the control hardware.

bit-wide pattern lasting 160 s can be stored onboard the PCI card with the chosen resolution of 20 μs. A duration of 160 s is sufficiently long for most experimental cycles. Timing resolutions higher than 20 μs are not required during a typical experimental cycle. The shortest repeatable pulse length normally required was for absorption imaging.

The analogue output board (PCI-6713) is used to generate voltage ramps. Unlike the digital pattern generator, it does not have an onboard memory to store voltage values. The digitised voltages are transferred from the computer to a first-in first out 16384 point buffer which updates the output when the clock signal is received from the pattern generator. The analogue output board has 8 channels each with an output range of ± 10 V with 12-bit resolution.

The analogue input board (PCI-6524E) and PCI-GPIB boards were used primarily as part of the rf frequency generation (Section 3.3.5).

The output signals of the digital and analogue boards are sent to 68-pin connectors. Shielded cables ran from the lab-PC to the electronics bench above the optical table. Breakout boxes were constructed to convert the 68-pin cable connectors to BNC outputs using custom printed circuit boards.

3.3.2 Structure of the Control Software

The software was written as a collection of reusable Java classes. Over 100 different classes were included in the source code, making a comprehensive summary impractical here. The class at the heart of the software, the *Experiment* class, represented a single experimental cycle. An

experiment was constructed from *Process* classes which contained information about the state of each TTL line and the initial and final states of the analog and rf ramps and the time duration of the process. A number of routines were written that compiled digital patterns and analog ramps from collections of processes. Finally, the compiled pattern and ramps were sent to the hardware devices and triggered by the *Experiment* class. *Experiment*s and *Process*es had equivalent graphical representations in the 'front-end', but the 'back-end' functionality of the software was separated from the front-end interface so that each could be developed independently. Experiments can be saved and recalled in a custom-written file format.

An important aspect of the control program was also the inclusion of the ability to pre-trigger devices such as shutters by a prescribed time. The measured response time of a device could be saved in the program configuration. When this device was required in the waveform it was pre-triggered by the appropriate time. This allowed events to be synchronised even if they involved several devices with different response times, meaning it was not necessary to explicitly consider the response times when designing waveforms.

3.3.3 Graphical User Interface

The user interface was written using the Java Swing AWT components (see for example [80]). A single process was represented by a collection of text fields to enter names, durations and units, check boxes to determine TTL states and numerical fields to enter the voltages required for analog ramps. Pairs of TTL signals constituting inputs to 4-way multiplexing level-setters were represented by drop-down chooser menus, offering four possible levels as options. Experiments were represented by internal windows consisting of a collection of processes. The overall control application that manipulated the experiment offered a series of toolbar buttons and drop down menus to control the experiments and execute the output. An example of part of the user-interface is shown in Figure 3.10.

The function of each TTL line, analog output and rf output was defined in a central XML file which was loaded by the application. The front end displayed the name of each line accordingly (e.g. "Camera Trigger"). The software remained independent of the experimental configuration and new outputs could be added as the apparatus grew in complexity.

3.3.4 Synchronisation with Imaging Software

Data in experiments is primarily collected by making images of trapped or expanding atom clouds using a CCD camera (Roper Scientific Pentamax) and integration of the control software with image acquisition was helpful. The camera had its own driver and image capture software (Roper Scientific *WinView*), which was used to acquire and process images. To abolish the inconvenience of returning to the WinView software each time the experimental control software was run, a bridge between the two programs was constructed. The bridge made use of the Microsoft COM interface which WinView supports. The C programming language was used to compile executable programs which performed tasks in WinView. The executable program

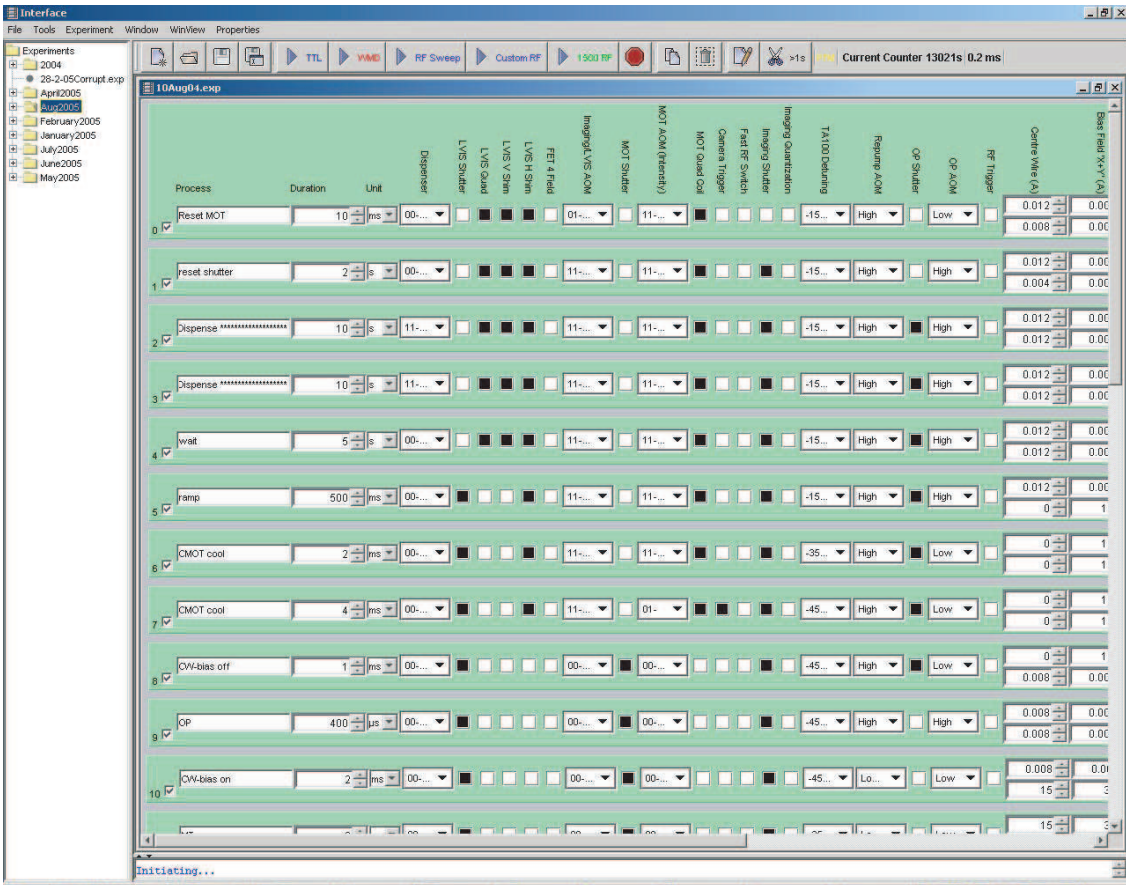

Figure 3.10: A screen-shot of part of the user-interface. Check boxes control TTL lines and level setters. Text fields control voltage ramps etc.

could be run from inside the Java software to perform the desired task in WinView. This method was used to prime WinView for image acquisition before commencing each experimental cycle.

3.3.5 Computer Control of RF Evaporative Cooling

An essential stage of BEC production in a magnetic trap is forced evaporative cooling, usually achieved by driving spin-flips with a time-dependent radio-frequency field in a controlled way. A suitable means of controlling rf signals was necessary for the experiments performed here. Many commercial programable signal generators are capable of producing simple linear frequency ramps. However, the ability to generate arbitrary frequency waveforms is extremely helpful for experimental optimisation of evaporative cooling. For this reason, the ability to generate arbitrary rf waveforms was incorporated into the experimental control interface.

A Stanford DS345 function generator was used to generate rf signals. The DS345 can be programmed by hand via the front-panel or by computer using the GPIB or RS232 interfaces. The GPIB interface was used in early evaporation attempts to generate simple linear or logarithmic frequency sweeps. The start and stop frequencies and duration were entered using the control user-interface. These values were then sent to the DS345 before commencing an experimental cycle. This method had the advantage that the sweep could then be triggered at the appropriate moment by a TTL edge, thus synchronising the sweep with the rest of the experimental cycle. However, the method had the disadvantages of being limited only to linear or logarithmic ramps and allowing only one ramp per experimental cycle.

In order to generate a train of arbitrary ramps, the onboard memory of the DS345 was utilised. The device is capable of storing up to 1500 frequency values which can be uploaded via the GPIB interface. The computer user-interface and control software was used to compile the 1500 values, upload them to the DS345 and then upload a suitably calculated output rate. The significant drawback of this method is that the sweep cannot be triggered with a TTL edge. The only available method of commencing the sweep is to send a command via GPIB. This presents a significant difficulty in maintaining absolute control over the synchronicity of the rf sweep and the rest of the experimental cycle because of the necessity to invoke software timing.

The arbitrary frequency sweeps were triggered at the appropriate moment using the following method. A TTL line acting as an rf trigger was designated and set to change state when the first rf sweep was required. This line was fed-back into one of the channels of the analog input board (PCI-6524E). The computer then entered a loop in which it monitored the analog input, looking for a change in voltage. When the trigger was detected, the computer then sent the appropriate software command via GPIB to commence the sweep. The software loop slept for 1 ms between checks, introducing a shot-to shot uncertainty in the repeatability of the rf trigger point of $\simeq 1$ ms.

The ability to produce arbitrary rf waveforms proved to be extremely successful in designing the evaporation trajectories. The uncertainty introduced by the software loop was not critical

although it would be desirable in future to use a function generator that can be triggered with a TTL pulse. This would eliminate the need for software timing anywhere in the computer control system altogether.

The atom chip, which lies at the heart of the vacuum chamber is described in the next section.

3.4 The Videotape Atom Chip

The atom chip was constructed to serve the dual purposes of mounting the videotape and housing macroscopic current carrying wires for manipulating atoms. The atom chip is described in detail in Reference [47] and only a summary of the chip construction is given here.

The chip consists of a 1 inch square stainless steel block. Several channels are cut in the block to accommodate 5 wires made from ceramic-coated copper. The principal wire, used to form a guide as described in Section 5.1, bisects the chip and will be referred to as the 'centre wire'. It has a 500 μm diameter and lies with its upper surface parallel to the surface of the block and runs along the z-direction. Two additional wires of 1 mm diameter, the 'end wires', run in separate channels in the x-direction with their upper surfaces beneath the centre wire. Two further wires of 500-μm diameter run parallel to the centre wire and are connected to make a loop which we use as an rf antenna for evaporative cooling.

The videotape used in the atom chip is *Ampex 398 Betacam SP* with a 3.5 μm thick magnetic layer and a width of 12.5 mm. The magnetic layer consists of iron-composite needles that are 100 nm long and have a radius of 10 nm, set in glue and aligned along the x-direction [81]. The videotape is recorded with a sinusoidal signal with a nominal wavelength of 100 μm. Measurement of the wavelength gives a value of $106 \pm 2\,\mu$m [47].

To complete the chip the magnetised videotape is glued to a 150-μm-thick glass coverslip (22 mm $\times$ 22 mm) using UHV compatible epoxy (Bylapox 7285) and then coated with a thin layer of gold. The coverslip is glued in turn to the surface of the steel block. A photograph of the surface of the atom chip is shown in Figure 3.11 with each of the wires labelled. This also defines the coordinate system used extensively when describing the experimental system. The distance from the axis of the centre wire to the surface of the chip is the sum of the wire radius, the glass coverslip thickness, the videotape thickness and the total thickness of glue used. A cross-section through the chip showing the centre wire and the dimensions of the components glued above it is shown in Figure 3.12. Each of the wires on the atom chip is connected internally to one of two multi-pin vacuum feed-throughs to allow electrical connections to be made. Ceramic beads are threaded onto the wires to reduce the possibility of their touching. The gold coated atom chip is mounted on a stainless steel stalk and positioned at the centre of the main vacuum chamber, where it can be manoeuvered on a millimeter-scale using a translation threads mounted on UHV bellows.

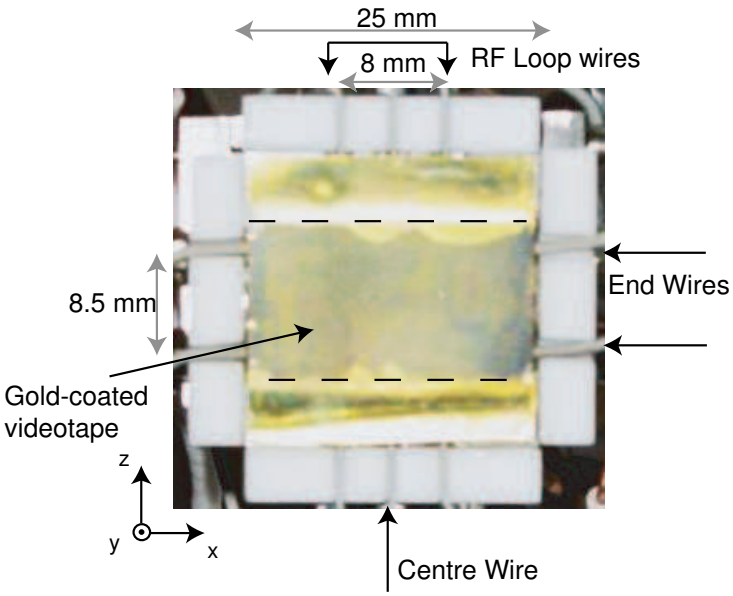

Figure 3.11: The surface of the atom chip. The wires running beneath the surface are labelled. The dashed lines indicate the boundaries of the videotape.

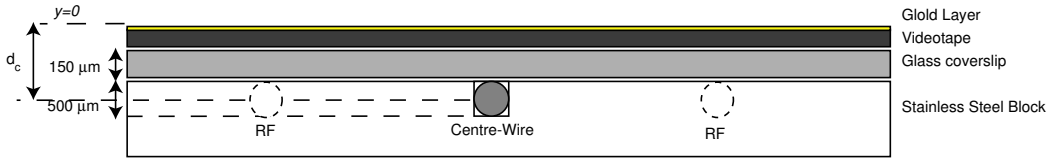

Figure 3.12: A schematic cross section through the atom chip depicting the centre wire and the videotape mounted above it (not to scale).

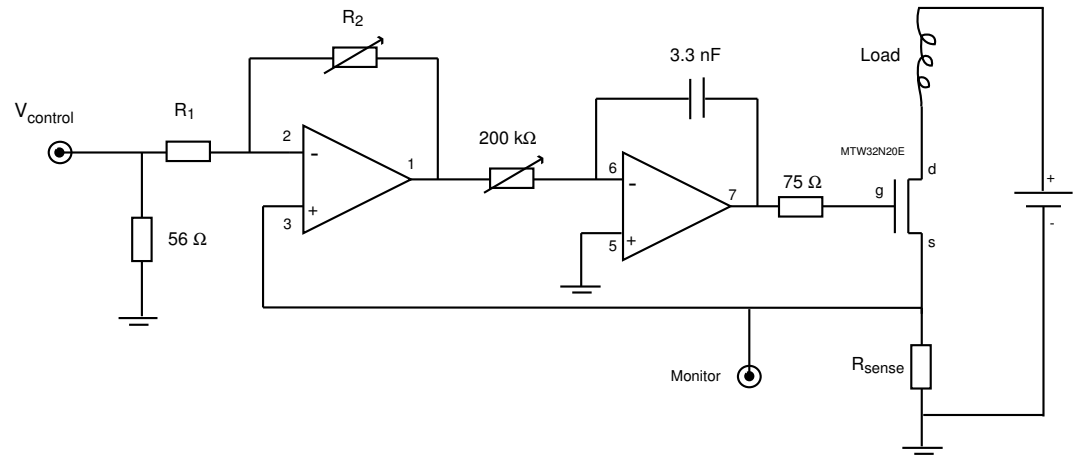

Figure 3.13: FET control circuit used to control and stabilise the currents running through the wires and coils. R_{sense} is typically 0.47 Ω.

3.5 Generation of Magnetic Fields

Various magnetic fields generated by coils and current-carrying wires are applied during an experimental cycle. The fields must be controllable by computer and stable. The fields generated by external coils are outlined below followed by a description of the way the currents are controlled and stabilised.

3.5.1 Magnetic Field Coils

The principal uniform magnetic field used in the formation of magnetic traps, the bias field B_{bias}, is formed by coils of 100 turns each, forming two Helmholtz pairs on axes orientated at 90° to each other. The coils have a diameter of 10 cm and are mounted directly over the chamber viewports. One pair of bias coils produces fields of up to 35 G at the centre of the chamber with the two coils wired in series with each other. With both pairs carrying equal current the field is orientated along the x-direction. A pair of anti-Helmholtz quadrupole coils, described in Section 4.3.1 is mounted over one of the pairs of bias coils.

Another pair of coils in Helmholtz orientation of 100 turns each creates a uniform field in the z-direction to reduce the z-component of the field due to the end wires, producing fields of up to 25 G if required. A set of 60×40 cm and 40×40 cm rectangular coils surrounding the chamber with provides additional magnetic fields up to ~ 1 G which can be used to apply small offsets and cancel the Earth's magnetic field.

3.5.2 Magnetic Field Control

The currents in the wires and coils must be stable to approximately 1 part in 10^4. FET driver circuits of the kind shown in Figure 3.13 are used to regulate the current and to allow computer control the fields by applying a variable voltage to $V_{control}$. The first part of the circuit provides

differential feedback, stabilising the voltage with respect to the control voltage, followed by an integrator. The voltage applied to the gate of the FET regulates the current flowing through the load and sense resistor on the high power side of the circuit. The choice of resistors R_1 and R_2 determine the current flowing in the circuit for a given control voltage. Circuits similar to that in Figure 3.13 were constructed for the pair of bias coils, the centre wire and end wire, the B_z cancelling coils. The high power for these circuits was supplied by Isotech ISP and Tenma switch-mode power supplies and sense resistors of $0.47\,\Omega$ or $0.1\,\Omega$ were used depending on the load resistance. The FETs and sense resistors were mounted on water-cooled copper heat sinks to dissipate the heat generated by the FETs and stabilise the temperature of the sense resistors. Additional FET control circuits that were not water cooled were used to drive the mirror-MOT quadrupole coils, rubidium dispenser, shim fields and the LVIS quadrupole field coils (Chapter 4).

The FETs themselves need to be able to dissipate several hundreds of Watts of power when operating at around a few Amps. To prevent overloading the FET, the voltage of the power supply should be set to the maximum required to drive the load but not more than this, in order to limit the excess power that must be dissipated in the FETs at intermediate currents. It is also important to apply a small voltage ($\sim 10\,\mathrm{mV}$) to the input of the FET circuits at all times to prevent the input going negative and causing switch on delays due to the integrator response.

3.6 Absorption Imaging

Absorption imaging is used to probe magnetically trapped and expanding atom clouds. This is achieved by illuminating the cloud with a resonant or near-resonant probe beam and imaging the beam profile on a CCD camera chip. The shadow cast in the beam as a result of photon absorption by the intervening atoms yields a two-dimensional profile of the atomic density distribution. The absorption in the low intensity limit ($I_{probe} < I_{sat}$) is exponential with optical thickness, as described by Beer's law. Considering transmission of the probe beam along the x-direction, the transmitted intensity profile after passing through the cloud is given by

$$I'(y,z) = I_0(y,z)\exp(-\sigma_L \int n(x,y,z)dx) \tag{3.1}$$

where $I_0(y,z)$ is the probe beam profile and σ_L is the atomic absorption cross section. For a two level atom the cross section is given by

$$\sigma_L = \hbar\omega\frac{\Gamma}{2}\frac{1/I_{sat}}{1 + I/I_{sat} + 4(\frac{\delta}{\Gamma})^2} \tag{3.2}$$

where I_{sat} is the saturation intensity, δ is the detuning and Γ is the natural linewidth.

By taking the natural log of the intensity profile after passing through the cloud the 2D density distribution is recovered

$$n_{2D}(y,z) = -\frac{1}{\sigma_L}\ln\left(T(y,z)\right) \tag{3.3}$$

where transmitted profile $T(y,z)$ is obtained from the normalisation $\frac{I'(y,z)}{I_0(y,z)}$. The atom number can in general be obtained from a processed image by summing over the cloud

$$N = -\frac{dxdy}{\sigma_L}\sum \ln(T(y,z)) \tag{3.4}$$

where dx and dy are the dimensions represented by a pixel in the object plane. The duration of the imaging pulse should be short enough that the atoms do not move far as a result of the radiative recoil yet long enough to provide sufficient signal-to-noise by stimulating enough counts in each CCD camera well. A typical pulse length used in these experiments is $40\,\mu$s. For circularly polarised light on the $F = 2 \rightarrow F' = 3$ transition the two level model is justified because optical pumping causes the atoms to enter the $m_F = 2$ state and continuously scatter into the $m'_F = 3$ state. In addition, no repump light is needed in the imaging beam because the transition is closed.

3.6.1 Imaging System

Absorption imaging is performed with a weak probe beam of typically $300\mu\mathrm{W/cm}^2$ for which $I/I_{sat} = 0.18$. The image is formed using a $2f$ lens arrangement. Before entering the chamber the beam passes through a linear polariser and a $\lambda/4$ plate to circularly polarise the beam. The geometry of the vacuum chamber constrains the beam to pass across the atom chip at an angle of θ to the x-axis where θ was usually $33 \pm 2\,^\circ$. After transmission through the chamber, the beam passes though a 2.54 cm diameter achromatic lens with a focal length of 10 cm placed outside the chamber window and mounted on a micrometer stage to allow fine positioning of the lens. The $2f$ arrangement allowed florescence images to be taken using the same lens (Section 4.3.2).

A schematic representation of the imaging system is shown in Figure 3.14. The coordinates in the frame of the image are denoted by primes (x', y', z') and in order to transform between the coordinates in the frame of the atom chip and the image with unit magnification the relation

$$z' = z\cos\theta + x\sin\theta \tag{3.5}$$

must be used. For imaging Gaussian shaped clouds this results in transformed widths of $\sigma'_z = \sqrt{\sigma_z^2\cos^2\theta + \sigma_x^2\sin^2\theta}$. In most cases cylindrical symmetry applies and σ_x and σ_y are interchangeable. If the camera is also tilted by ϕ there is an additional correction in the z-direction of $z'' = z'\cos\phi$.

Two separate Princeton Instruments PentaMax cameras with different CCD chips were used for data acquisition in the experiments at different stage. These had 6.8 and $9\,\mu$m square pixels

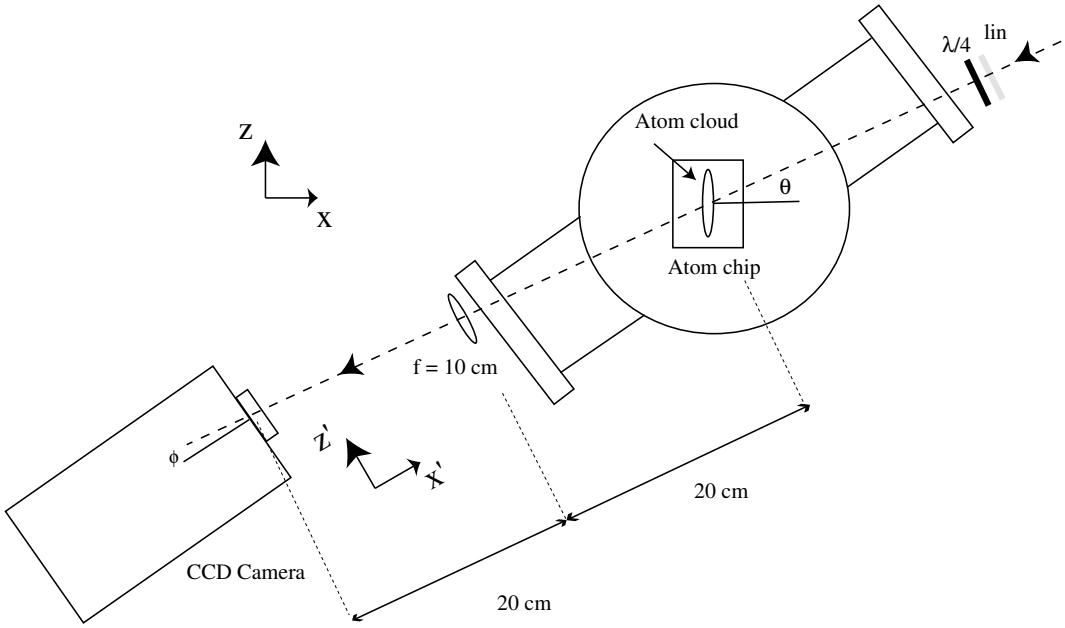

Figure 3.14: Schematic diagram of the $2f$ imaging arrangement. The probe beam enters the chamber from the right after being circularly polarised. A high-quality achromatic lens forms an image on the CCD camera chip. The angles θ and ϕ determine the magnification in the z-direction.

Chip	Dimensions	Pixel Size	Digitisation	Sensitivity at 780 nm
Kodak-768	768×512	$9 \times 9\,\mu$m	12 bit	0.019 counts/γ [47]
Kodak-1035	1317×1035	$6.8 \times 6.8\,\mu$m	12 bit	0.026 counts/γ [36]

Table 3.2: Properties of the two CCD camera chips used in the experiments.

and properties of the two camera chips are given in Table 3.2. Both cameras were electronically cooled to -30°C. A limited region of interest was read out to reduce the time needed between shots to typically 150 ms. The Kodak-768 camera was tilted by an angle ϕ which was usually $20 \pm 1°$ to prevent unwanted fringes in the image. The Kodak-1035 camera was not usually rotated.

3.6.2 Double Imaging Technique

An important advance in the work described in this thesis was the ability to directly image atoms trapped in a videotape microtrap. The videotape microtraps form generally less than 100 μm from the surface of the chip and previously it was very difficult to observe atoms this close to the surface due to the slight overhang and bowing of the videotape. By taking advantage of the gold mirror on the surface of the chip, it is possible to reflect the probe beam off the surface of the chip, thereby forming an image of the atom cloud and its reflection in the

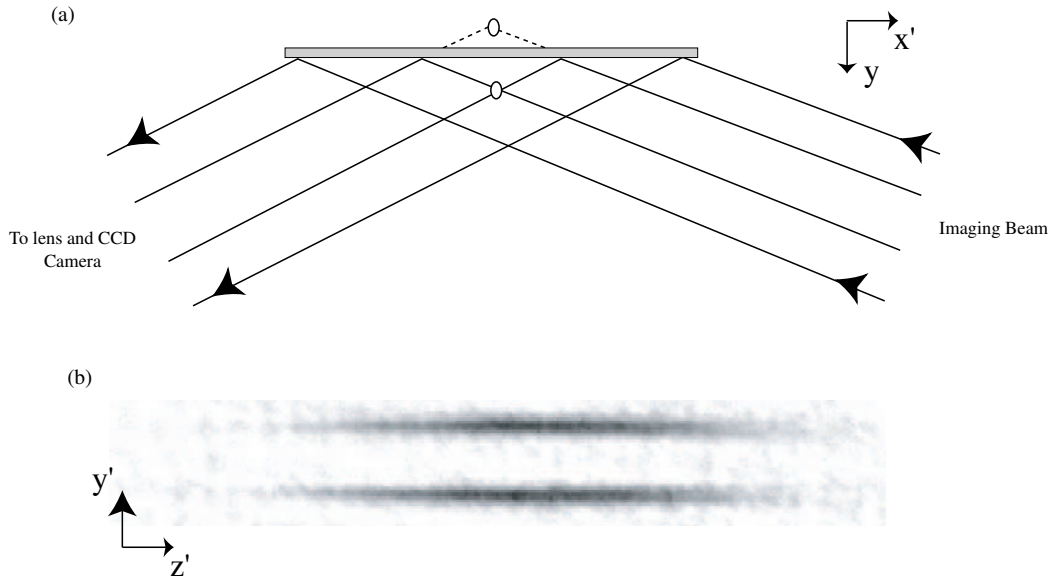

Figure 3.15: Schematic diagram of the reflection imaging technique. (a) The probe beam bounces off the chip, producing a double image of the atom cloud. (b) A double image formed using this technique.

mirror. This technique allows a clear image of the cloud in the videotape trap to be obtained and has the significant added advantage of allowing the atom surface distance to be determined accurately from the separation of the two images.

A schematic representation of the reflection imaging and an example of an absorption image are shown in Figure 3.15. The probe beam was typically reflected off the chip at an angle of $\simeq 10\,^\circ$ and the lens and CCD camera were tilted back by the same amount to ensure the beam passed through the lens on axis. In this orientation, the atom-surface distance is given by half the distance between the image and its reflection. Almost all of the data relating directly to the videotape microtraps in this thesis was obtained using this method. However, for imaging MOTs and magnetic traps far from the surface ($y_0 \gtrsim 1\,\mathrm{mm}$) the probe beam was not reflected off the chip surface.

Abberations due to the chamber viewports and reflection off the non-ideal surface of the chip mean that the optical resolution limit of the imaging system is somewhat larger than the $7.5\,\mu\mathrm{m}$ diffraction limit set by the lens. The radial size of ultracold clouds and condensates viewed in absorption images gives some indication of the resolution limit. The smallest radial half-widths of fits to *in situ* absorption images was $\sigma_r \simeq 1.5$ pixels or equivalently $24\,\mu\mathrm{m}$ FWHM. The resolution was not a severe limitation because that the axial length rather than the radial size was principally used to obtain temperature measurements for *in situ* images. This resolution could probably be improved by using high-quality quartz viewports and making a smoother atom chip mirror surface for the reflection imaging.

3.7 Summary

Having described the laser, vacuum and computer control systems as well as summarised the atom chip and magnetic field and imaging arrangements the next chapter will present details of the laser cooling and trapping stages of the experiment.

Chapter 4

Low Velocity Atom Source for a Mirror-MOT

Laser cooling and trapping is an essential starting point for all experiments that have produced BEC in a dilute alkali vapour. The conditions achieved in the laser cooling stage critically determine the subsequent success of the experiment. Magneto-optical traps offer an efficient way to capture large ensembles of cold atoms and cool them to micro-Kelvin temperatures. However, the high-vapour pressures needed to accumulate the largest number of atoms are not commensurate with the ultra-high vacuum conditions normally required to obtain BEC. Various techniques to combine large atom numbers with ultra-high vacuum have been established with varying success and technical complexity. This chapter describes the realisation of one particular technique, a low-velocity intense source, which is used to load a magneto-optical trap close to a room temperature surface. The design, construction and operation of the source is presented, followed by a description of the operating conditions of the surface-MOT. The methods used to further cool the atoms and prepare them for transfer into a purely magnetic trap are then described.

4.1 Laser Cooling

The field of laser cooling and trapping is now well-established in atomic physics and is described in the extensive literature. Broad reviews of the field are available in References [82] and [83]. These sources contain many citations of important work in laser cooling including slowed atomic beams, optical molasses, Doppler and sub-Doppler cooling, vapour cell magneto-optical traps and novel cooling methods.

This chapter focuses on two particular systems employing laser cooling techniques, the low velocity intense source of atoms (LVIS) [84] and the mirror-magneto-optical trap (mirror-MOT) [85]. Both of these have been touched upon in the previous chapter but here they are presented in more detail. The LVIS provides a beam of cold atoms from a slightly modified standard MOT. The mirror-MOT allows the collection of cold atoms within a few millimeters

of a reflecting surface, a convenient precursor to transfer into a purely magnetic surface trap. In this work the two techniques were combined to achieve large atom numbers in a mirror-MOT while simultaneously maintaining excellent vacuum conditions. In the next section some possible methods of loading a MOT are briefly discussed to motivate the adoption of an LVIS.

4.1.1 Slow Atomic Beams

An early demonstration of atomic manipulation by lasers was the deceleration of a thermal beam from an oven source [86]. Subsequently, cooling in three dimensions was demonstrated [87] followed by three dimensional magneto-optical trapping [88]. In 1990 Monroe *et. al.* [89] demonstrated that a magneto-optical trap could be loaded directly from a background vapour without the need for complex beam slowing apparatus. Vapour-cell MOTs have been used extensively in laser cooling applications. However, the relatively high background pressures required to load the MOT ($\sim 10^{-7}$ torr) render them unsuitable for applications where long lifetime is critical. In such situations it is common practise to spatially separate the high-vacuum MOT from an independent source of atoms and use differential pumping to maintain good vacuum. The choice then arises between loading from a slowed thermal beam or from atoms out-coupled from another high-pressure MOT. In both cases, the magnitude of the flux of atoms from the source is one of the most important quantities.

Zeeman slowing [86] and chirped cooling [90] are two very successful methods for slowing a thermal beam. Zeeman slowers can be physically very long ($> 1\,\mathrm{m}$) and are therefore not a practical choice for a miniature atom optics experiments such as this one. Chirped cooling achieves slowing by sweeping the frequency of the laser in a time dependent manner. Modulation of the laser frequency, although reasonably easily achieved with diode lasers, is an undesirable complexity. Despite the historical success of slowed beams, many atom optics experiments now adopt a double-MOT approach.

In a double-MOT system a primary MOT operating at high vapour pressure and laser intensity provides a source of atoms for a secondary low-pressure 'science' MOT. The transfer is usually performed with a resonant 'push' laser beam [91] which can be combined with the force of gravity [18] to transport atoms between the MOTs. The primary MOT is traditionally loaded from a constant background vapour. However, heated alkali getters offer a compact, clean, switchable source of atoms and have been used successfully in many atom optics experiments [92].

A variation on the double MOT is the 2D MOT [93] in which cooling and trapping in the primary MOT are performed in two dimensions and an atomic beam emerges along the 3^{rd} axis. The 2D-MOT configuration has been successfully extended to include cooling in the 3^{rd} direction using the so-called $2D^+$ MOT [93, 94].

The LVIS [84] is a particulary simple and compact source of atoms offering high output fluxes and was adopted in the present work.

Before discussing the LVIS in detail it is worth noting that slow atomic beams have generated

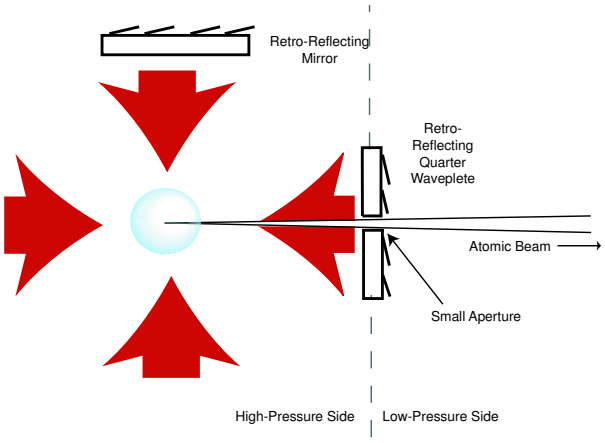

Figure 4.1: The principle of operation of the LVIS. The rectangles are retro-reflecting optics. Another pair of beams into and out of the page to complete the 6-beam MOT are not shown. The dark column in the reflected beam produces the output flux of atoms.

significant interest in their own right as a means of continuously loading a magnetic guide. The authors of [95] used an LVIS to load a magnetic guide on an atom chip. Similar methods could be used to replenish a Bose condensate with the aim of making a CW matter-wave laser [96].

4.2 The Low Velocity Intense Source of Atoms (LVIS)

The LVIS operates on the same principle as the standard 6-beam vapour cell MOT with an important modification. One of the six beams has a dark column in its centre, created by an aperture in one of the retro-reflecting optics. Atoms are captured from the background gas by the six laser beams and directed to the centre of the trap by a standard MOT quadrupole field. When an atom enters the dark column in the centre it is accelerated out of the MOT by the radiation pressure due to the unbalanced counter-propagating beam. The principle of extraction of atoms in from the LVIS is outlined in Figure 4.1.

The aperture in the retro-reflecting optic is made deliberately small (mm-scale) to limit the molecular conductance of the aperture. By choosing the pumping speed on each side of the aperture appropriately, a large pressure differential can be maintained between the LVIS chamber and the secondary chamber, as will be discussed in Section 4.2.3.

The flux of atoms Φ out of the system is given by [84]

$$\Phi = \frac{R}{(1 + \frac{\Gamma_B}{\Gamma_t})} \tag{4.1}$$

where R is the loading rate from the background vapour, $\Gamma_B = 1/\tau_B$ is the rate of collisions with the background gas and Γ_t is the transfer rate of atoms into the extraction column. The time-scale $1/\Gamma_t$ is comparable with the atomic damping time in molasses which is of the order

of milliseconds. The background losses occur on a longer timescale, allowing the approximation $\Gamma_B \ll \Gamma_t$ to be made. This results in $\Phi \simeq R$, meaning that the flux of atoms out of the LVIS is approximately equal to the capture rate into the LVIS MOT. The equivalence of loading rate and flux in the case of the LVIS means that the usual steps to maximise MOT loading such as high power and large beams are desirable for increasing the LVIS flux. In Reference [94] the authors combine Equation 4.1 with an additional loss term which takes into account atoms specifically lost from the extraction column due to collisions with atoms in the background vapour. These atoms are less robust to being lost due to collisions than atoms fully confined in a MOT. The absolute value of this loss rate is difficult to quantify and measure without clear knowledge of the time-dependent vapour pressure and collision cross-section. However, it is enlightening to be aware that the output flux is restricted at very high vapour pressures.

Having introduced the LVIS in principle, the particular LVIS constructed and operated in the work presented in this thesis will now be described. As a point of terminology, the word 'LVIS' will be used henceforth to describe the physical device constructed in the laboratory, rather than simply the principle of producing a low-velocity intense source of atoms.

4.2.1 The LVIS Vacuum System

An LVIS similar to the one described in Reference [84] was designed and constructed. Although compactness is desirable in efforts to miniaturise components used for atom optics, there were no serious constraints on space that precluded the use of standard vacuum hardware to build the LVIS. The LVIS was constructed from two $2\frac{3}{4}$ inch conflat 6-way crosses separated by a T-piece. The first 6-way cross, closest to the main chamber, accommodated the MOT region and four windows to introduce light to the chamber. A conflat-mini viewport was welded onto the corner of the 6-way cross to provide a viewing window for the LVIS MOT that was free from scattered laser light and which proved essential in LVIS-MOT diagnostics.

The second 6-way cross incorporated a window for the pushing beam and ports to attach additional equipment including a 20 l/s ion pump and two small all-metal gate valves. The interconnecting T-piece housed the rubidium dispensers, mounted on a four-pin vacuum feed-through. Figure 4.2 is a schematic diagram depicting the most important LVIS components.

4.2.2 LVIS Extraction Mirror

The principal component required for the LVIS is an optic with a hole for the extraction of the atoms. A 6 mm thick 32 mm diameter custom made Comar $\frac{\lambda}{4}$ waveplate was drilled with a 1 ± 0.2 mm diameter hole at the centre. The back face of the waveplate was then coated with a layer of aluminium to make it reflective. The coated waveplate is 70 % reflective for 780 nm light. A mount for the waveplate was machined from stainless steel and the waveplate was then glued onto the mount with vacuum compatible epoxy around the edges.

The LVIS mirror mount assembly was attached to a $2\frac{3}{4} \rightarrow 4\frac{1}{2}$ inch adaptor flange. The

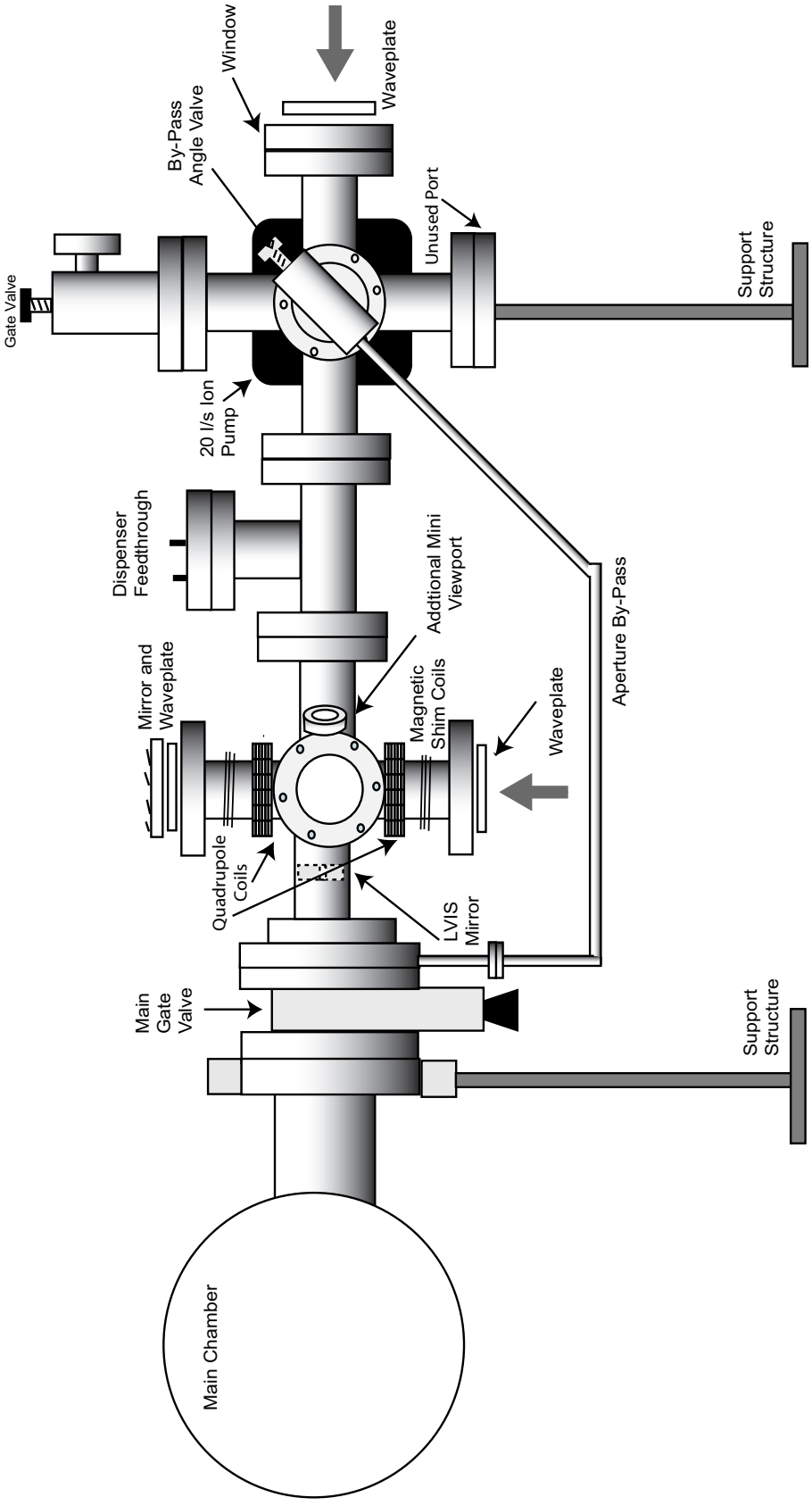

Figure 4.2: A schematic diagram of the LVIS vacuum components viewed from the side. The main chamber is shown to the left with all of its other ports omitted for clarity. Many of the clamps and mounts which attach mirrors and waveplates to the chamber are also omitted for clarity.

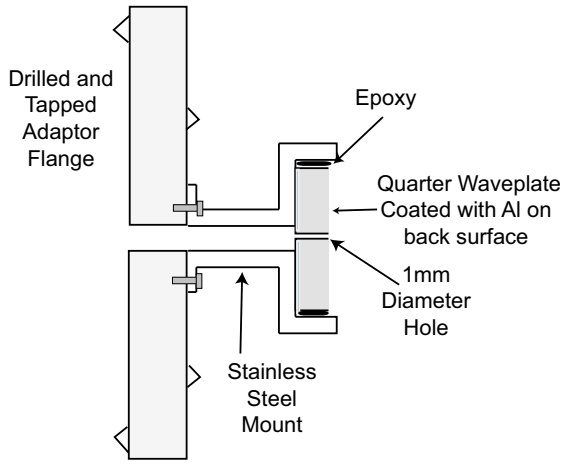

Figure 4.3: Cross-section of the LVIS mirror assembly attached to the adaptor flange.

mount was screwed into three tapped holes in the flange. Figure 4.3 shows a cross-section through the mirror-assembly. The adaptor flange served to mount the LVIS vacuum system on the main chamber. Initially the LVIS was attached directly to the main-chamber with the adaptor flange. However, it proved particulary useful to include a gate valve between the main-chamber and the LVIS. This 'main-gate valve' allowed independent maintenance and baking of the either the LVIS or main-chamber without disturbing the vacuum in the adjacent chamber.

4.2.3 Pressure Differential

The 1 mm diameter × 6 mm long aperture in the LVIS mirror provides the only route for gas transfer between chambers. Differential pumping allows several orders of magnitude difference in pressure between the LVIS and main chamber to be maintained. The difference in pressure is determined by the conductance of the aperture.

At ultra-high vacuum pressures, gas transfer through a small aperture such as this may be treated in the molecular flow regime. The conductance C in l/s of a tube of diameter d and length l is conveniently expressed by [97]

$$C = 12\frac{d^3}{l} \tag{4.2}$$

where d and l are given in centimeters. According to Equation 4.2 the conductance of the LVIS aperture for air is 0.02 l/s. The conductance is about 0.01 l/s for rubidium.

A 60 l/s ion pump operates in the main chamber. Taking into account the pump housing the effective pumping speed S_e at the centre of the chamber is approximately 45 l/s. The throughput of a pumping system is given by $\dot{Q} = PS_e$ where P is the pressure and S_e is the effective pumping speed. The throughput of a tube with conductance C is

$$\dot{Q} = C(P_u - P_d) \tag{4.3}$$

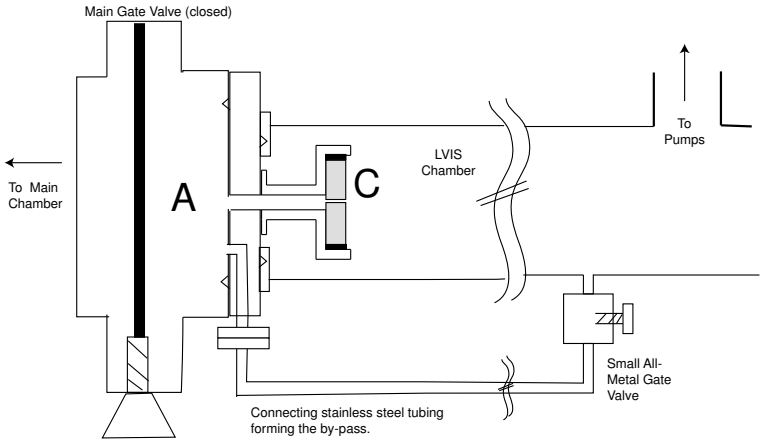

Figure 4.4: Cross-section illustrating how the part of the chamber labelled **A** can be pumped out by the LVIS main pumps through the connecting tubing without pumping solely through the low conductance aperture, labelled **C**. When the large gate-valve is open, region **A** is pumped on by the main-chamber pumps.

where P_u and P_d are the upstream and downstream pressures respectively.

Since throughput is conserved we can use Equation 4.3 to obtain the pressure differential, neglecting the contribution due to pumping by the stainless-steel walls. If we define the ratio of the low-pressure chamber to the high-pressure chamber as $\kappa = \frac{P_{low}}{P_{high}}$ then rearrangement of Equation 4.3 gives

$$\kappa = \frac{1}{\frac{S_e}{C} + 1} \simeq \frac{C}{S_e} \tag{4.4}$$

where S_e is the effective pumping rate and C is the conductance of the tube and $S_e \gg C$. Given the pumping speed in the main chamber, $\kappa = 4 \times 10^{-4}$ for the pressure differential between the LVIS and the main chamber.

In normal practise, no influence of raising the pressure in the LVIS chamber by dispensing atoms could be observed on the ionisation-gauge in the main chamber, which continued to read $\sim 1 \times 10^{-11}$ torr.

4.2.4 Low Conductance Aperture By-Pass

When the main-gate valve is closed there is a region of the LVIS chamber between the main-gate-valve and the 1 mm LVIS mirror that is isolated from the rest of the system, as shown in Figure 4.4. This region is only pumped through the low conductance aperture. To prevent gas remaining trapped in this region during pump-down of the LVIS, a by-pass was installed connecting this region directly to the LVIS chamber. To construct the by-pass a tube was drilled through the body of the adaptor flange, connecting the outside edge with the central bore. A conflat-mini connector was welded to the outside edge of the adaptor flange. Stainless steel tubing (6.3 mm diameter) was used to connect this mini-flange to the rest of the LVIS chamber.

A small gate valve was installed as a means of opening and closing the by-pass. The main features of the by-pass can also be seen in Figure 4.4. Initially, the by-pass was constructed from Swagelok fittings with a needle valve acting as the by-pass switch. However, leaks in this system prevented achievement of UHV in the LVIS chamber, prompting the replacement of the Swagelok with welded fittings and replacement of the needle-valve with a UHV all-metal gate-valve.

4.2.5 LVIS Magnetic Fields

A pair of coils in anti-Helmholtz orientation provide the quadrupole magnetic field for the LVIS MOT. Due to the construction of the main 6-way cross, a minimum separation of 5.6 cm is necessary. The coils had to be be wide enough to fit over the ends of the conflat flanges so that they could be easily removed for bakeout.

The diameter of each coil was 8.6 cm. The resulting axial field gradient is 0.054 G/cm per Amp-turn. The coils were wound with 55 turns each and the normal operating current for the LVIS coils is 2.2 A, giving a field gradient of 7 G/cm along the axis of the coils.

In order to make fine adjustments to the position of the quadrupole zero, extra shim coils were added to the LVIS. One pair produced a uniform field in the vertical direction and another pair produced a field along the horizontal axis, both perpendicular to the atomic beam axis. The coils were wound directly onto the body of the 6-way cross. These shim field were essential in optimising the flux out of the LVIS, second only to beam laser beam alignment in importance.

4.2.6 The LVIS Atom Source

Initially a rubidium sidearm was tested as the source of atoms for the LVIS. The sidearm consisted of a glass tube containing rubidium metal separated from the chamber by a needle valve. An external heating element was used to control the temperature of the sidearm. In practise it proved difficult to regulate the sidearm vapour pressure despite regular heating to 70°C or more. Overheating eventually caused the glass to fracture and the sidearm was removed.

Alkali metal dispensers proved a much more satisfactory source of atoms. Two SAES Getters rubidium dispensers were attached to a vacuum feedthrough and mounted 7 cm away from the edge of the LVIS trapping region. During a bakeout one dispenser became un-useable and the other became shorted to the vacuum chamber and therefore grounded. The dispenser could still be operated using a floating power supply, however, in this condition the current was either on or off. It was therefore not possible to keep the dispenser warm between cycles by running 2 A through it as is customary [92]. Consequently, it is necessary to run the LVIS dispenser for up to 20 s, including time for it to warm up, in order to achieve the maximum loading rate in the LVIS MOT.

4.2.7 Operation and Testing of the LVIS

The LVIS was constructed and tested separately from the main-chamber. Once atoms were trapped in the LVIS MOT (visible by fluorescence) evidence of an atomic beam was sought. A security camera was set up to look in through the conflat-mini window welded to the LVIS chamber. We looked for fluorescence in the output beam in 'pulsed' mode after the MOT was allowed to fill away from the extraction column and rapidly (in several ms) moved into the centre using one of the shim fields. A short pulse of florescence as atoms were pushed out of the MOT could be seen on examination of a slow-motion playback. This provided sufficient initial evidence that the LVIS was capable of providing an output flux to instigate attaching it to the main chamber. Successful loading of the mirror-MOT from the LVIS beam was observed immediately on the first occasion that the main gate valve was opened.

The longitudinal velocity of the LVIS beam and the transverse velocity spread are important quantities determining the performance of the LVIS as a source of cold atoms. Both of these quantities can in principle be measured using standard atomic beam time-of-flight techniques. Attempts were indeed made to record the time-dependent fluorescence from the LVIS atomic beam. However, insufficient signal was collected with photodiode 20 cm away from the probe beam to make any quantitative measurement of the time-of-flight profile. In an alternative attempt to measure the beam velocity, the time delay between initiating a pulse of atoms from the LVIS and the onset of mirror-MOT fluorescence was measured. Uncertainty in the absolute time at which the mirror-MOT begins to fill means this method merely sets a lower limit on the beam velocity ($\geq 10\,\mathrm{m/s}$) and reveals no useful information about the transverse velocity spread. In principle it would be possible to install a small viewport less than 1 cm away from the LVIS beam and use a photo-multiplier tube to collect the fluorescence in a time-of-flight measurement. However, this step was not considered necessary since in practise the mirror-MOT loads particulary well from the LVIS. Table 4.1 summarises the beam velocities measured by a selection groups who have measured the longitudinal beam velocity of their LVIS. Measured beam velocities fall within the range of $8 - 26\,\mathrm{m/s}$. This velocity range compares closely with typical MOT capture velocities and the successful loading of the mirror-MOT from the LVIS in our experiment is a good indication that our LVIS operates within this standard range of velocities.

In addition to the beam velocity, the beam flux is an important property of the LVIS. The highest output fluxes from the LVIS were obtained by following a careful experimental optimisation procedure. The relative flux was optimised by maximising the loading rate of the mirror-MOT. The single most important factor in maximising LVIS flux was the total power in the LVIS beams. This is unsurprising considering that the flux is directly related to the loading rate and hence the capture velocity. Once all available power was delivered to the LVIS (typically a total power of 100 mW) the flux could be optimised by fine alignment of the push beam or positioning of the quadrupole zero using the shim fields.

To highlight the importance of the accurate positioning of the quadrupole centre of the LVIS

Group	Hole	Flux	Velocity	$1/e^2$	Gradient
Lu *et. al.*, JILA [84]	1 mm	5×10^9/s	14 m/s	4 cm	5 G/cm
Jun *et. al.*, Seoul [98]	2 mm	8×10^8/s	11 m/s	-	13 G/cm
Cacciapuoti *et. al.*, Naples [99]	N/A	7×10^7/s	14 m/s	1 cm	15 G/cm
Dieckmann *et. al.*, Amsterdam [93]	0.8 mm	3×10^8/s	26 m/s	0.7 cm	14 G/cm
Ovchinnikov, NPL [100]	2 mm	8×10^9/s	8.5 m/s	2.5 cm	6 G/cm
LVIS at Imperial	1 mm	$\sim 1 \times 10^8$/s	> 10 m/s	3.5 cm	7 G/cm

Table 4.1: A table summarising the parameters of some groups that have successfully operated an LVIS. The $1/e^2$ column refers to the trap laser beam size.

using the shim-fields, a simulation was performed in which the centre of the quadrupole field was slightly offset from the position of the extraction column. In the simulation the equations of motion were solved for atoms under the combined influence of the laser beams and magnetic fields, including the dark extraction column in one of the beams, following the methods in [100]. The trajectories of 100 atoms for two similar conditions are shown in Figure 4.5. Each atom begins with a velocity of 25 m/s at the edge of the molasses region with random direction and position. In part (a), perfect alignment of the LVIS is simulated. The centre of the quadrupole field and the laser beams overlap with the middle of the LVIS extraction column and all atoms captured in the MOT are eventually transferred into the LVIS beam. In the second simulation, shown in part (b), the centre of the quadrupole field is misaligned from the centre of the laser beams and extraction column by 700 μm in the x and z directions. The flux of atoms out of the LVIS is dramatically reduced. Indeed, only one of the 100 atoms in the simulation is directed out of the LVIS. The results of this simple model demonstrate that the small magnetic field and beam alignment adjustments needed regularly are an essential part of maintaining maximum performance from the LVIS.

4.2.8 Beam Divergence

The collimation of the atomic beam is important in determining the re-capture efficiency. A simple expression for the divergence of the beam is given by $\theta = d/z$ where d is the diameter of the extraction column and z is the distance from the point where atoms enter the extraction column to the mirror aperture itself. The distance z is approximately 25 mm giving a divergence of $\theta = 40$ mrad. After travelling ~ 30 cm to be re-captured in the second MOT, the beam profile would have expanded to a diameter of 2.4 cm, still within the cross-sectional area of the mirror-MOT beams, allowing the atoms to be recaptured.

Ref. [94] reported a significantly higher flux of atoms from the $2D^+$ MOT compared to an LVIS. It is interesting to note that the author of Reference [100] did not observe any increase in the LVIS flux by attempting to cancel the LVIS field gradient in one dimension.

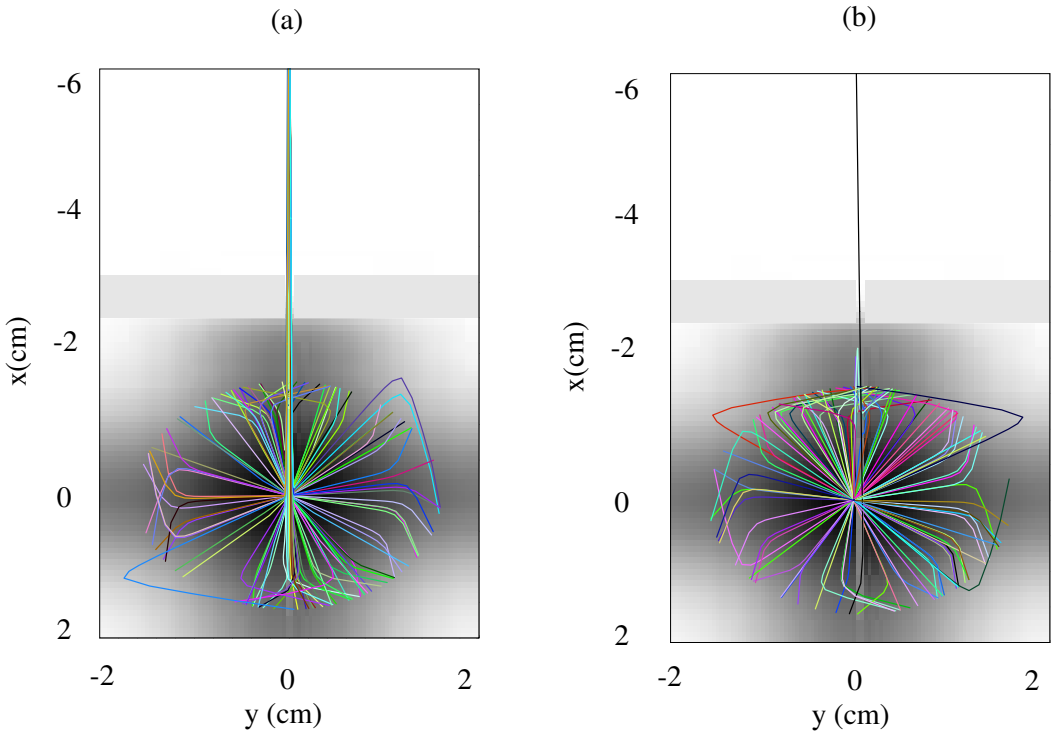

Figure 4.5: The trajectories of 100 atoms in the simulated LVIS. In (a) the quadrupole field center coincides exactly with the centre of the extraction column and all of the atoms captured in the MOT are coupled out through the hole. In (b) the centre of the quadrupole is offset from the centre of the extraction column by 700 μm. Only one of the 100 atoms in (b) is extracted from the LVIS in this case.

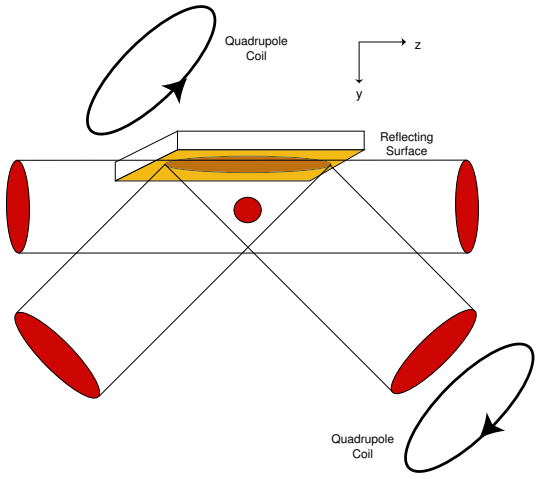

Figure 4.6: The orientation of a mirror-MOT. Two of the four beams are reflected from the surface. The anti-Helmholtz coils produce the usual quadrupole field, orientated at 45 ° to the plane of the surface.

4.3 The Mirror MOT

So far the principle of the LVIS has been introduced and details of the LVIS actually constructed in the laboratory have been given. As previously discussed, the purpose of implementing an LVIS was to load a mirror-MOT on the atom chip. In the following sections the mirror-MOT will be formally introduced. This is followed by results obtained from loading the mirror-MOT using the LVIS.

The mirror-MOT [85] design is particularly well suited to trapping atoms a few millimeters away from a reflective surface. This is a great advantage for loading laser cooled atoms into atom chip surface traps because the atom chip structure forms an integral part of the MOT geometry rather than an obstruction. The MOT employs four trapping beams, two of which are reflected from the mirror-surface. The quadrupole coils are orientated at 45 ° to the plane of the mirror surface.

The beams are circularly polarised as in standard MOT and the reflection off the surface maintains the necessary polarisation orientations due to the inversion of helicity on reflection.

4.3.1 The Mirror-MOT in Practise

A mirror-MOT is formed in the main-chamber using the gold coated surface of the videotape atom chip. The reflective area of the atom chip surface is 1 inch^2. The mirror-MOT beams had a diameter of 1 inch to roughly fill the area of the chip.

The quadrupole magnetic field was provided by two external coils in anti-helmholtz configuration. Each coil had 480 turns and a diameter of 10 cm and separation of 21 cm. Water cooling in the coil formers allowed up to 5A of current to be run through the coils for short periods. However, overheating could easily occur if run for prolonged periods and the coil for-

mers could reach temperatures in excess of 100 °C. Normally about 4.5 A were run through the coils creating an axial field gradient of 10 G/cm.

The detuning of the mirror-MOT trap light was normally set between 2Γ and 2.5 Γ, where Γ is the natural linewidth of the cooling transition. The detuning was chosen experimentally to achieve the largest MOT numbers.

Initially, the mirror-MOT was operated with a single horizontal beam which was retro-reflected. However, to minimise the effects of beam attenuation at high densities, two independent horizontal beams were subsequently used. Some abberation of the beams reflected off the atom-chip surface was visible due to roughness introduced by the videotape surface. However, these distortions did not seem to affect the operation of the mirror-MOT adversely.

4.3.2 Fluorescence Measurements

The time-dependence of the number of atoms in the mirror-MOT and can be determined by collecting the fluorescence signal with a photodiode or CCD camera. The power measured gives the number of incident photons from the MOT and knowing the collection efficiency and scattering rate the atom number can be obtained. The photon scattering rate for a two-level atom in laser beams of detuning δ is given by

$$R = \frac{\Gamma}{2} \frac{I_{tot}/I_{sat}}{1 + I_{tot}/I_{sat} + \frac{4\delta^2}{\Gamma^2}} \tag{4.5}$$

where I_{tot} is the total intensity sum of the trapping beams. For an optical transmission fraction of F and collection solid angle of $d\Omega$ and power P measured by the detector, the atom number N is given by

$$N = \frac{P}{Fd\Omega R} \frac{\lambda}{hc} \tag{4.6}$$

where $\frac{hc}{\lambda}$ is the energy of a photon.

In the measurements presented in the following section, the florescence was collected by a 2.54 cm diameter lens 20 cm from the centre of the MOT and cast onto a 1 cm^2 amplified photodiode.

4.3.3 Loading the Mirror-MOT from the LVIS

In initial experiments, the mirror-MOT was loaded from a rubidium getter source mounted on a flange in the main chamber approximately 20 cm away from the trapping region. The dispenser was heated at 7.5 A for 10 s to fill the mirror-MOT and then the vacuum was allowed to recover for 10 s before attempting any further experiments. The LVIS eventually replaced this loading method entirely.

The loading time and decay rate of the mirror-MOT from the LVIS are measured by monitoring the MOT fluorescence as a function of time on a photodiode. Figure 4.7 shows the florescence from the mirror-MOT during loading from the LVIS beam under non-optimal con-

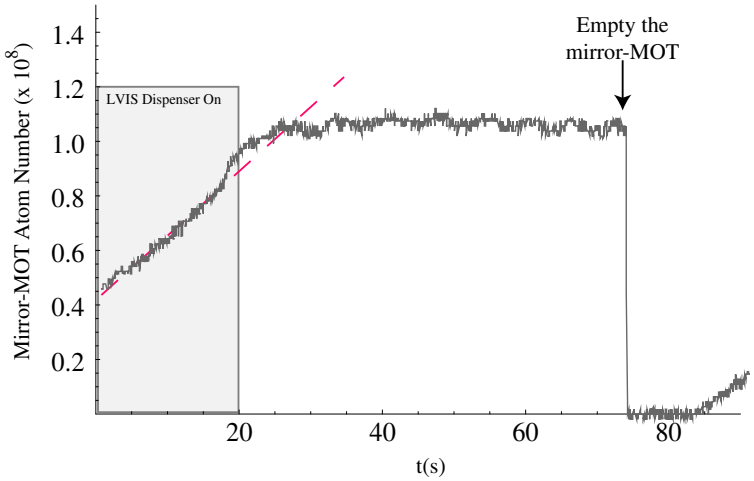

Figure 4.7: LVIS loaded mirror-MOT. The gradient of the fill curve provides an indication of the capture rate from the LVIS. The slope of the dashed line yields a minimum value of 4×10^6 atoms/s in this un-optimised example.

ditions. Loading begins with 5×10^7 atoms already in the mirror-MOT. The LVIS dispenser is then turned on at 7.5 A for 20 s at $t = 0$. The florescence from the mirror-MOT can be seen to increase with time in Figure 4.7 until 1×10^8 atoms have been loaded. The initial gradient of the fill curve indicates that $\sim 4 \times 10^6$ atoms/s are captured from the LVIS beam during this particular fill cycle. The flux of atoms delivered to the mirror-MOT by the LVIS beam varies during the operation of the LVIS dispenser. This can be seen as an increase in loading rate towards the end of the 20 s fill curve. The LVIS dispenser is switched off at the end of the 20 s but LVIS MOT is left on. The mirror-MOT reaches a steady state during this interval. At $t = 75$ s the mirror-MOT quadrupole field is turned off to empty the trap. When the LVIS is well-optimised nearly 10^8 atoms/s are recaptured by the mirror-MOT.

An image of the mirror-MOT florescence is shown in Figure 4.8. The image is captured by an infra-red security camera looking into one of the viewports used for a horizontal mirror-MOT beam. The structure of the atom chip can be clearly seen above the MOT. The reflective gold surface is partially visible because of the slightly oblique viewing angle. Some light scattered off the windows can be seen around the MOT. The 8 mm distance between two of the mounting screws on the atom chip is shown as a length scale comparison. The maximum number of atoms in the mirror-MOT was around 10^9, with 5×10^8 being available relatively straightforwardly. Certainly this is larger than any cloud that could easily be loaded into an atom chip magnetic trap and steps, described later, are taken to attempt to maximise the transfer. The large atom numbers is a direct result of implementing the LVIS.

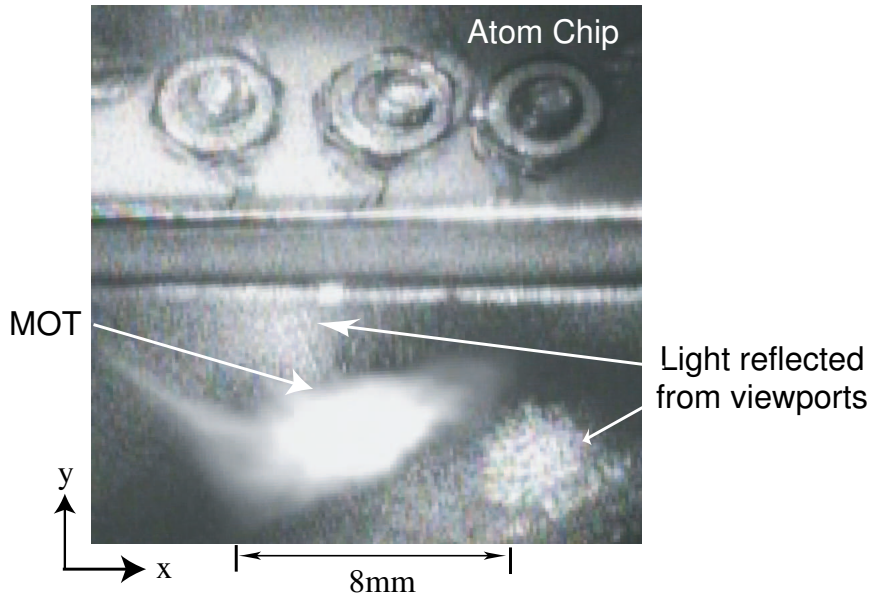

Figure 4.8: An image of the mirror-MOT captured with a security camera. The atom chip is visible in the top half of the image. Some laser scatter from the viewports is visible in the regions surrounding the MOT.

4.3.4 Mirror-MOT Lifetime

The lifetime of the mirror-MOT is an important indication of the vacuum in the main chamber. The decay of the mirror-MOT is shown in Figure 4.9. First the MOT is loaded by the LVIS for 20 s. At $t = 0$ the LVIS quadrupole coils are switched off to remove the flux of atoms, allowing the mirror-MOT to decay without any replenishment form the LVIS. The mirror-MOT florescence is monitored on a photodiode and the signal is plotted in Figure 4.9. The decay is well described by an exponential function with a time constant of 70 s. The lifetime is consistent with being limited by collisions with the background gas at a base pressure of 1×10^{-11} torr. The long lifetime of the MOT demonstrates that the low-conductance aperture between the LVIS and main-chamber successfully fulfills its purpose of maintaining UHV conditions in the main-chamber while simultaneously allowing high rubidium vapour pressure in the LVIS chamber.

4.4 The Mirror-MOT Temperature

In addition to its longevity, the temperature of the mirror-MOT is an important quantity. The temperature of a MOT can be obtained using the ballistic expansion method described below.

The idea of temperature in an ensemble of trapped atoms may seem ambiguous since the atoms are always isolated from interacting with their physical surroundings. This is at odds with the thermodynamic definition of temperature in which a collection of non-interacting particles

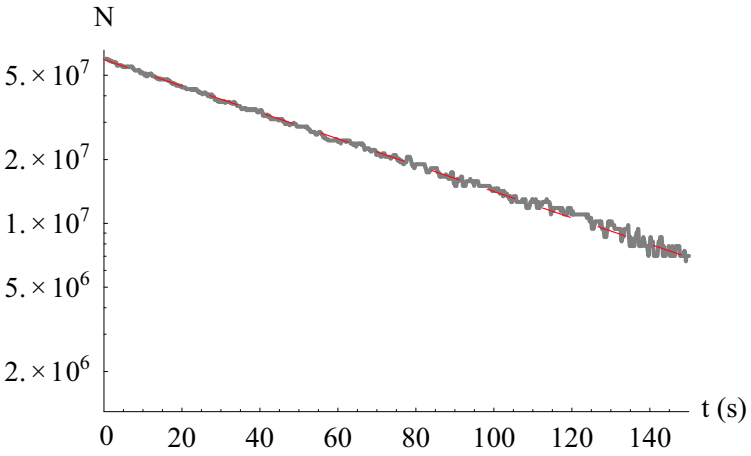

Figure 4.9: Decay curve of the mirror-MOT. The LVIS quadrupole field is turned off at time $t = 0$ to remove the flux of atoms. The solid line is the fluorescence signal from the mirror-MOT. The dashed line is an exponential fit with a time constant of 70 s.

is in thermal equilibrium with a heat bath. In this case the Maxwell-Boltzmann distribution links the particle velocities to an associated temperature T. In fact, the Maxwell-Boltzmann distribution can indeed be used to describe the atomic velocities in a MOT or magnetic trap [83] even in the complex environment of continuous scattering events in optical molasses.

The method of measuring temperature by ballistic expansion is a time-of-flight technique similar to that used to understand the temperature variation in optical molasses [101] that is also applicable to a thermal cloud released from a magnetic trap. At least two images taken at different expansion times are required to extract information about the initial velocity distribution of the trapped cloud at $t = 0$. The profile of the cloud after release is described by the convolution of the Gaussian spatial and velocity distribution functions which is also a Gaussian function with variance equal to the sum of the two initial variances. The half-width of the expanded cloud at time t is given by

$$\sigma_i^2(t) = \sigma_i^2(0) + \frac{k_B T}{m} t^2 \tag{4.7}$$

The temperature may be determined from the gradient of a plot of σ_i^2 vs t^2.

In order to determine the mirror-MOT temperature, the density profile was recorded taking absorption images with a CCD camera for various expansion times. To allow sufficient field of view of the expanding MOT the imaging system was set-up with a magnification of 0.35. An example of one one such expansion series is shown in Figure 4.10. A Gaussian profile was fitted to each image of the expanded cloud and the variance of the Gaussian is plotted against the square of the expansion time. The gradient of the linear fit gives a temperature of $480 \pm 30\,\mu$K. This temperature is somewhat higher than the Doppler temperature of $140\,\mu$K. MOT temperatures of several hundred micro-Kelvin are typical when no effort is made to

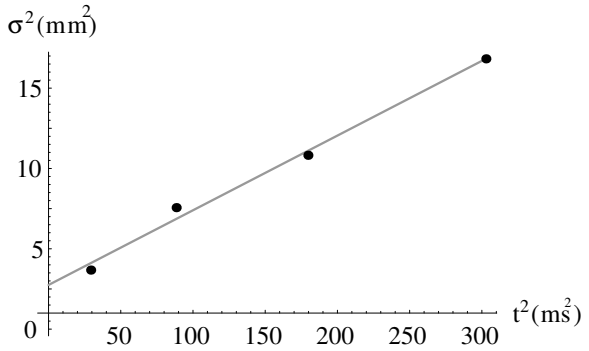

Figure 4.10: Ballistic expansion of the Mirror-MOT. The solid line is a linear fit giving a temperature of $480 \pm 30\,\mu$K.

take advantage of sub-Doppler cooling methods. However, a stage of sub-Doppler cooling is essential for efficient loading of the magnetic trap. This not only reduces the temperature but also transiently increases the peak density and thus phase-space density, greatly improving the initial conditions for progressing towards BEC.

4.4.1 Sub-Doppler Cooling

Several ways of implementing a sub-Doppler cooling stage were examined. A stage of pure optical molasses for several milli-seconds lowered the mirror-MOT temperature below $100\,\mu$K. However, this was at the considerable expense of atom number. A compressed-MOT formed by superimposing the quadrupole field of a current-carrying wire and bias field with the quadrupole field of the MOT quad coils to axially squeeze the cloud [36, 47] was also examined. This was reasonably helpful, however, by far the most successful method of cooling the MOT was to reduce the photon scattering rate *in situ* without changing the magnetic field gradients. Sub-Doppler cooling processes involve the several polarisation gradient cooling effects and are difficult to quantify precisely. However, the temperature achieved is broadly proportional to the factor $T \propto \frac{I}{\delta}$. Therefore, reducing the trap light intensity and/or detuning the trap light far from resonance assists in cooling the MOT.

A small reduction in mirror-MOT temperature was observed by reducing the trapping beam intensity to $\sim 10\%$ of its normal value. However, the most dramatic reductions in temperature were obtained by detuning the frequency of the trap beams as far from resonance as possible for some tens of milli-seconds. The maximum detuning was limited by the tuning range of the VCO providing the local oscillator signal for the laser lock described in Section 3.1.5. This resulted in a maximum detuning of $-50\,$MHz from resonance.

The length of time for which the laser was detuned was chosen to minimise the atom loss for a given reduction in temperature. The mirror-MOT temperature is plotted as a function of the cooling time in Figure 4.11 (a) to provide an example. The temperature decreases with longer cooling time with an apparent $1/t$ dependence. In contrast, the number of atoms remaining in

the mirror-MOT is plotted as a function of cooling time, shown in Figure 4.11 (b) and seems to follow a linear trend. Of course these trends cannot be rigorously determined from just three data points in this example but they broadly describe the situation. Although cooling times of 40 ms or longer would yield lowest temperatures, the corresponding loss in atom number is unacceptable. A suitable compromise was to choose cooling times between 10 and 20 ms to achieve temperatures routinely of 50 μK with a ($\sim 20\,\%$) loss in atom number. The temperature

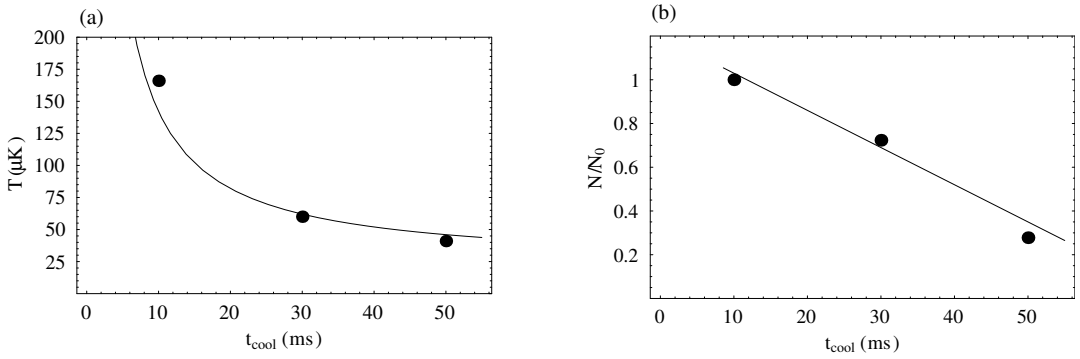

Figure 4.11: The mirror-MOT temperature and atom number as a function of cooling time t_{cool}. The solid line in (a) shows a t^{-1} dependence. The solid line in (b) is a linear guide to the eye.

of a mirror-MOT cooled for 30 ms as measured by ballistic expansion is shown in Figure 4.12 with a temperature of $55 \pm 3\,\mu$K.

In addition to the laser frequency and cooling time, the final mirror-MOT temperature was particulary sensitive to the manner in which the frequency was jumped. The best results were obtained by stepping the frequency in two stages, first to -35 MHz for 10 ms and then to -50 MHz for a further 5 ms. Presumably a smooth sweep of the detuning would improve the cooling process even further, although this is not possible with the laser lock presently employed. The cooling times and frequencies were established by experimental optimisation of the magnetic trap loading.

From the expansion data the initial size of the cooled MOT can be extrapolated to be approximately $400 \times 600\,\mu$m. The MOT undergoes rapid spatial compression during the sub-Doppler cooling stage, further increasing the phase-space density, although as seen above, atom loss sets in rather quickly. These parameters correspond to maximum peak densities of about $2 \times 10^{11}\,\mathrm{cm}^{-3}$ immediately after initiating the sub-Doppler cooling and phase-space densities as high as $\sim 3 \times 10^{-6}$, an increase in about two orders of magnitude compared to the un-cooled MOT. These are excellent starting conditions prior to loading a magnetic trap. The atom cloud must also be positioned appropriately for loading into a magnetic trap and this process is described in the next section.

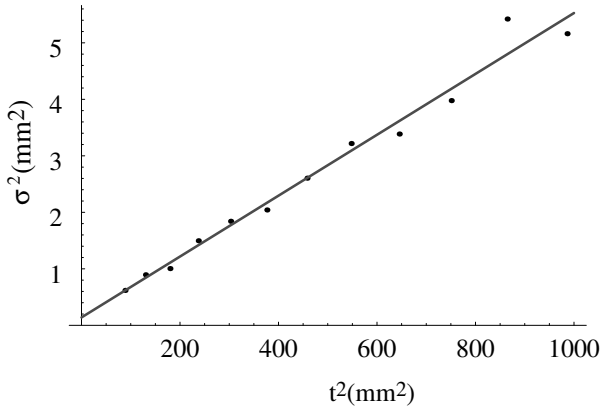

Figure 4.12: Ballistic expansion of the Mirror-MOT after sub-Doppler cooling for 30 ms. The fitted temperature is $55 \pm 3\,\mu$K.

4.5 Moving the Mirror-MOT Closer to the Surface

In order to load the atom chip magnetic trap the cloud must be less than 2 mm away from the surface of the atom chip. In normal operation, the mirror-MOT is formed 4-5 mm away from the surface. In order to avoid heating while transferring the atoms closer to the surface, the MOT was transferred closer to the chip before the cooling stage was implemented so that the magnetic trap could be loaded immediately afterwards. The transfer was achieved by ramping on an external bias field. This shifted the centre of the quadrupole field up, towards the chip surface. Due to the mounting angle of the mirror-MOT quadrupole field coils, the axis of maximum field gradient was at 45 ° to the horizontal. The applied bias field was set at an angle of 18.4 ° to the horizontal in order to shift the quadrupole centre directly upwards. The external field was formed by the B_{bias} coils and was ramped from zero to 5 G in 100 ms. Immediately after the mirror-MOT is ramped up to the surface, the sub-Doppler cooling stage is implemented in preparation for optical pumping and loading the magnetic trap. The large physical size of the mirror-MOT, as seen in Figure 4.8, means that during the ramping process a significant fraction of the mirror-MOT is likely to come into contact with the surface and become lost. It is likely that we lose up to half of the atom cloud in this manner. This reduction in atom number is an acceptable effect due to the large mirror-MOTs but difficult to quantify accurately. We have found that the best indication of the optimum loading conditions is is given by the number of atoms recaptured in the magnetic trap.

4.6 Summary

The state of affairs at this point in the experimental cycle is now briefly summarised. Rubidium 87 atoms emitted by the hot alkali dispenser have been captured by the high-power LVIS MOT and transferred by means of the LVIS output coupling beam into the mirror-MOT at the centre

of the UHV vacuum chamber. The MOT-cloud is then moved towards the surface of the chip where a stage of sub-Doppler cooling reduces the temperature to $\sim 50\,\mu$K. The next step is to load a magnetic trap and transfer the cloud of atoms into the videotape microtraps where further cooling by evaporation can be performed. The methods for re-capture, cooling in the magnetic trap and transfer to the videotape microtraps are the subject of the next chapter.

Chapter 5

Loading a Videotape Microtrap

In Chapter 4 the process of collecting and cooling samples of atoms in a mirror-MOT was described. In order to progress towards Bose-Einstein condensation it is necessary to load the atoms into a magnetic trap for evaporative cooling. The issue of matching the laser cooled cloud into a comparatively small videotape trap then arises. To assist in this, the cloud is first optically pumped and recaptured in a weakly confining magnetic guide formed by a macroscopic current-carrying wire and an external bias field, and trapped in the third dimension by the field of the end-wires. This trap is then compressed, allowing efficient evaporative cooling to commence. Once the cloud has been cooled it can then be gradually transferred into a videotape microtrap, ready for further experiments. A description of each of these stages forms the basis of this chapter. It begins with a brief description of the principle behind the magnetic trap formed by the macroscopic wire.

5.1 The Atom Chip Wire Trap

The principle of magnetic guiding and trapping has been previously introduced in the context of the microscopic traps formed by videotape. In this section the treatment is extended to consider the field produced by a macroscopic current-carrying wire, which provides a way of magnetically manipulating large atom clouds recaptured from the MOT.

A current-carrying wire produces a cylindrically symmetric magnetic field with a field strength that decays with distance from the wire. The magnetic field magnitude at a distance r from the axis of a wire carrying current I is given by

$$B(r) = \frac{\mu_0 I}{2\pi r} \tag{5.1}$$

which follows immediately from Ampère's law. Consider the case of a wire running along the z-direction with its axis centred on the point $x = y = 0$. If a uniform magnetic field B_{bias} is

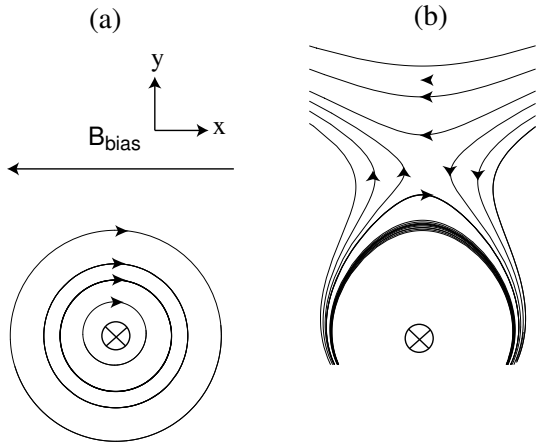

Figure 5.1: Magnetic field lines due to a current-carrying wire and bias field. In (a) the wire carries current into the page and a magnetic field B_{bias} is applied. The resulting field lines are shown in (b). A region of low field suitable for trapping atoms forms above the wire.

applied in the x-y plane, the field of the wire is exactly cancelled at a radial distance

$$r_0 = \frac{\mu_0 I}{2\pi B_{bias}} \tag{5.2}$$

This produces a region of low magnetic field running along $\hat{z}$ that can be used to confine weak-field seeking atoms. In the simple case when the field B_{bias} is applied along $-\hat{x}$, the field (now called B_x) is cancelled at a distance $y_0 = \frac{\mu_0 I}{2\pi B_x}$ and the height at which the minimum forms is therefore determined by the interplay between the magnitude of the wire current and the magnitude of the bias field. The principle of the wire guide is shown in Figure 5.1. In part (a) the magnetic field lines of the wire alone are illustrated and in (b), the field lines produced as a result of applying the uniform field B_{bias} in $-\hat{x}$ are shown and the resulting local field minimum above the wire is apparent. In Figure 5.2, cross-sections through the magnetic field minimum are shown, depicting the potential experienced by weak field seeking atoms. At the centre of the potential the magnetic field variation is linear with a field gradient B' given by

$$B' = \frac{2\pi B_x^2}{\mu_0 I} \tag{5.3}$$

Since the total field at the centre of the guide is zero, atoms in this region can be lost due to Majorana spin-flips. In order to stop the total field going to zero, a small magnetic field can be applied along z. This has the additional effect of rounding out the bottom of the trap which can then be approximated as harmonic at the centre. The equivalent harmonic frequency is determined from the field gradient as

$$f = \frac{1}{2\pi}\sqrt{\frac{\mu_\zeta}{m}\frac{\beta^2}{B_z}} \tag{5.4}$$

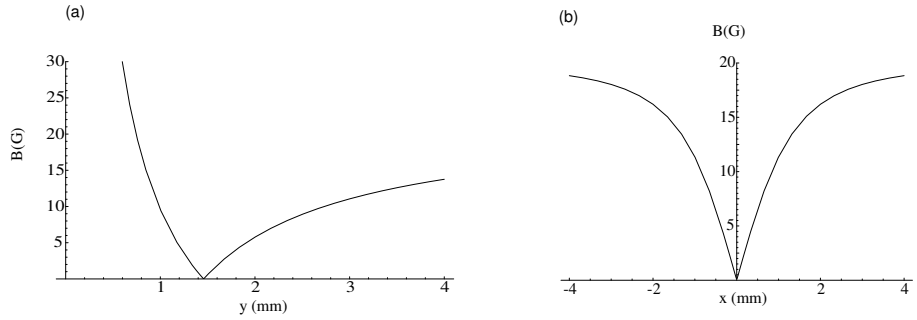

Figure 5.2: Magnetic field strengths of the wire + bias guide for $I = 15\,\mathrm{A}$ and $B_x = 20\,\mathrm{G}$. In (a) the cross-section of the field is plotted along the y-direction at $x = 0$. In (b) the field in the x-direction is plotted at the height $y = 1.45\,\mathrm{mm}$ where the minimum forms.

where $\beta = -\frac{\mu_0 I}{2\pi r^2}$ is the transverse magnetic field gradient at the centre of the guide. The depth of the confining potential is also modified by the axial field to become $\mu_\zeta(B_x - B_z)$. Full confinement in all three dimensions is achieved on the atom chip by combining the wire + bias potential with confinement in z provided by the end-wires. In order to recapture the atoms released from the mirror-MOT such a wire + bias potential is provided by the centre wire on the atom chip.

5.1.1 Temperature of a Thermal Cloud

One other theoretical aspect is mentioned here. A magnetically trapped cloud in thermal equilibrium in a harmonic potential of known frequency specifically allows the temperature to be inferred *in situ*. Consider an ensemble of particles trapped in a harmonic oscillator potential of angular frequency ω. The spatial distribution of N particles due to the Maxwell-Boltzmann distribution of velocities is also a Gaussian described by

$$f(x,y,z) = \frac{N}{(2\pi)^{3/2}\sigma_x\sigma_y\sigma_z} \exp\left[-\left(\frac{x^2}{2\sigma_x} + \frac{y^2}{2\sigma_y} + \frac{z^2}{2\sigma_z}\right)\right] \tag{5.5}$$

where the σ_i are the half-widths of the distribution in each dimension. By equating the thermal energy to the harmonic oscillator energy

$$\frac{1}{2}k_B T = \frac{1}{2}m\omega_i^2\sigma_i^2 \tag{5.6}$$

the spatial width of the trapped cloud is related to the temperature by

$$\sigma_i = \sqrt{\frac{k_B T}{m\omega_i^2}} \tag{5.7}$$

such that an image of the cloud in the trap can be used to obtain the temperature. The temperature may also be obtained by ballistic expansion, as was outlined in Section 4.4.

The next section returns to the experimental procedure for magnetic trapping, beginning with a stage of optical pumping.

5.2 Optical Pumping

In the interval between laser cooling and magnetic trapping, the atom cloud is spin-polarised in the $|F = 2, m_F = 2\rangle$ Zeeman sub-level, which can be magnetically trapped, by a stage of optical pumping to maximise the population that can be recaptured in the magnetic trap formed by the centre wire and end wires.

The optical pumping laser light is tuned to the $F = 2 \rightarrow F' = 2$ hyperfine transition and is circularly polarised to drive $\Delta m_F = +1$ transitions. This transition is chosen because once an atom has been fully transferred across to the $|2, 2\rangle$ state, it no longer interacts with the optical pumping beam, preventing unnecessary heating. The optical pumping beam must also be combined with a small amount of repump light because there is a decay channel into the $F = 1$ ground state in the optical pumping transition.

The optical pumping beam is derived from the reference laser and undergoes a double pass through an AOM operating at 123 MHz. The beam is blue-detuned by 20 MHz from the $2 \rightarrow 2$ resonance, experimentally selected to optimise the effectiveness of the optical pumping. The 1.7 mW beam is combined with ~ 1 mW of repump light using a beam-cube which is followed by a mechanical shutter. Mirrors then direct the combined beam towards the main-chamber where it is overlapped with the centre of one of the mirror-MOT horizontal beams using a polarising beam splitter cube. The MOT optics then direct the beam to the chamber window so that it enters the chamber along the same path as the horizontal mirror-MOT beam along the z-axis. The quarter-wave plate used to circularly polarise the horizontal MOT beam immediately before the chamber window also circularly polarises the optical pumping beam. The optical pumping beam has a diameter of 4 mm to ensure it illuminates the whole cloud and the z-component of the magnetic field of the end wires is used as the optical pumping quantisation axis.

The method of optical pumping along the z-axis was found to be superior to a previously attempted arrangement in which the beam entered the chamber orientated at $\sim 30^\circ$ to an applied bias field along x. It was found that by directing the beam along z the entire cloud could be pumped in a few hundred microseconds in contrast to a few milliseconds. This has the advantage that that cloud is unconfined for a shorter amount of time, minimising the amount of time for which it expands and falls and also reduces heating.

5.2.1 Optical Pumping Timing Sequence

Correct synchronisation of the laser light and magnetic fields is important for optimal optical pumping. To begin the sequence, the magnetic fields and laser light in the mirror-MOT must first be turned off and the quantisation field applied. The timing sequence for the optical pumping stage is shown in Figure 5.3. At the start of the sequence the mirror-MOT quadrupole

field is on as well as both pairs of bias coils which are used to move the MOT towards the atom chip surface as was described previously in Section 4.5. The quad coil and bias fields are then turned off and are replaced by a field from the end wires. This produces a magnetic field along the z-axis of $\sim 4\,\mathrm{G}$ in the region of the atomic cloud which acts as the quantisation field. Once the quantisation field has been turned on, the pulse of optical pumping light is produced by applying the rf signal to the AOM for $400\,\mu\mathrm{s}$. The mechanical shutter in the optical pumping beam is pre-triggered to ensure that it is open for the duration of the pulse. Once the optical pumping is complete the cloud is recaptured in a magnetic trap formed by turning on the centre wire and bias field as described in Section 5.3. The atom cloud is unconfined for a total time of 2 ms during optical pumping.

The optical pumping parameters were optimised by maximising the number of atoms recaptured in the magnetic trap. The temperature of the magnetic trap with and without the optical pumping stage was measured and no appreciable heating due to the optical pumping was observed. Typically, successful optical pumping allowed a factor of 2.5-3 more atoms to be captured in the magnetic trap.

5.3 Recapture in a Magnetic Trap

The optically pumped cloud is recaptured in a magnetic trap formed by the centre wire and the bias field. The depth, position and dimensions of the magnetic trap are critical for efficient recapture of the cloud. If the trap is not deep enough, hot atoms will escape over the edges and be lost. If the position of the trap does not closely match the position of the cloud, the atoms will find themselves on the side of the potential rather than at the minimum and begin to slosh, thereby heating the cloud. If the characteristic dimensions of the trap are significantly larger than the cloud size, the recaptured cloud will expand, resulting in a decreased density. If the trap is significantly smaller than the cloud size the cloud will be non-adiabatically compressed on recapture, resulting in heating. All of these processes can create to an undesirable loss in phase-space density at the point of recapture in the magnetic trap. Therefore, steps are taken to attempt to match dimensions of the recapture trap with those of the atom cloud and to match the position of the cloud with that of the trap, as described in this section. It is not possible to fulfill all these conditions fully, however, it has been pointed out in [55] that the relevant parameters scale in a forgiving manner such that efficient evaporative cooling is not significantly compromised.

The principal considerations determining the parameters of the recapture magnetic trap are that the trap frequencies should be low enough to efficiently recapture the cloud while simultaneously being deep enough to confine the cloud without loss. The trap depth in terms of temperature can be expressed as

$$\mu_B B = \eta k_B T \tag{5.8}$$

A value of $\eta \simeq 10$ is sufficient to ensure that the trap is deep enough to confine a cloud with

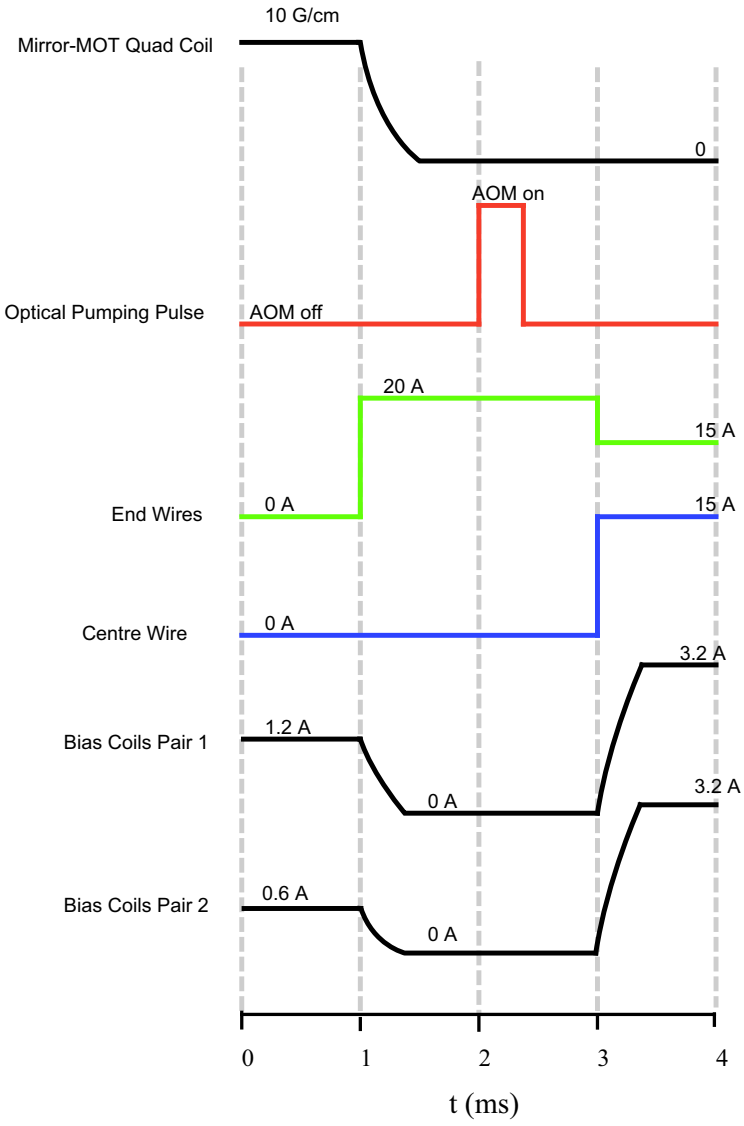

Figure 5.3: Timing sequence of the optical pumping stage. The MOT fields are switched off at the beginning, the optical pumping is performed and the atoms are recaptured in a purely magnetic trap.

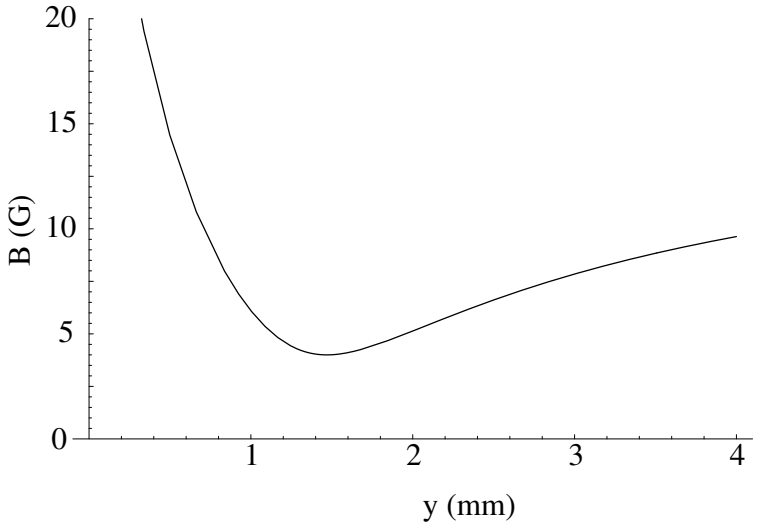

Figure 5.4: Potential of the recapture magnetic trap in the y-direction. The trap is chosen to provide weak axial confinement whilst simultaneously providing sufficient depth.

a temperature T. The atom cloud recaptured from the mirror-MOT is $\sim 50\,\mu$K so a trap with depth of order 10 G will adequately confine the cloud, thus determining the minimum magnitude of the applied bias field. We also wish to form a trap as far away from the surface as possible to facilitate transferring the MOT but are limited to a maximum safe current of 15 A in the centre wire which places some constraint on the trap height. Finally, the trap must not be too tight in the radial direction, meaning that a large net axial field B_z is desirable.

In practise, the cloud is normally recaptured in a magnetic trap with 15 A in the centre wire, a bias field of 14 G and 20 A in the end wires. The trap forms at a distance of approximately 1.5 mm from the surface of the chip. The contribution from the end wires to the axial field is about ~ 4 G at this height giving a calculated radial trap frequency of 41 Hz and radial trap depth of 10 G. The calculated radial potential of the re-capture trap is shown in Figure 5.4. If the cloud is loaded off centre, the sloshing motion in the trap can be used to measure the radial trapping frequency of the recapture trap. The position of the centre of the cloud is shown as a function of trapping time in Figure 5.5. Although only one clear oscillation of the cloud can be seen before many of the atoms are lost from the trap and the motion is damped, the period of the motion is measured to be 38 Hz, as shown by the damped cosine in the figure. This value of the radial frequency is in good agreement with the calculated trap parameters for the recapture magnetic trap. The fast damping time of $\tau = 20$ ms is due to the large amplitude oscillations of the cloud in a potential which has significant asymmetry beyond the central harmonic region. The collision rate is low and is not likely to contribute to the damping.

The end wires are turned on at their maximum safe current to provide as much trap depth as possible in the axial direction. If the centre of the cloud is poorly matched to the centre of the axial potential, the motion can be used to determine the frequency. The motion of the

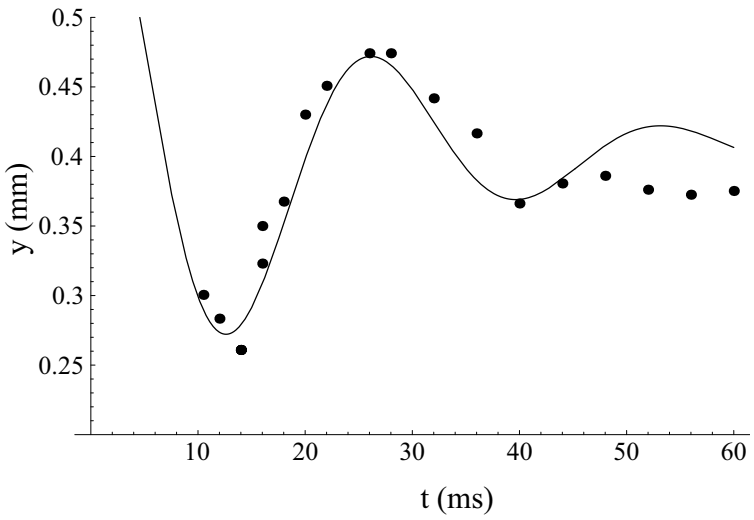

Figure 5.5: Radial centre-of-mass sloshing motion of the cloud recaptured in the magnetic trap. The solid line is a cosine with frequency 38 Hz. The damping is due to the large amplitude oscillations of the large cloud in the non-harmonic potential.

cloud in the axial direction over 150 ms is shown in Figure 5.6. Once again, the MOT position is poorly aligned with the magnetic trap and a sloshing motion is excited. The frequency of the oscillation is 13 Hz with no damping observable over the 150 ms duration because the trap is harmonic.

It is very important to minimise the sloshing motion for effective loading into the magnetic trap because the kinetic energy of the sloshing motion eventually causes heating of the cloud. The sloshing amplitude in the axial direction can be reduced from more than a millimeter to less than a few tens of microns by finely adjusting the position of the mirror-MOT with applied magnetic fields so that it coincides exactly with the position of the magnetic trap. Sloshing in the y-radial direction is minimised by making fine adjustment to the height to which the mirror-MOT is moved using the applied bias field before loading the magnetic trap. The x-direction is more difficult to judge because sloshing in this direction is not imaged but gross mismatches can be spotted by a reduced re-capture atom number. Once the sloshing has been minimised, and the cloud is reasonably well matched to the shape of the trap, no significant heating after transfer should occur.

An absorption image of an atom cloud recaptured in the magnetic trap is shown in Figure 5.7. It has an aspect ratio of ~ 2.5:1, in agreement with the calculated and measured trapping frequencies. Having successfully recaptured the optically pumped atom cloud in a purely magnetic potential, the next step is to increase the collision rate so that evaporative cooling of the cloud can begin. This is achieved by compressing the magnetic trap in the radial direction to increase the density and collision rate. To motivate the need for trap compression and increased collision rate the next section introduces evaporative cooling, before returning to describe the

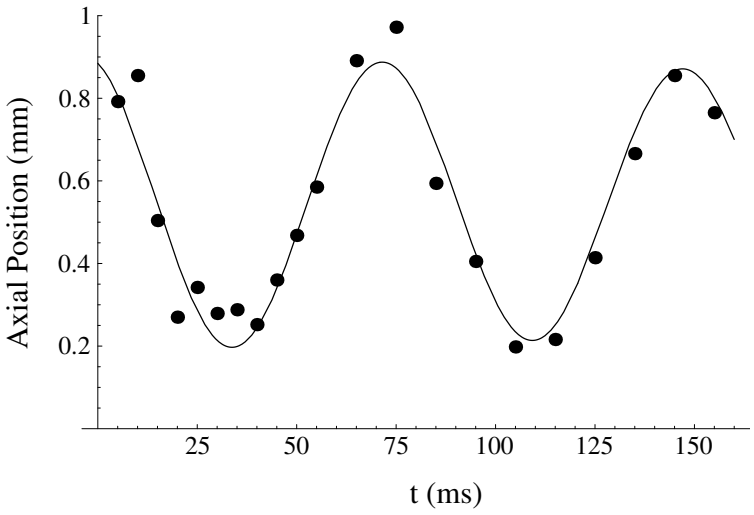

Figure 5.6: Axial sloshing after recapture in the magnetic trap. The solid line is a damped cosine of frequency 13 Hz and amplitude of 350 μm.

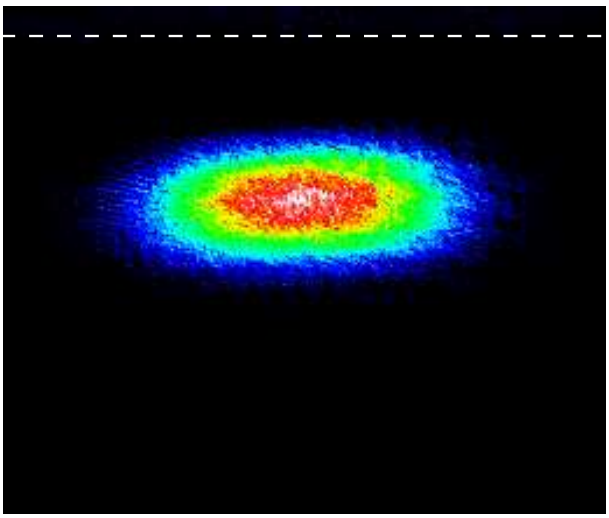

Figure 5.7: Absorption image of a cloud recaptured in the magnetic trap. The white dashed line denotes the surface of the atom chip. The imaged area is 4.6×4 mm.

compression and cooling in practise.

5.4 Evaporative Cooling Background

Evaporative cooling is a powerful tool for rapidly increasing the phase-space density of a trapped gas. The process works by selective removal of the atoms occupying the high-energy tail of the thermal distribution. After the truncation is performed, elastic collisions redistribute the remaining energy throughout the ensemble, causing the cloud to re-thermalise at a lower temperature. The process can be performed in a magnetic trap by driving internal spin-flip transitions into un-trapped states using a tuneable oscillating radio-frequency (rf) field. Atom chip microtraps are particulary well suited for efficient evaporative cooling because of the tight compression and high collision rates made available by using micro-structures.

5.4.1 Collision Rates and Evaporation Timescales

The aim before commencing evaporative cooling is to achieve high elastic collision rates so that evaporative cooling can be achieved in a short time. At low energies we can consider only the s-wave interaction potential and take the cross-section for collisions between two ground state atoms to be [102]

$$\sigma_{el} = \frac{8\pi a^2}{1 + k^2 a^2} \tag{5.9}$$

where $k = 2\pi/\lambda_{dB}$ and a is the scattering length. For temperatures below $30\,\mu$K then $\sigma_{el} \approx 8\pi a^2$ and a is measured to be $(98.98 \pm 0.04)a_0$ [103] in the ground state of ^{87}Rb where a_0 is the Bohr radius. The elastic collision rate is given by

$$\gamma_{el} = n\sigma_{el}\langle v_{rel}\rangle \tag{5.10}$$

where $\langle v_{rel}\rangle = \sqrt{\frac{6k_BT}{m}}$ is the average relative velocity between atoms and n is the number density. This rate can be increased by compression of the magnetic trap to allow efficient evaporative cooling.

Several models of evaporative cooling are available [104–106]. The process can increase phase space density rapidly if the self-sustaining runaway evaporation regime is reached. As the temperature of the cloud decreases, the rate of evaporation is maintained by ensuring a corresponding reduction in the trap depth such that η in Equation 5.8 remains roughly constant. The principal timescale governing evaporation is the rate at which elastic collisions redistribute the energy within the ensemble. The cloud re-thermalises after between roughly 2 and 4 elastic collisions. However, the rate at which evaporation is performed must also take into account the finite lifetime due to background collisions and three body losses at high densities governed by the time constant τ_{loss}. The various models agree that in order to sustain a constant or increasing collision rate (runaway evaporation) the initial condition $\gamma_{el}\tau_{loss} \gtrsim 150$ must be

fulfilled [106, 107]. Therefore long trap lifetimes and high compression are the ideal conditions for successful evaporation.

5.4.2 Forced RF Evaporative Cooling

Evporative cooling is achieved by selective removal of the hottest atoms. In a magnetic trap the Zeeman shift allows energy selection by appropriately tuning a radio-frequency field which drives transitions into un-trapped states. A linearly polarised rf field can be split into circular components capable of driving $\Delta m_F = \pm 1$ transitions,

$$h\nu_{rf} = g_F \mu_B |\mathbf{B}| \tag{5.11}$$

Atoms in state m_F with energy greater than ΔE will be removed from the trap according to

$$\Delta E = m_F h(\nu_{rf} - \nu_0) \tag{5.12}$$

where ν_0 is the frequency corresponding to the bottom of the trap $\nu_0 = \mu_B g_F B_0/h$.

Forced evaporative cooling is performed in the compressed magnetic trap and the compression is described in the following section.

5.5 Compression of the Magnetic Trap

Compression of the cloud is essential to reach the collision rates needed for effective evaporative cooling and several options are available to compress the trap. The aim is to keep the cloud sufficiently far away from the surface that the videotape does not play a significant role and yet increase the cloud density and thus collision rate by as much as possible. The field gradient of the wire-trap can be increased by lowering the current in the wire or increasing the applied bias field, as can be seen from Equation 5.3. Both of these processes cause the trap centre to move towards the surface. Furthermore, the field curvature at the bottom of the trap can be increased by reducing the net axial magnetic field in the trap. The change in the trap depth during compression must also be considered. Increasing the bias field *increases* the trap depth which is necessary due to the accompanying increase in temperature, however, decreasing the wire current compresses the trap but leaves the depth unchanged. Therefore reducing the wire current significantly is not a suitable strategy for compression.

Scaling laws for the temperature and density for a sudden and an adiabatic compression of a magnetic trap can be obtained for power-law potentials. Calculating the scaling of each parameter during the compression of a realistic potential such as the Ioffe wire microtrap is complicated by the fact that the shape of the potential changes from predominantly harmonic to predominantly linear during the compression. However, we can consider the effect of compression in each simplified case. An adiabatic compression that multiplies the potential by a factor of α scales the temperature by $\alpha^{2\delta/(2\delta+3)}$ [15, 106] where δ is the parameter describing

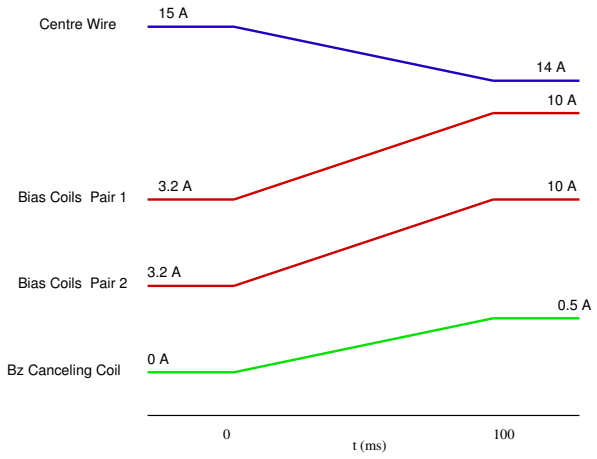

Figure 5.8: Timing sequence for the compression of the magnetic trap. The main compression is achieved by ramping up the current in the bias field coils. Adding a cancelling field along z also reduces the net axial field. Reduction of the centre-wire current is not always performed.

the shape of the trap. Adiabatic compression of a harmonic potential ($\delta = 3/2$) by α results in an increase of temperature by $\alpha^{1/2}$ and since $V(r) \propto \omega^2$ in each dimension, an adiabatic compression results in

$$T_f = T_i \frac{\omega_f}{\omega_i} \tag{5.13}$$

Compression of a wire-based microtrap can be approximated by a 2D compression of a linear potential ($\delta = 2$) [15] where the initial and final field gradients are proportional to the square of the proportional increase in bias field during compression (c.f. Equation 5.3). This results in a temperature increase of $\alpha^{8/7}$ for 2-dimensional adiabatic compression.

In practise, the magnetic trap is compressed by increasing the bias field B_{bias} from its initial magnitude of 14 G to 44 G over 100 ms, with the centre-wire current held constant at 15 A. In order to simultaneously increase the field curvature at the centre of the trap, a uniform field is ramped on in the z-direction to reduce the net axial field to ~ 500 mG. Reducing the centre wire current from 15 A to a value between 11 and 14 A also assisted in compressing the trap although this step was not absolutely necessary and was usually omitted. The timing sequence for compression is outlined in Figure 5.8 and the resulting calculated radial potential at the end of the sequence is displayed in Figure 5.9. The compression stage results in an elongated cloud approximately 190 μm from the surface of the chip. An example of an absorption image of the compressed-magnetic trap is shown in Figure 5.10 with a bias field of 44 G and 14 A in the centre wire. Several features of the compressed magnetic trap are worthy of note. The axial extent of the cloud in Figure 5.10 is greater than 7 mm. At these distances the atoms find themselves in fields in excess of 10 G, causing a detuning of more than 2Γ from the probe beam. This results in distortion of the cloud shape and errors when estimating the temperature of the cloud from *in situ* images. The detuning in the wings also has the effect of making the aspect

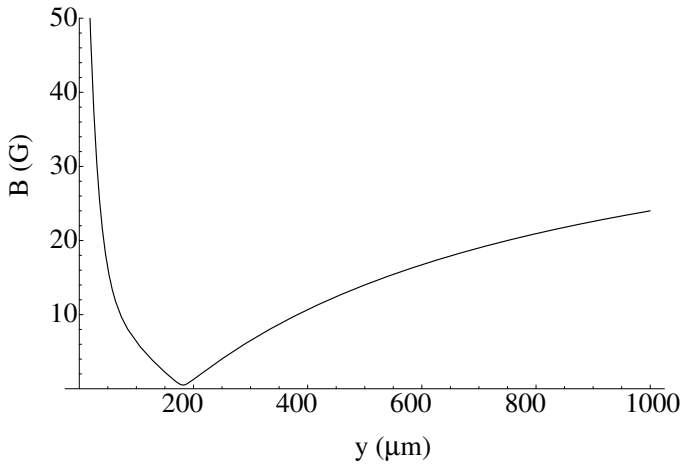

Figure 5.9: Magnetic potential of the compressed trap for $I = 15\,\mathrm{A}$ and $B_{bias} = 44\,\mathrm{G}$ and a net axial field of 500 mG. The contribution of the magnetic field of the videotape surface has also been included. The videotape provides a steep barrier at the surface.

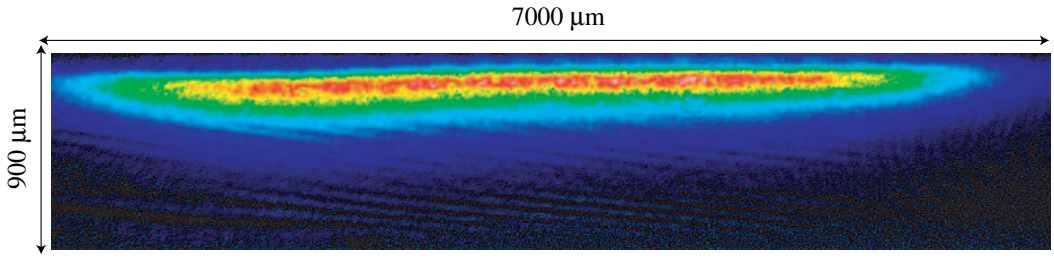

Figure 5.10: Absorption image of a compressed magnetic trap. The surface of the chip coincides with the top edge of the picture. The imaged area is $0.9 \times 7\,\mathrm{mm}$. The trap forms $\simeq 200\,\mu\mathrm{m}$ from the surface.

ratio in the image appear smaller than its true value.

The central region of the radial potential is calculated to be harmonic with frequency of $\sim 1100\,\mathrm{Hz}$. However, the compressed cloud principally samples the linear regions of the potential so a comparison of the radial profile to a radial harmonic potential is not helpful.

Ballistic expansion might seem to offer the best way to measure the true temperature of the compressed cloud. However, the high temperature and limited field of view mean that just a few milliseconds after release from the magnetic trap the long cloud dimension becomes much larger than the field of view of the imaging system, introducing a large error in the measured temperature. Using the method of ballistic expansion yields a temperature of $450\,^{250}_{100}\,\mu\mathrm{K}$ by measuring the radial width of the rapidly expanding cloud. The axial profile of the compressed cloud *in situ* gives a temperature of $350\,\mu\mathrm{K}$ although this is expected to systematically underestimate the temperature of the cloud as discussed above. An adiabatic compression of the radial direction assuming a harmonic trap would increase the temperature by a factor of 9.5, from $\sim 50\,\mu\mathrm{K}$ to $\sim 500\,\mu\mathrm{K}$, in agreement with the temperature estimated from ballistic expansion. It is quite possible that the compression is not completely adiabatic. Experimentally, the duration of the compression is optimised to minimise the atom loss during compression rather than temperature. However, the experimental uncertainties in the compressed trap temperature are not problematic due to the successful evaporative achieved in the compressed wire trap as discussed in Section 5.6.

Figure 5.11 shows the profile of a compressed cloud in the radial direction, integrated along the entire length of the cloud. The asymmetric profile follows the non-uniform shape of the trap potential. A small feature at $\sim 50\,\mu\mathrm{m}$ is due to atoms that have already become trapped by the videotape potential. There are two possible reasons why atoms may become accidentally trapped in the videotape. First, atoms from the MOT can be loaded directly into the videotape magnetic trap if they overlap at the time of loading. Second, hot atoms in the compressed wire trap can sample regions of the trap which are generated by the videotape. The possibility of this occurring can be seen from the contour plot of the compressed trap in Figure 5.12 which shows both the main minimum where the atoms are trapped and the additional minima forming videotape microtraps at about $40\,\mu\mathrm{m}$ from the surface. There are no significant problems posed by this additional trapping, the atoms soon become separated from the rest of the main cloud once evaporation commences.

The number of atoms in the compressed trap can be estimated by releasing the cloud from the trap. The rapid expansion of the cloud due to its high-temperature means that the cloud expands beyond the field of view of the imaging system. The total absorption of probe light indicates that there are at least 8×10^7 atoms in the compressed magnetic trap. This is likely to be an underestimate due to detuning from resonance for atoms close to the videotape surface and the near complete attenuation of the imaging beam due to the optical thickness of the atom sample. These conditions indicate that the elastic collision rate after compression is $60 \pm 30\,\mathrm{s}^{-1}$ for a temperature of $450\,\mu\mathrm{K}$ in a linear potential. With a magnetic trap lifetime of 15 s the ratio $\gamma_{el}\tau$ is therefore ~ 900 which is much greater than the required 150 to be within

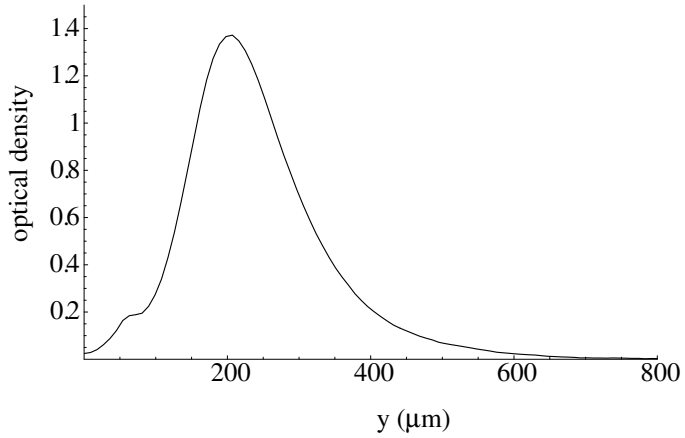

Figure 5.11: Profile of a compressed cloud in the radial direction integrated along the axial direction. The profile clearly deviates from a Gaussian distribution in the wings of the cloud as expected from the inhomogeneous shape of the confining potential in the compressed trap.

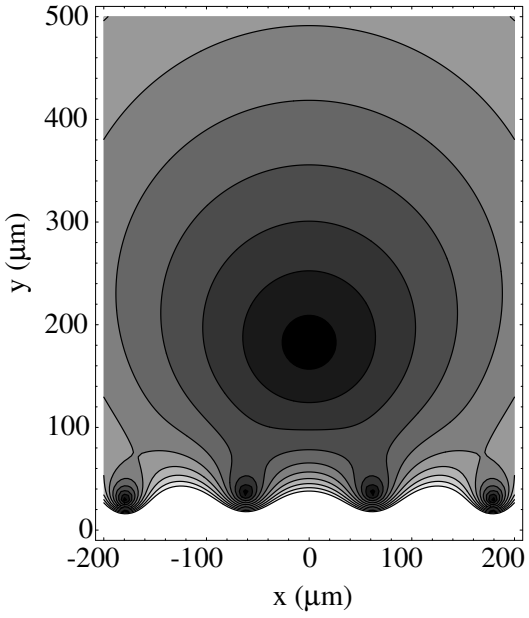

Figure 5.12: Radial contours of constant magnetic field in the compressed magnetic trap due to the centre wire and the magnetised videotape surface. $I = 15\,\mathrm{A}$, $B_{bias} = 44\,\mathrm{G}$. It can be seen that off axis there is additional contribution to the potential due to videotape microtraps at a height of approximately $40\,\mu\mathrm{m}$.

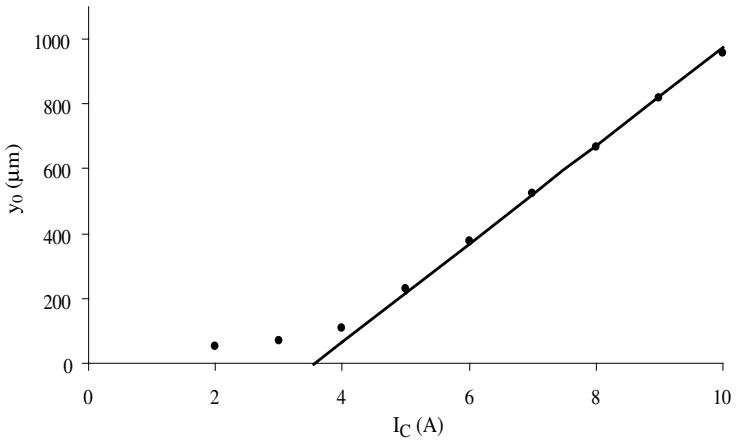

Figure 5.13: The height at which the magnetic trap forms (y_0) as a function of current in the centre wire. The applied bias field is 13 G. The solid line is a fit to the wire-trap height dependence (Equation 5.2). The deviation below 6 A is due to the presence of the videotape.

the regime for runaway evaporative cooling, given an optimum choice of truncation parameter η. The phase space density is of order 10^{-7} at this stage, indicating that some reduction in phase space density occurs during the recapture or compression. There may be further room for optimisation in these steps in future. Nonetheless, evaporative cooling can progress successfully and this is discussed in Section 5.6.

The depth of the compressed trap is limited by the axial-trap depth, which is approximately 25 G, somewhat shallower than the radial trap depth of 44 G. The truncation of the thermal energy distribution caused by the limited axial trap depth leads to some 1D evaporation in the compressed wire trap. This effect, although uncontrolled, does not lead to any detrimental effects. In fact, the resultant cooling is of some assistance. However, in order to control the evaporation process fully, the rf evaporation ramps begin immediately after compression is complete.

5.5.1 Determination of the Centre Wire Position

As a brief digression, the distance from the centre wire axis to the surface of the chip can be determined by measuring the height at which the trap is formed as a function of the current in the wire. In Figure 5.13 the measured trap height y_0 is plotted against the current in the centre wire I_c for an applied bias field of 13 G. A linear fit to Equation 5.2 for currents greater than 6 A is shown. The intercept of the linear fit indicates a wire-surface distance of 560 μm, consistent with the approximate total sum of the glass slide and glue between the centre wire and the surface. As the current in the wire is lowered below 5 A, corresponding to heights $\lesssim 150\,\mu$m from the videotape surface, the contribution of the field of the videotape becomes dominant and the trend deviates from linear. A study of the height of the *videotape* traps is

given in Section 6.0.1.

The centre wire position is not necessarily constant over long periods of time. For instance, the measured position can vary by as much as 80 μm between two measurements several months apart. This is to be expected since the centre wire is regularly heated by running current through the wire with variable duration and frequency. Measurements made with an identical wire in vacuum with similar heat sinking properties revealed that the temperature increased well above 100 °C after passing 7 A through it for a few tens of seconds. Notably, significant buckling of the wire was also observed. It is very likely that a similar situation applies to the centre wire used in this experiment. Tolerances greater than 80 μm in the wire position are expected because of the manner in which the wire resides in its channel in the stainless steel block on the atom chip. This does not present a problem because the position of the wire does not play a critical part in the experiment. The principal roles of the wire are to recapture and compress the atom cloud. The amount of compression achieved for evaporative cooling does not depend strongly on the wire position and therefore small fluctuations in the position do not play a critical role. It *is* however important to closely monitor the amplitude of centre-of-mass sloshing during the recapture of the laser cooled atoms and make appropriate adjustments to suppress this effect over long periods of time if any shift is observed.

5.6 Evaporative Cooling in the Compressed Magnetic Trap

After compression, an initial stage of evaporative cooling is performed to reduce the temperature of the cloud so that transfer into the videotape microtraps can begin. In order to drive the evaporation, an rf field is applied to the antenna on the atom chip. The parameters of the evaporation ramps are largely determined experimentally in order to maximise the remaining atom number at the end of the initial evaporation sequence. A number of rf time dependencies were tested including linear and exponential sweeps. The most successful evaporation was achieved with an exponential sweep in which the initial and final rf frequencies, duration and time constant could be experimentally optimised. The rf was swept over time, t, according to the function

$$\nu_{rf}(t) = (\nu_1 - \nu_2)\exp(-t/\tau) + \nu_2 \tag{5.14}$$

where ν_1 and ν_2 are the initial and final rf frequencies respectively and τ is the exponential time constant. The evaporation in the compressed wire trap was optimised with $\nu_1 = 30$ MHz, $\nu_2 = 3.9$ MHz and $\tau = 1$ s and swept for a duration of 6 s. The initial rf value of 30 MHz corresponds to a magnetic field of 43 G, which is approximately equal to the radial trap depth but larger than the axial trap depth. Therefore the rf field does not become resonant with the hottest atoms until after the sweep has commenced. However, this choice of initial frequency optimised the initial slope of the rf frequency sweep. Absorption images of evaporatively cooled atoms in the wire trap are shown in Figure 5.14. The rf was swept from 30 MHz to a variable final value before imaging the cloud in the trap. As expected, the dimensions of the cloud

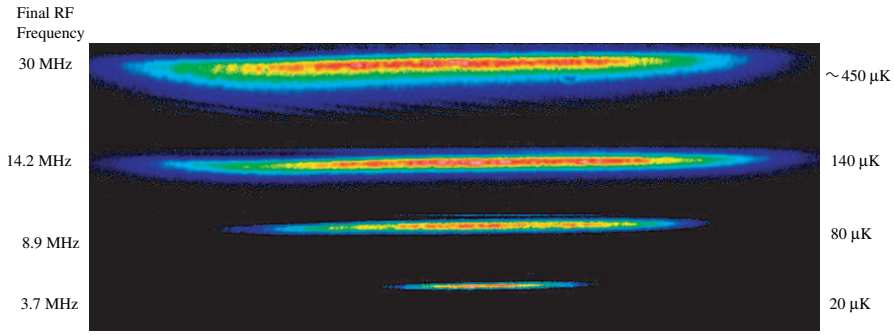

Figure 5.14: Absorption images of the compressed magnetic trap during evaporative cooling. The final rf frequency is shown on the left. The reduction of the axial and radial cloud widths indicates the reduction in temperature. Length of images 6.9 mm.

become noticeably smaller as the cloud is cooled. The temperatures in Figure 5.14 are derived from the axial length of the cloud with the assumption that the cloud has reached thermal equilibrium and is not significantly distorted by the trapping potential. The initial evaporation in the wire trap cools the cloud to $\sim 15 - 20\mu$K which is sufficient to begin the transfer into the videotape microtraps. The temperature is sufficiently low to load only one of the videotape microtraps.

5.7 Transfer into a Videotape Microtrap

The process of loading a videotape microtrap can begin once the cloud has been pre-cooled in the centre-wire magnetic trap. The principal aim is to finish with a single videotape microtrap loaded with the centre wire turned off completely. An intermediate regime in which atoms can be trapped simultaneously by the combined field of the centre wire and videotape is also available. However, for the purpose of performing experiments to probe the properties of the videotape traps it is most desirable to trap only using the field of the videotape.

The transfer into the videotape traps is achieved by ramping the bias field and centre-wire current appropriately, as well as tuning the axial bias field. The videotape traps are capable of generating very high trap frequencies and it is important not to transiently compress the cloud too much during transfer to avoid high-density losses and non-adiabatic heating.

The transfer is performed in two stages and is combined with simultaneous evaporative cooling to counteract the heating due to compression. In the first stage of transfer the centre wire current is ramped from 15 A to 5.5 A in 3 s. The bias field is simultaneously ramped from 44 G to 22 G and the B_z-cancelling coils are ramped off entirely to reduce the radial trap frequency. In the second stage of transfer, which lasts 1 s, the centre-wire is ramped off entirely and the bias field is ramped from 22 G to a final value depending on the required videotape trap height and gradient, usually between 500 mG and 5 G. Normally the end-wire current is kept constant at 15 A during transfer. After the completion of the second stage of transfer,

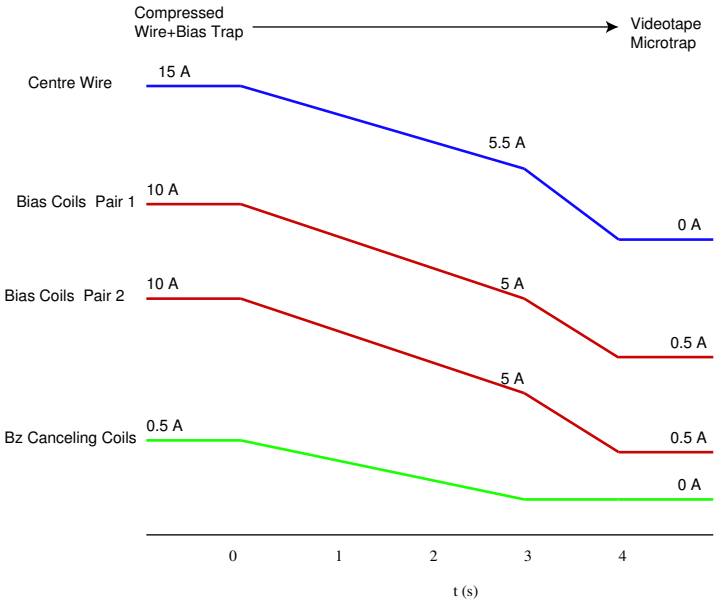

Figure 5.15: Timing sequence for transfer into a videotape microtrap. The ramps are designed and tested to avoid transient over-compression and to minimise trap loss.

the atoms are trapped due to the videotape, bias field and end-wire fields alone. The timing sequence for transfer into the videotape trap is shown in Figure 5.15. The rf signal is kept constant at 3.9 MHz during both transfer stages. This continues the process of evaporative cooling, counteracting any heating that occurs during transfer. Contours of constant magnetic field during the transfer process are shown in Figure 5.16. The radial trap frequency during the first stage of transfer reduces during the first 2 s of the transfer from to $\omega_r = 2\pi \times 1100$ Hz to $2\pi \times 500$ Hz as the cloud moves to a distance of 125 μm from the surface. For the remainder of the transfer the radial trap frequency approaches the final trap frequency of the videotape microtrap. For the case shown in Figure 5.16 the final bias field is 3 G and the trap forms at 60 μm from the surface with a radial trap frequency of $2\pi \times 1600$ Hz. The temperature of the cloud after transfer into the videotape microtrap is $\sim 10\,\mu$K, which indicates that the transfer process combined with the rf knife prevents any unwanted heating. During the transfer the temperature of the atoms is sufficiently low that they never sample regions of magnetic field outside the innermost closed contours in Figure 5.16, corresponding to an iso-surface of 0.5 G. This strongly indicates that the transfer does not load multiple videotape traps but rather only loads the trap that forms closest to the middle of the centre-wire potential. The only remaining uncertainty is whether or not the centre-wire lies exactly above one of the videotape traps at $x = 0$ as depicted in Figure 5.16 or whether there is a small offset δ between the centre wire and the videotape. The maximum possible offset between the wire and the periodic videotape magnetisation would be one half wavelength of $\delta = \pm 53\,\mu$m. In this special case, the cloud would be split exactly into two parts during the transfer, with the low temperature ensuring

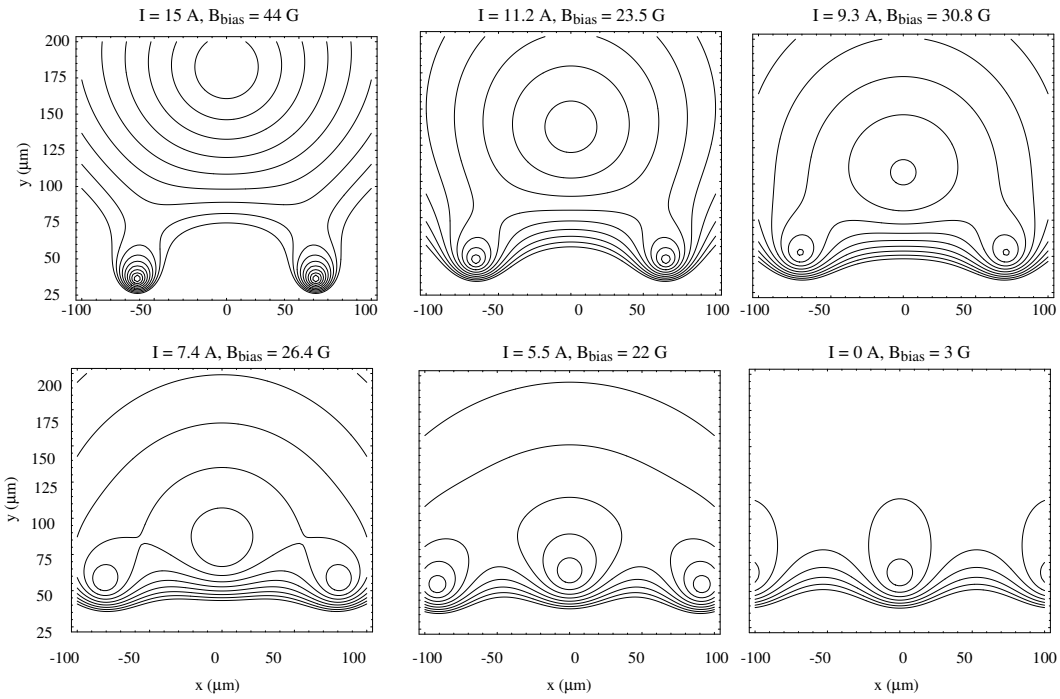

Figure 5.16: Transfer into a videotape microtrap following the experimental protocol. Contours of constant magnetic field are shown from $0.5 - 9.5\,\mathrm{G}$. The centre wire current and bias field are simultaneously reduced. At the end of the transfer the centre wire is turned off completely and the atoms are trapped by the videotape alone.

that the cloud was split into no more than two parts. It is most likely however that the wire is at an intermediate position δ. Depending on the temperature, most of the cloud would be preferentially loaded into one the microtraps over the other. While there is no evidence to suggest that more than one of the videotape microtraps is loaded during the transfer, the absorption image along the x-direction is not sensitive to the z-direction, where any splitting of the cloud would be observable. It is therefore not possible to claim with absolute certainty that one trap alone is loaded. It is possible however to conclude that the absolute maximum number of traps that could be potentially loaded is two. The possibility of deliberately using the videotape to split clouds presents interesting possibilities for novel interferometry schemes if a condensate could be split and recombined in this manner.

With the transfer to the videotape complete and the centre wire turned off the cloud is now trapped entirely in a videotape microtrap. The ultracold atom cloud can now be used to probe the properties of the videotape microtrap or cooled further to BEC as described in the next chapter.

Chapter 6

Microtrap Properties and BEC

Once the atom cloud has been transferred into a videotape microtrap, the ultracold atoms can be used to gain a further understanding of the magnetic field created by the videotape. In this section, the field at the surface of the videotape is determined experimentally and the range of radial trap frequencies is measured by means of a resonance experiment. A measurement of the slight horizontal tilt of the atom chip by observing the perturbation due to gravity is also presented. The second part of the chapter concerns Bose-Einstein condensation.

6.0.1 Measurement of the Surface Field

The form of the magnetic field due to the periodically magnetised videotape was presented in Section 2.2. It was shown that the field decays exponentially with distance from the surface and that the magnetic field strength at the surface depends on the magnetisation, magnetic film thickness and wavelength of magnetisation. The magnetically trapped ultracold atoms provide a unique method of determining the magnetic properties of the videotape. The exponential decay law for the magnetic field can be tested by measuring the height at which the magnetic trap forms as a function of the applied field B_{bias}. We recall a rearrangement of Equation 2.16 gives

$$y_{trap} = -\frac{\lambda}{2\pi} \ln\left(\frac{B_{bias}}{B_{sur}}\right) \tag{6.1}$$

where B_{sur} is the field at the surface. The field strength decays exponentially with a decay constant of $k = \frac{2\pi}{\lambda}$. On a plot of the trap height vs bias field, the height at which the trap forms y_{trap} should be linearly proportional to $\ln(B_{bias})$ with a slope of $-1/k$ and an intercept of B_{sur} on the x-axis. The trap height is obtained from an absorption image by measuring the distance between the cloud and its reflection. The trap height as a function of B_{bias} shown on log-linear axes is given in Figure 6.1. The error bars indicate the 4-μm uncertainly in the trap height and the 7 % calibration uncertainty in the bias field. The data follows a linear trend as expected and the intercept of the least squares fit to the data gives a surface field of 110 ± 10 G.

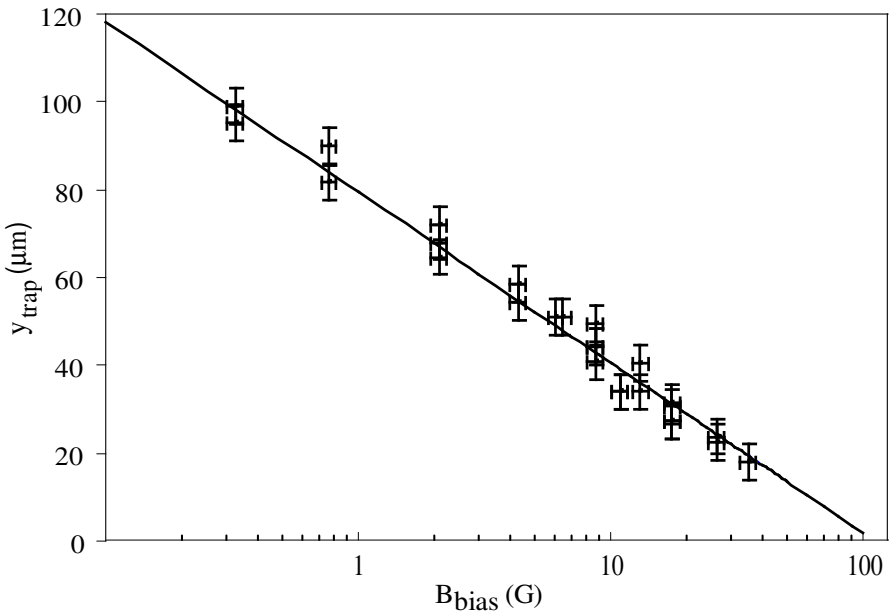

Figure 6.1: Dependence of the videotape trap height y_{trap} on the applied bias field. The intercept of the linear fit gives the field at the surface to be $110 \pm 10\,\mathrm{G}$.

The magnitude of the field at the surface was given in Section 2.2 as

$$B_{sur} = \frac{1}{2}\mu_0 M_1 (1 - e^{-kb}) \tag{6.2}$$

where M_1 is the magnetisation and b is the magnetic layer thickness. The videotape used in these experiments has a saturated magnetic remanence of $\mu_0 M_1 = 2.3\,\mathrm{kG}$ and a magnetic layer thickness of $3.5\,\mu\mathrm{m}$ [81]. For the recorded wavelength of $106\,\mu\mathrm{m}$ the maximum obtainable the surface is $215.5\,\mathrm{G}$. During the process of magnetising the videotape steps were taken to specifically avoid saturation effects. The current in the recording head was reduced when distortion in the playback signal was observed. The measured value of $110 \pm 10\,\mathrm{G}$, which is about half of field due to saturation, is consistent with the field expected as a result of recording the videotape in this manner.

6.0.2 Probing the Videotape Trap Frequencies

The videotape microtraps allow very high radial trapping frequencies to be obtained with the application of only a modest external bias field. For example a $30\,\mathrm{G}$ bias field and a net axial field of $1\,\mathrm{G}$ generates a trapping potential with a radial frequency of $\omega_r = 2\pi \times 22.7\,\mathrm{kHz}$. High radial trap frequencies make the permanent-magnet microtraps particulary promising for studies of low-dimensional quantum gases. It is helpful to be able to measure these frequencies for quantitative studies in these traps and to confirm the predictions of the theory for the videotape magnetisation. Ultracold atom clouds confined by the videotape can be used to make

studies of the radial trap frequencies by examining their response to external perturbations. It is not possible to measure the trap frequencies directly by exciting and observing radial centre-of-mass oscillations because the frequencies are too high and the oscillation amplitudes are usually much less than a micron. However, the radial trap frequencies can be indirectly observed by making a time-dependent modulation to the trap parameters and observing the heating that results when the modulation causes resonant excitation of the cloud in the trap. By adding a small modulation to the trap and scanning the frequency of modulation, the radial trap frequencies of a given magnetic trap can therefore be measured. This method of measuring trap frequencies is similar to that used by the optical lattice and dipole trap communities to measure the high trapping frequencies generated by optical potentials [108].

In order to probe the radial trap frequencies in practice, cold thermal clouds are prepared by evaporation and a modulation was then applied to the bias field B_{bias}. A function generator (Stanford DS345) was used to generate a modulation voltage of $\delta V = 30\,\mathrm{mV}$ which was added to the computer control voltage signal for one pair of bias field coils using a summing op-amp. The combined signal was then applied to the control input of the FET control circuit. The bias field is normally generated by the combined field of the two pairs of bias coils $B_{bias} = B_1\hat{\theta} + B_2\hat{\vartheta}$ where $\hat{\theta}$ and $\hat{\vartheta}$ are unit vectors at $\pm 45^\circ$ to the horizontal. The additional voltage corresponds to a magnetic field modulation in one pair of coils of $\delta B \simeq 100\,\mathrm{mG}$. For a drive frequency of f_{drive}, the time dependent bias field becomes

$$B_{bias} = B_1\hat{\theta} + (B_2 + \delta B\cos(2\pi f t))\hat{\vartheta} \tag{6.3}$$

The addition of this small modulation has the effect of periodically shaking the position of the centre of the trap in the x-y plane. For example, if the modulation is added to an applied bias field of 2 G the trap centre position is periodically shifted by $1\,\mu$m. This position shift is of the same order of magnitude as the oscillation amplitude of atoms in the trap at a temperature of $10\,\mu$K. When the frequency of modulation is far from resonance with the radial oscillation frequency this shaking of the trap has no observable effect. However, when the modulation frequency corresponds closely to the radial frequency, the cloud absorbs energy from the modulation. The absorbed energy is converted to thermal kinetic energy through collisions and the heating can be observed as an increase in the equilibrium size of the trapped atom cloud once sufficient re-thermalisation has taken place.

Evaporative cooling is used to prepare a thermal atom cloud at $10\,\mu$K. The cloud is compressed over 3 s into the radial potential whose trap frequency is to be determined. The modulation is then turned on for a duration of 5 s. After the modulation is complete the cloud is adiabatically decompressed into the original trap and imaged by absorption. The axial length of the cloud is used to determine the temperature of the cloud after decompression. Providing the compression and decompression are adiabatic the increase in final temperature measured in the trap is proportional to the energy absorbed during the modulation. This process is then repeated for different modulation frequencies to map out the response. Figure 6.2 shows the

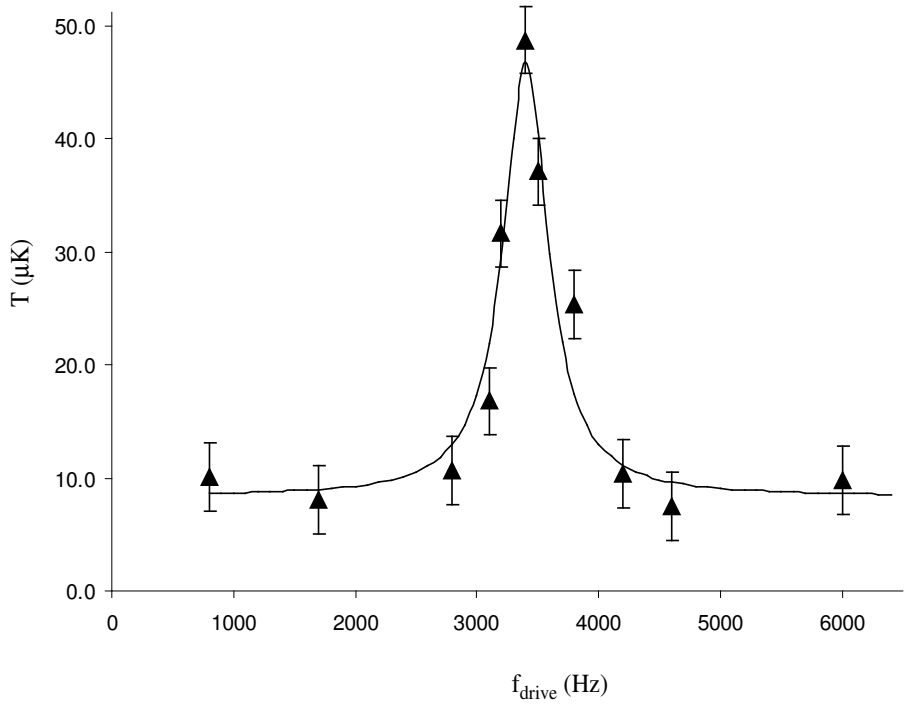

Figure 6.2: Response of the cloud temperature to a time-dependent modulation applied to the bias field. Data (▲): cloud temperature measured after the application of the modulation. Solid line: A Lorentzian function fitted to the data with a centre frequency of 3400 Hz.

results of one such measurement as the modulation frequency was varied in a trap with an applied bias field of 6.6 G and a net axial field of 2 G. As the modulation frequency is varied, a marked increase in the final temperature is observed close to 3.5 kHz. The solid line in Figure 6.2 is a Lorentizan profile giving a width of 445 ± 50 Hz FWHM and a centre frequency of 3.4 ± 0.2 kHz. The centre frequency of the excitation corresponds to the radial frequency f_r of the videotape microtrap. A second resonance can be observed at $2f_r$ if the frequency of the modulation is scanned far enough, although this was not usually performed. In order to examine the dependence of the radial trap frequency on the applied bias field, a number of measurements similar to the one presented in Figure 6.2 were performed for different bias fields. The range of bias fields corresponds to a range in heights from 80 to 20 μm from the videotape surface. The axial field varies no more than 5% over this range of heights. The centre frequency of the response to the modulation is plotted in Figure 6.3 as a function of the applied bias field. The radial frequency increases with the magnitude of the bias field and is well described by a linear trend up to a frequency of 6 kHz. The radial frequency of the videotape microtraps is expected to follow the relation

$$2\pi f_r = kB_{bias}\sqrt{\frac{\mu_\zeta}{mB_z}} \tag{6.4}$$

where μ_ζ is the atomic magnetic moment, m is the atomic mass and B_z is the net axial field.

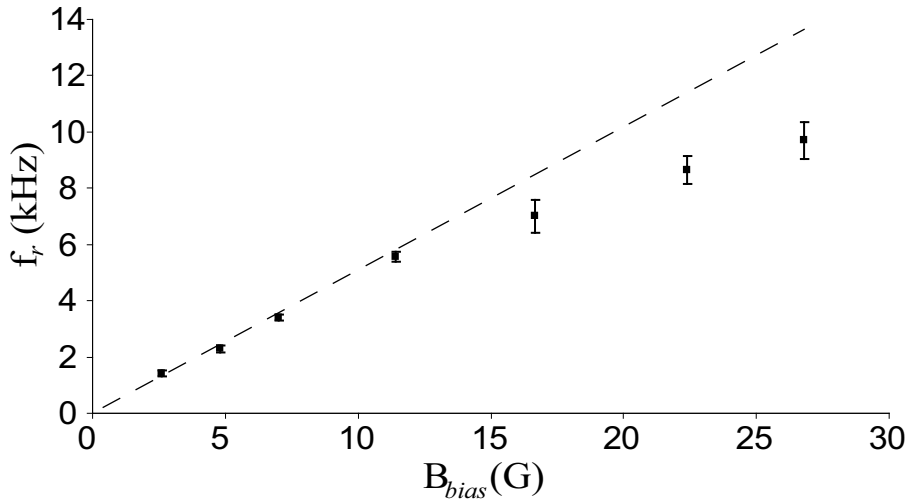

Figure 6.3: Data: Measured radial frequencies of the videotape microtraps plotted against the magnitude of the applied bias field for a net axial bias field of 2 G. The dashed line is the calculated radial trap frequency. The deviation at large bias fields is due to the anharmonic potential (see text).

The expected radial frequency according to Equation 6.4 is plotted in Figure 6.3 as a dashed line. There is good agreement of the data with theory until the data points begin to deviate from the dashed line at frequencies above 6 kHz. The deviation is accompanied by a dramatic increase in the width of the resonance. The first four points, which fall on the dashed line, all have a resonance width 540 ± 150 Hz FWHM. By contrast, the measurements that deviate from the theory have a mean resonance width of 2300 ± 500 Hz FWHM, nearly a factor of 4 times wider. The amplitude of the resonance is also reduced by a factor of 2. This deviation from theory and increase in the resonance width can be understood by considering the videotape potential experienced by the atoms and the cloud temperature. The videotape potentials are harmonic at the centre, but become linear beyond the central harmonic region. The amplitude of atomic oscillations, which is proportional to $T^{1/2}$, therefore determines whether the atoms sample the linear region of the potential. This is discussed further below.

The experimental sequence for obtaining a data point is to compress the trap, apply the modulation and then decompress the trap and measure the temperature. The quantity of importance is the temperature of the cloud after the initial compression, during the modulation, as this governs the motion in the trap under investigation. For an adiabatic compression from a harmonic trap of initial radial frequency ω_r^i to a final frequency of ω_r^f the temperature increase is proportional $(\frac{\omega_r^f}{\omega_r^i})^{2/3}$ if no change is made to the axial confinement, which is the case in these experiments. The initial radial trap frequency is well known, it corresponds to the first resonance measurement in the data set and has a frequency of $\omega_r^i = 2\pi \times 1.4 \pm 0.1$ kHz. This information is used to obtain the temperature in the trap after adiabatic compression. Let us take for example, compression by increasing the bias field to 25 G in 3 s. The temperature

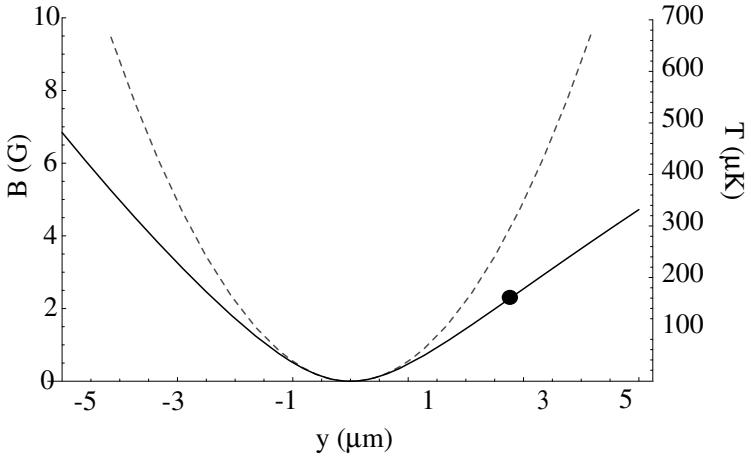

Figure 6.4: Deviation of the videotape microtrap transverse potential from that of a harmonic oscillator potential. Solid line: calculated potential of the videotape for a bias field of 25 G and an axial field of 2 G. Dashed line: pure harmonic oscillator potential with a oscillation frequency of $\omega = 2\pi \times 13.3\,\mathrm{kHz}$. In both cases the offset field of 2 G has been subtracted. The solid circle indicates the amplitude of oscillation of an atom at a temperature of $150\,\mu$K.

in this case is expected to increase by a factor of 5 during adiabatic compression. However, the temperatures measured after decompression are $\sim 30\,\mu$K indicating a temperature during modulation resonance of up to $150\,\mu$K. In the highly compressed videotape traps the harmonic region only extends to a radius of $\approx 1\,\mu$m. This is illustrated in Figure 6.4 which compares the calculated videotape potential for a bias field of 25 G with a harmonic oscillator potential with the equivalent curvature at the centre. Beyond a micron from the centre of the trap the potential begins to deviate significantly from harmonic and is effectively linear beyond $1.2\,\mu$m from the centre. A classical particle undergoing centre-of-mass oscillations in such a potential oscillates with a frequency lower than the equivalent harmonic oscillator frequency f_{HO}. The equivalent energy in micro-Kelvin for the Zeeman shift of a ground state ^{87}Rb atom undergoing a displacement in this potential is also shown on the right-hand axis of Figure 6.4. A mean temperature of $150\,\mu$K would result in atomic trajectories which sample significant linear region of the potential. Such behaviour would indicate why the measured resonance frequencies plotted in Figure 6.3 fall below the line predicted by theory; the atom clouds are hot enough to sample a significantly anharmonic potential and oscillate with a lower average frequency than f_{HO}. Each atom in the ensemble experiences a different local field curvature in its frame of reference. The modulation of the potential at a given frequency f_{drive} couples energy into the cloud less effectively, resulting in increased resonance widths and reduced amplitude.

Overall, the method of exciting radial resonances with a modulation of the trapping field is an effective method of determining the trap frequencies when the cloud dimensions prevent direct optical imaging of the motion. The measured frequencies show good agreement with the theoretical predictions in the limit that the cloud samples only the harmonic region of the trap.

Measurements of the harmonic trapping frequency up to higher values still could be performed in future using even colder clouds or condensates. Nonetheless, these radial trap frequencies are more than adequate for studies of low-dimensional quantum gases, allowing traps with aspect ratios much greater than 2000:1 to be generated with the videotape atom chip. Such tight, anisotropic confinement is unique among single magnetic traps, creating conditions only previously available in multiply loaded optical potentials.

6.1 Axial Confinement in the Videotape Microtraps

The discussion of the videotape microtraps has so far focussed on the properties of the videotape traps in the transverse radial direction, with little emphasis on the confinement provided in the axial direction. It has however been pointed out that the axial confinement is provided by the pair of end wires running beneath the surface of the atom chip. The ability to load ultracold atoms into the videotape potentials and cool them to sub-micro kelvin temperatures allows reasonably accurate measurements to be made of the axial trapping parameters as well as the radial parameters. These measurements include direct observation of the centre-of-mass oscillation frequency and the influence of gravity on the equilibrium trap position due to a slight tilt of the chip.

The force of gravity on confined atoms at micro-Kelvin temperatures can have a significant effect. The gravitational force experienced by a ^{87}Rb in the $|2,2\rangle$ state is equivalent to an applied magnetic field gradient of 15 G/cm. In the videotape microtraps the transverse field gradients are usually in excess of 1 kG/cm and the influence of gravity can be neglected. However, the in the axial direction the magnetic field gradients are much smaller and even a small additional field gradient can have a significant effect. This is the reason that Ioffe-Pritchard style magnetic traps, with weak axial confinement, are never orientated with the long axis parallel to the direction of gravity. The same applies to the videotape microtraps described here; however, the chip is not perfectly horizontal and a small influence due to gravity can be observed. This effect is described in the next section followed by an example of how the effect can be used to measure the oscillation frequency in the axial trap.

6.1.1 The Influence of Gravity on the Axial Field Gradient

The atom chip is mounted in vacuum on a stalk incorporating bellows and translation threads that allow adjustment of the position of the chip under vacuum. When the chip was installed it appeared nominally horizontal to the eye, but as we now know, it has a slight tilt with respect to the plane perpendicular to gravity. The sensitivity of the cold atoms to small forces allows this tilt to be measured.

Consider the case in which the atom chip is orientated with the plane of its surface at a small angle ϕ to the z-x plane. The z-axis of the coordinate system defines the long axis of the magnetic trap in the frame of the chip. The gravitational vector can be split into two

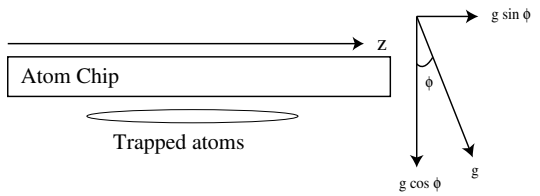

Figure 6.5: Schematic illustration of the effect of a slightly tilted atom chip. Viewed from the frame of reference of the chip there is a small component of gravity that acts along the z-axis.

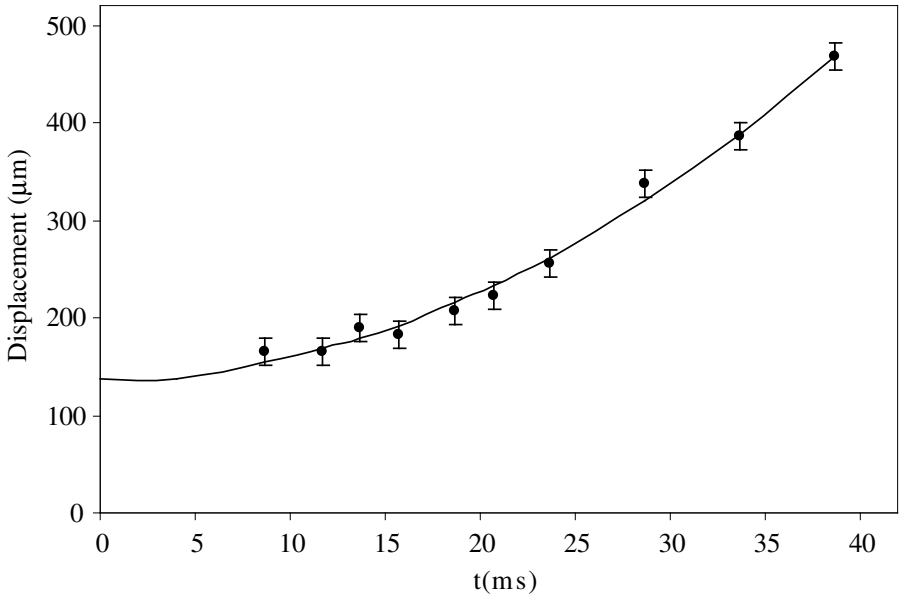

Figure 6.6: Position of the cloud during expansion in a waveguide. Data: the position of the centre of mass of a 1.6 μK thermal cloud from a Gaussian fit to the cloud. Solid line: fit to the data giving a uniform acceleration of 0.44 μm/ms^2.

components in the frame of the atom chip, one component along y and another component along z as illustrated in Figure 6.5. When the angle of the tilt is very small, which is the case here, $\sin(\phi) \approx \phi$. As the current in the end wires is changed, it is possible to detect a shift in the centre of the trapped cloud due to the small component of gravity along z. By measuring the magnitude of the displacement the angle ϕ can be inferred by considering the perturbation to the axial magnetic confinement. In another type of measurement the axial confinement is removed altogether and the cloud is allowed to expand along the radial waveguide formed by the videotape. As well as observing an expansion of the axial length of the cloud due to the thermal energy, the centre of mass of the cloud in the waveguide is also observed to shift. The acceleration of the cloud along the guide can be measured and used to estimate the tilt angle. The shift in the centre of mass of a 1.6 μK cloud expanding in a waveguide is shown in Figure 6.6. The data points are the centre position of the cloud as obtained from a Gaussian

fit to the axial profile. The solid line is a fit to the classical equation of motion for a particle starting at rest and accelerating at a rate of ϕg. The fit to the acceleration in Figure 6.6 gives $\phi = 0.045 \pm 0.003$ rad and an initial (arbitrary) position of $137.7 \pm 1.0\,\mu$m. A value of 45 mrad for the chip tilt agrees with the value determined by a measurement of the shift to the equilibrium trap position without removing the axial confinement altogether, which indicates that the atom cloud does not receive a 'kick' when the axial confinement is removed. There is probably also a small tilt in the x-direction too but it cannot be determined in this manner.

The tilt of the chip does not present any significant problems for confinement in the videotape microtraps. Perhaps a more sophisticated vacuum mounting system could be designed in future which allows the tilt to be adjusted more precisely. An extreme step taken for making precision measurements is to servo the compressed air system keeping the optical table afloat, as demonstrated in [109]. Such measures are not required for the experiments described here. In fact, the effect of the small force in the z-direction can be used to excite axial oscillations which allow the oscillation frequency to be measured as described in the next section.

6.1.2 The Axial Confining Potential

Measurements of centre-of-mass sloshing due to mismatch between the atom cloud and the magnetic trap position after loading from the MOT were presented in Section 5.3. A stationary atom cloud in equilibrium in a magnetic trap can only be excited to perform centre-of-mass oscillations by briefly applying a magnetic field *gradient* to transiently shift the equilibrium position. Equivalently, a small displacement due to the gravitational equilibrium position shift can be used to a excite centre-of-mass motion. The position of the cloud as a function of time is recorded by making an absorption image of the cloud as the propagation time is varied. An example of such a set of measurements is shown in Figure 6.7. For each data point a cloud of $1\,\mu$K was prepared by evaporative cooling in a videotape microtrap with a bias field of 0.5 G. A centre-of-mass oscillation with an amplitude of $100\,\mu$m was then excited by making a sudden change to the axial potential by switching end-wire current from 5 A to 15 A. The cloud then propagated in the trap for a time t and its position was recorded. The solid line in Figure 6.7 is a damped cosine. The axial oscillation frequency is $\omega_z = 2\pi \times 15.0 \pm 0.3$Hz. The cloud size is small compared to the amplitude of oscillation and the axial potential is harmonic over this region. The damping time of 150 ms is likely to be due to redistribution of the kinetic energy into thermal energy through collisions within the cloud. Roughness of the potential as discussed in Chapter 7 is not likely to play a very significant role in these measurements which were performed $95\,\mu$m from the surface.

With this knowledge of the axial trapping parameters a full empirically supported description of the videotape microtraps is available.

Having described the process of recapturing the laser cooled atoms, loading them into a permanent-magnetic microtrap, evaporative cooling and investigations of the trap properties, the final stage of cooling to BEC in a microtrap can be undertaken, and is presented in the

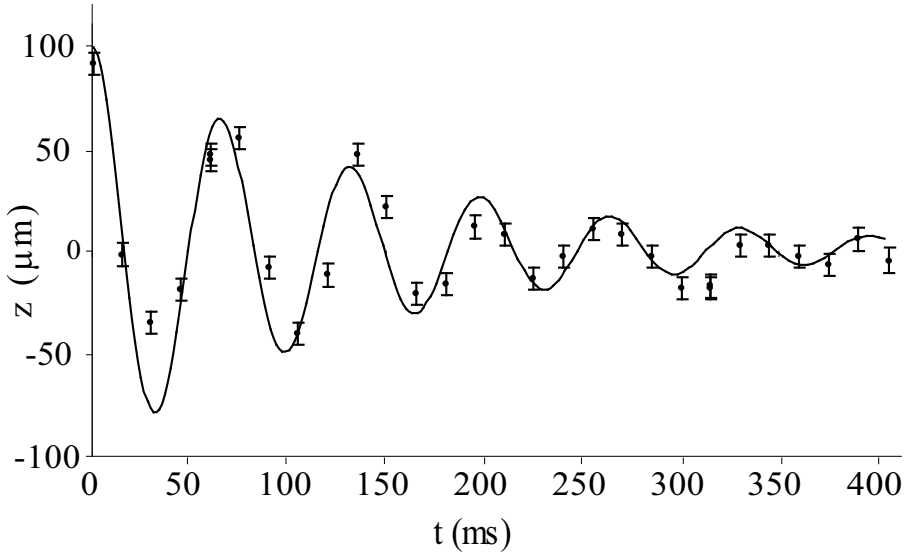

Figure 6.7: Oscillation of a 1 μK thermal cloud in the axial potential. The solid line is damped cosine with a frequency of $\omega = 2\pi \times 15$ Hz and a time constant of 150 ms.

next section.

6.2 Bose-Einstein Condensation

Thus far the steps taken to cool, trap and load atoms into a videotape microtrap have been discussed. In this section, production of BEC in a videotape microtrap will be presented.

6.2.1 Evaporation and Detection

A final stage of evaporation in the videotape microtrap is used to cool the cloud to BEC by sweeping the rf field exponentially from an initial value of 3.9 MHz to a final value usually between 800 kHz and 1.42 MHz, depending on the axial magnetic field. The rf field is swept according to the form of Equation 5.14 typically with a duration of 2 s and time constant τ of 400 ms, depending on the trap parameters. A balance must be struck between maintaining tight confinement close to the surface and avoiding the roughness of the potential, which increases closer to the surface. The absolute parameters of the evaporation are optimised experimentally. Absorption images taken *in situ* in the videotape microtrap during evaporative cooling are shown in Figure 6.8. It can be seen from these images that the cloud becomes significantly smaller as it cools, however, the radial dimension of the cloud in the image does not shrink, indicating that the imaging resolution limit has already been reached in the radial direction. The final image is almost spherical in shape despite the anisotropic trap shape. It is possible to observe the formation of BEC in this manner as central peak in the magnetic trap density profile, although the true shape is often masked by the limited resolution and the small spatial

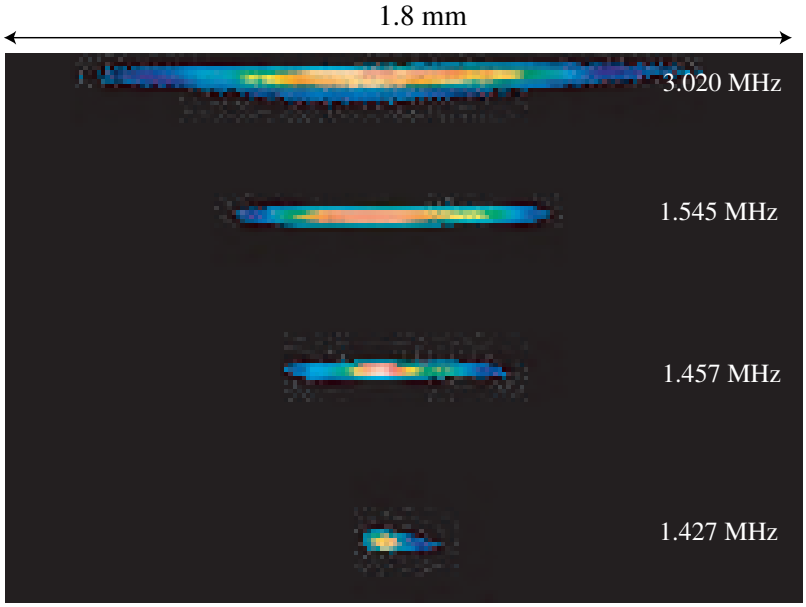

Figure 6.8: Absorption images taken in the videotape microtrap during evaporative cooling. The final rf frequency is shown on the right and the data was taken with an axial field of 2 G. The images are 1.8 mm wide.

extent of the condensate.

A much more satisfactory way to observe the formation of the condensate is to image the cloud after a time-of-flight expansion, a technique that is widely used in BEC experiments. This method allows clear resolution of the bimodal density distribution that is a key signature of BEC. The principal disadvantage of this method is that the videotape field cannot be turned off in the same way a coil or wire can, and effects due to this must be considered. If the field is not switched off carefully, distortions of the cloud can occur and acceleration due to the surface field gradients can also be significant. Examples of data obtained using these methods are described below.

6.2.2 Free Expansion of the Condensate

The trap is switched off by turning off the end wires, bias field and axial cancellation field. The fields are turned off simultaneously using the control software but in reality it takes between 2 and 3 ms for all the fields to switch off completely. In the case of sudden release, the atom cloud would be exposed to the magnetic field gradient of the videotape, which, at a height of 90 μm has a value of 300 G/cm or equivalently 20 g. The atom cloud therefore would be expected to undergo rapid acceleration away from the surface. In reality, the cloud is observed to become re-trapped between 100 and 200 microns from the surface. This in itself is not surprising since it only takes a stray magnetic field of 7 mG to trap a 500 nK cloud in the permanent field of the videotape, which of course cannot be switched off as is the case in wire-based traps. Attempts

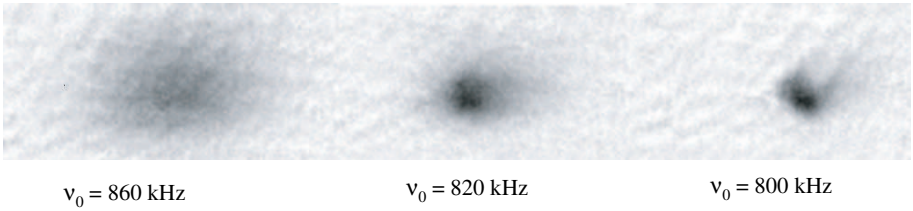

Figure 6.9: Free expansion of a thermal cloud and partial condensates as the temperature is lowered by evaporation. The emergence of the dense central component corresponds to the condensate.

were made to cancel stray fields but it was not possible to eliminate the re-trapping effect. In order to allow free expansion of the cloud between 100 and 300 mA was run through the centre wire during the release of the cloud. The axis of the centre wire is $\sim 600\,\mu$m from the cloud at the point of release so currents of a few hundred mA produce a magnetic field of $\sim$ 300-900 mG in the vicinity of the atoms. The magnetic field *gradient* due to the centre wire is negligible at these distances in comparison with the videotape field gradient. The process of turning on the centre wire to release the cloud pushes the cloud away from the surface, accelerating it further for higher currents. For comparison, a centre-wire current of 200 mA produces an acceleration equivalent to that due to gravity. In any case, the clouds are released in the same way each time allowing sets of data to be obtained in a consistent manner. Figure 6.9 shows the density distribution for three different final temperatures obtained by stopping the rf evaporative cooling ramp at three different final frequencies. The central dense component corresponds to the condensed part of the cloud.

6.3 Condensate Properties

Absorption images of the cloud taken during ballistic expansion can be compared with established theories of ideal gas condensates to obtain some of the relevant properties. The analysis and discussion in this section is performed assuming the Thomas-Fermi approximation. The Thomas-Fermi model is very well established as an accurate description of the behaviour of Bose-Einstein condensates under appropriate conditions. The justification for using this model in the particular experimental conditions under consideration here is discussed further in Section 6.3.3. First, the method used to extract information from the absorption images is described.

6.3.1 Data Processing

The three dimensional density distributions of thermal clouds and pure condensates confined in harmonic oscillator potentials have been previously discussed in Chapter 2. The shape of these distributions is preserved during ballistic expansion and is scaled accordingly in each dimension by the appropriate scaling factors for thermal clouds and pure condensates. It is also

necessary to consider the intermediate case in which both a condensed and thermal component are present. The simplest case is to treat the two components as independent from each other and non-interacting. Although there is not an exact theoretical description in this regime, this 'bimodal' treatment has described previous experimental data very well indeed [55] and has proved successful in describing partially condensed clouds. We recall that the Gaussian distribution used to describe thermal clouds is

$$n_{TH}(x,y,z) = \frac{N}{(2\pi)^{3/2}} \exp\left(-\left(\frac{x^2}{2\sigma_x^2} + \frac{y^2}{2\sigma_y^2} + \frac{z^2}{2\sigma_z^2}\right)\right) \tag{6.5}$$

and the density distribution of a condensate in the Thomas-Fermi regime is given by

$$n_{TF}(x,y,z) = \frac{15N}{8\pi R_x R_y R_z} \max\left[1 - \frac{x^2}{R_x^2} - \frac{y^2}{R_y^2} - \frac{z^2}{R_z^2}, 0\right] \tag{6.6}$$

where R_x, R_y and R_z are the Thomas Fermi radii of the condensate in each dimension and the subscripts TH and TF denote thermal and Thomas-Fermi profiles respectively. In experiments, the density profile recorded in an absorption image corresponds to integration along the x' direction yielding the 2D column density along x' where the prime denotes use of the imaging coordinate system. The resulting Gaussian and Thomas-Fermi column density distributions are then given by

$$n2D_{TH}(y',z') = \frac{N}{2\pi\sigma_{y'}\sigma_{z'}} \exp\left(-\left(\frac{y'^2}{2\sigma_{y'}^2} + \frac{z'^2}{2\sigma_{z'}^2}\right)\right) \tag{6.7}$$

$$n2D_{TF}(y',z') = \frac{5N}{2\pi R_{y'} R_{z'}} \max\left[1 - \frac{y'^2}{R_{y'}^2} - \frac{z'^2}{R_{z'}^2}, 0\right]^{3/2} \tag{6.8}$$

where integration has been performed along the x'-direction and the primes denote quantities in the imaging coordinate system. The transform into the image coordinate system due to the probe beam angle θ is given by

$$z_l' = \sqrt{z_l^2 \cos^2\theta + x_l^2 \sin^2\theta} \qquad y_l' = y_l \tag{6.9}$$

where the z_l etc. refer to the Gaussian widths or Thomas-Fermi radii.

In order to describe a partially condensed cloud, the total column density profile is given by the sum of the thermal and condensate components weighted by the condensate fraction f_c such that $n2D_{tot} = (1-f_c)n2D_{TH} + f_c n2D_{TF}$. By fitting this type of profile to the experimentally obtained absorption images the properties of the thermal cloud and condensate are obtained. It then remains to account for the ballistic expansion and extrapolate back to the static properties in the magnetic trap before release by using the appropriate scaling factors. For the axial dimension we recall that these are $\lambda_{z,T}(t) = \sqrt{1+(\omega_z t)^2}$ for the thermal cloud and $\lambda_{z,TF}(t) =$

$1 + \epsilon^2 \left(\omega_r t \arctan \omega_r t - \ln \sqrt{1 + (\omega_r t)^2} \right)$ for the condensate. In this manner, the temperature of the thermal component and condensate dimensions may be determined with knowledge of the initial trap frequencies.

In order to perform the fits to experimental data, the absorption image is normalised to the probe beam profile and the natural log is taken, thus obtaining the 2D optical density profile. Cross-sectional profiles through the centre of the cloud are taken and divided by the optical absorption cross-section to obtain the column density profile along the y' and z' axes since $n_{2D} = (1/\sigma_L)OD(y', z')$. The fit to the profiles is performed 'by eye' with the thermal cloud widths, condensate widths, condensate fraction and total atom number as free parameters, attempting to closely match the experimental profiles in both the y' and z' directions by minimising the residual difference. The transformation from the imaging coordinates y' and z' into the trap coordinates y and z is then performed to obtain the parameters in the frame of the trap.

6.3.2 Comparison with Theory

A set of free expansion data analysed in the manner described above is shown in Figure 6.10. A discussion of the behaviour is this set of data and the comparison between extracted quantities and those expected from theory follows below. However, first the experimental conditions under which this data set was taken are briefly described.

In order to obtain the data shown in Figure 6.10 the cloud was cooled by rf evaporation to sequentially lower temperatures determined by the end frequency of the evaporation ramp. The evaporation was performed in a trap $91 \pm 3.5\,\mu$m from the surface. The frequency at which all atoms are lost from the trap gives a measure of the net axial field B_z which in this case is 1.15 G. The radial trap frequency is determined from the bias field B_x and net axial field to be 335 Hz and the axial trap frequency, obtained by sloshing, is 15.0 Hz. The radial frequency is known to an accuracy of about 60 Hz mainly due to the measurement uncertainty on the bias field that forms the trap. The cloud is released by turning off the end wires and bias field and providing a small push with the centre wire at 300 mA during the release, and is allowed to expand for 8.7 ms before taking an absorption image.

The series of plots in Figure 6.10 correspond to cooling the cloud through the critical temperature for BEC. The points are data and the solid lines are bimodal distributions fitted in the way described in Section 6.3.1. With each plot in Figure 6.10 are given the final rf frequency as well as the temperature obtained from the axial width of the thermal component, the total number of atoms and the fitted condensate fraction. The axial direction is used to determine the temperature because the radial direction is potentially vulnerable to any systematic deformation during the release process from the videotape trap.

In Figure 6.10(a) the cloud is completely thermal and well described by a Gaussian profile. In Figure 6.10(b) the critical temperature is reached and a small peak at the centre begins to form. This is followed by the marked emergence of bimodal distribution composed of the thermal wings and a central condensed component as the cloud is cooled further. The peak

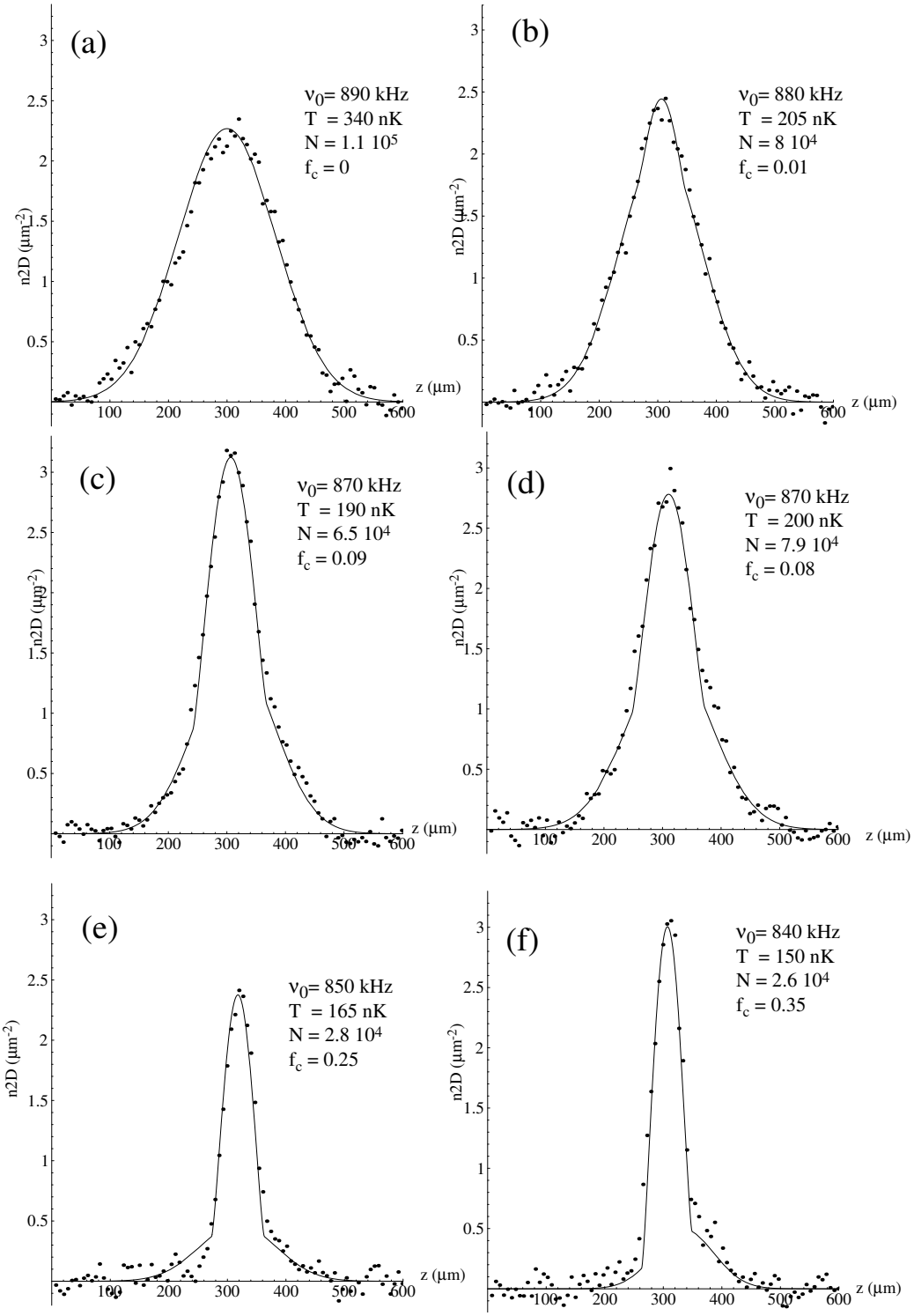

Figure 6.10: Axial profiles through the cloud after 8.7 ms time of flight as the final rf frequency is lowered. The solid lines are bimodal density distributions fitted to the data as described in the text. (a) corresponds to a thermal cloud and in (f) the condensate component dominates.

Condensate number	N_0	9×10^3
Chemical potential	μ/k_B	40 nK
Axial TF radius	R_z	30 μm
Radial TF radius	R_r	1.2 μm
Peak density	n_0	1.4×10^{14} cm^{-3}

Table 6.1: Properties of the condensate as obtained from the fits to the data using the Thomas-Fermi model.

corresponding to the condensate dominates the distribution in Figure 6.10(f). The position of the small thermal component in (f) is offset slightly from the condensed part, possibly due to sensitivity to slight trap distortions at low temperatures but the reason for this is not known for certain. Profiles (c) and (d) correspond to the same final rf frequency and are shown together for comparison of shot-to shot variations in temperature and atom number. The temperatures obtained from the fits in (c) and (d) differ by about 5 % and the atom number varies by about 15 %. The bimodal profiles of the clouds are very similar however.

6.3.3 Condensate Properties

The density profiles fitted to the data can be used to extract properties of the condensate produced in the videotape microtrap. Quantities of interest that can be obtained include the critical temperature, condensate chemical potential and size. The condensate can be seen to begin to form in Figure 6.10(b) with about 8×10^4 atoms and at a temperature of 205 nK. For the harmonic trap frequencies used in the experiment and this number of atoms the ideal gas critical temperature according to Equation 2.27 is calculated to be 230 nK. The measured temperature at the onset of condensation of just above 200 nK agrees well with the calculated critical temperature within the uncertainty of the measurement. The effect of finite number and interactions on the theoretical critical temperature is known to reduce the experimental value by a few percent [61] and this could indeed be the case here. However, the temperature measurements are not sufficiently sensitive to show this effect.

The physical size of the condensate is also obtained from the fits to the data. The Thomas-Fermi length ($2R_z$) of the condensed component in (d) and (e) is $2R_z = 60\,\mu$m. This corresponds to a chemical potential in the trap of $\mu/k_B = 40$ nK according to Equation 2.34. This can be compared with the chemical potential expressed in terms of atom number according to Equation 2.37 which also gives 40 nK for the $\approx 9 \times 10^3$ condensed atoms shown in profile (f). The radial size of the condensate and peak density can be calculated given these measurements and the properties are summarised in Table 6.1. The general agreement between the theoretical predictions for critical temperature and condensate size and the measurements obtained from the density profiles fitted to the data indicate that the non-interacting bimodal model is a suitable choice of distribution. The chemical potential of 40 nK is equivalent to a harmonic trap level spacing of $\omega = 2\pi \times 840$ Hz which is larger than the radial trap frequency of 335 Hz in the

experiment, indicating that the three-dimensional Thomas-Fermi description of the system is still an appropriate choice. It is however of interest to note that crossing into the 1D condensate regime could be achieved reasonably straightforwardly with the videotape atom chip and a detailed study of how condensate properties vary at low atom number and high radial trap frequency when $\mu \ll \hbar\omega_r$ is potentially a very fruitful topic for future work.

6.4 Discussion

It has been shown that atoms loaded into a videotape microtrap can be used to probe its properties in order to verify the theoretical model of the videotape potentials. Moreover, by implementing a final stage of evaporative cooling in the microtrap the trapped atoms can be cooled to Bose-Einstein condensation.

The size of the condensates produced in a videotape microtrap is reasonably small in comparison to the number of atoms available in the laser cooling stage of the experiment. There are many avenues available for optimisation of the experimental conditions including improving the coupling efficiency from the mirror-MOT into the centre-wire trap, further optimisation of the methods of loading a videotape microtrap and additional optimisation of the shape and duration of the evaporative cooling ramps used in the experiment. Each of these steps could potentially improve the number of atoms remaining at the end of the condensate preparation stage. Nonetheless, the current methods are certainly adequate as a means of preparing coherent samples of atoms as source for further experiments and the quantities compare reasonably well with other microtrap experiments. For future studies of quantum gases in low dimensions, low atom numbers will indeed be required although this will probably also have to be accompanied by the implementation of a more advanced detection system possibly involving micro-fibre optics and cavities integrated onto the chip.

The ability to prepare condensates in a videotape microtrap demonstrates that permanent-magnet micro-potentials in general and videotape in particular are compatible with the experimental conditions required to study ultracold quantum physics on a chip. To compare the general suitability of the microtraps for achieving more advanced goals involving coherent manipulation it is necessary to determine some particular properties that might distinguish the permanent microtraps from other technologies. An investigation into these properties forms the basis of the next chapter.

Chapter 7

Atom-Surface Effects

Ultracold atoms make remarkably sensitive probes of small magnetic fields. This chapter concerns using atoms to measure dc and ac field variations that become significant due to the close proximity of the atom chip surface. The chapter is split into two main parts. The first part discusses the fragmentation of atom clouds as they are brought close to the chip and the second part of the chapter concerns the lifetime of trapped atoms near the surface.

7.1 Part 1: Fragmentation

Atom chips provide confinement using magnetic fields generated on a surface only a few tens of microns away from the trapped cloud. This is in contrast to traditional magnetic trapping configurations which use electromagnets to trap atoms several centimeters away. The close proximity of the surface in atom chips makes ultracold atoms much more sensitive to small magnetic field fluctuations than in the traditional configurations. The distortion of atom clouds by spatial variations in the magnetic field is now a well-known effect in traps generated by current-carrying wires [20, 22, 30, 32–34]. The break-up of trapped atom clouds into lumps has generally become to be known as fragmentation and has been attributed to deviating current paths within the wires due to inhomogeneities in the physical structure of the wire [32,34,110,111], introduced as a result of the fabrication process. This is further confirmed by the fact that atoms held in an optical potential close to a surface at the same distance as an equivalent fragmented wire potential have been shown not to display fragmentation [20]. Although the fragmentation of thermal clouds and condensates in wire-based potentials does not prevent the efficient production of condensates for atom optics *per se*, the effect presents a significant difficulty in more complex applications for which surface microtraps might otherwise be well-suited. For example, attempts at atom interferometry using magnetic micro-structures have been seriously inhibited by the presence of rough confining potentials. In addition, addressing individual atoms, perhaps for implementing quantum gates, will require precise control of atomic positions, a task for which smooth confinement is required. The magnitude of the magnetic roughness can be reduced in wire-based traps by working further from the surface but

this prevents utilisation of the tight transverse confinement which micro-potentials otherwise so usefully provide. The task of reducing current path deviations in wire microtraps has become a technical challenge of improving and refining the fabrication process [111]. Advances have been made on this front, but it might seem a sensible strategy to avoid current-carrying wires altogether and their resulting current path deviations. Permanent-magnet potentials, such as those formed by videotape, provide radial confinement without the need for real currents and could potentially reduce the effect of fragmentation. The temperatures of trapped atom clouds reached in this thesis work are sufficiently low that the roughness of the magnetic potentials formed by the videotape potential can be probed with reasonable sensitivity for the first time. At temperatures below a few micro-Kelvin some fragmentation of the atom clouds was observed on the videotape chip. The effect appeared to become more severe closer to the surface. On the whole, experiments involving BEC described so far were performed sufficiently far from the surface that the effects of waveguide roughness were not dominant, however, further investigation of the severity of the waveguide roughness is of help for determining future directions involving the videotape, when working close the surface could be advantageous. A measurement of the roughness of the videotape waveguides is the subject of the first part of this chapter.

The structure of the section is as follows. It begins by outlining the method by which the rough potential may be extracted from absorption images of atoms confined in the waveguides. Experimental examples of the extracted potential are then given. This is followed by a discussion of the possible origin of the waveguide roughness including the results of a study of the surface quality of the videotape used. It concludes with a short discussion of how the roughness of videotape traps compares with that observed in wire-based traps and the prospects for future work involving the videotape waveguides.

7.1.1 Observation of Fragmentation

At high temperatures ($T > 5\,\mu$K) and far from the surface ($y > 90\,\mu$m), the profiles of thermal clouds in the magnetic trap are very well described by a Gaussian distribution. However as the temperature is lowered below a few μK, some additional structure within the cloud becomes apparent. This effect is shown in Figure 7.1 for an extreme example, demonstrating the onset of fragmentation at low temperatures. The images are taken at a distance of $85\,\mu$m from the surface as the temperature is lowered by evaporative cooling and the axial confinement has been relaxed to 9 Hz to allow the cloud to extend as far as possible in the z-direction. The temperature of the thermal cloud in Figure 7.1(b) where the fragmentation becomes significant is 250 nK. In Figure 7.1(c) the cloud has been cooled sufficiently to occupy two independent fragmentation potential wells.

The presence of fragmentation in the videotape waveguides is at first sight a curious effect because of the absence of real deviating currents which are the cause of such fragmentation in wire-based chips. The likely origin of the waveguide roughness is discussed in Section 7.1.4, but first a method of further quantifying the roughness will be introduced.

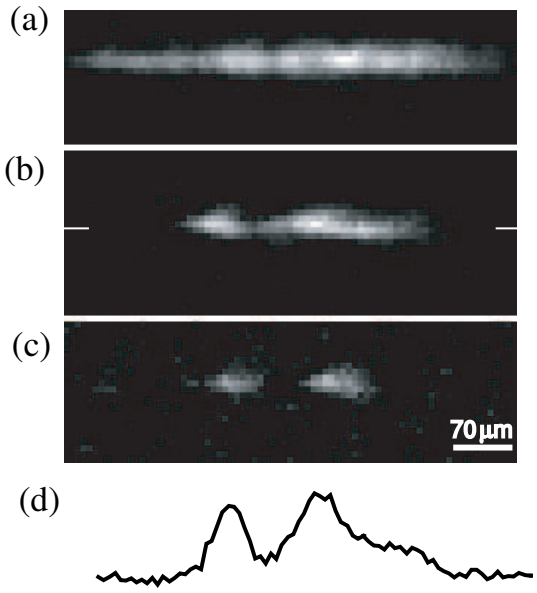

Figure 7.1: Fragmentation of a thermal cloud as the temperature is lowered by evaporative cooling. The cloud can be seen to break into two distinct lumps in (c). The profile shown in (d) corresponds to a cross section through (b) denoted by the white markers. The temperatures in (a) and (b) are 450 and 250 nK.

7.1.2 Obtaining the Fragmentation Potential

Cold atom clouds can be used to measure the waveguide roughness by comparing the expected equilibrium density distribution in a perfect trap with that of the experimentally measured density distribution in a fragmented potential. The Boltzmann law relates the density distribution ρ_r to the confining potential through the relation

$$V(r) = -k_B T \ln \rho(r) \tag{7.1}$$

The absorption images obtained in an experiment correspond to the column density integrated across the cloud and can therefore be used to describe the probability density of finding atoms in a particular region. The aim of the analysis is to separate the potential into two parts, the unperturbed harmonic trap (a parabola) and the fragmentation potential. By making use of the Boltzmann law, an absorption image can be analysed by taking the natural logarithm of the normalised density profile. Considering first the case of a pure harmonic trap of frequency ω_z, the resulting profile after taking the log is a parabola, $V(z) = az^2 + c$, where a fit to find a determines the temperature of the Gaussian thermal cloud via the relations $a = \frac{1}{2\sigma_z^2}$ and $k_B T = m\omega_z^2 \sigma_z^2$. The same procedure is used in the case of a fragmented cloud; however, in this case the resulting potential obtained after taking the log is not purely parabolic but contains additional structure resulting from the fragmentation potential. The fitted parabolic function must take this into account and pass through these deviations, as well as broadly

describing the parabolic envelope which is used to obtain T. The fitted parabolic potential can than be subtracted, leaving the residual fragmentation potential with an amplitude well-defined in units of temperature. The known Zeeman shift can be used to convert the obtained fragmentation potential into a spatially fluctuating magnetic field. The measured fluctuating field only corresponds to the z-component of the anomalous field and this must be taken into account when contemplating possible physical origins of observed fragmentation.

The method described above is best suited to analysing clouds that are only partially fragmented. If the temperature is too low and the atomic density profiles are broken up entirely, it is no longer possible to assign a temperature to the cloud using the parabolic envelope. In addition, the spatial extent of the cloud becomes small, limiting the amount of the fragmentation potential that is revealed by the method. The temperature of the cloud in the absorption image must be carefully chosen to provide enough contrast while simultaneously allowing the temperature to be obtained.

7.1.3 Depth of the Videotape Fragmentation Potential

Fragmented clouds in the videotape waveguides were studied for various distances from the videotape surface and the Boltzmann law was used to subtract the axial potential due to the end wires as described above. The residual fragmentation potentials obtained in this manner for three different distances from the videotape surface are shown in Figure 7.2 with the curves offset from each other for clarity. It can be seen that the variation of the fragmentation potential increases as the surface is approached. Very little variation can be seen at a height of $99\,\mu$m and at a distance of $41\,\mu$m the peak-to-peak variation of the potential has increased to $\simeq 2\,\mu$K. It is not possible to determine whether the fragmentation has a particulary well-defined spatial period at this height. However, over the small sampled area the fragmentation shows gross spatial variation with a characteristic wavelength of $\sim 150\,\mu$m together with smaller fluctuations of $25 - 30\,\mu$m period.

To obtain a more sensitive measurement of fragmentation far from the surface we return to the profile presented in Figure 7.1 (b). The fragmentation potential was determined in the same manner and is plotted in Figure 7.3. The peak-to-peak field fluctuations in this case are approximately 600 nK at a height of $85\,\mu$m. To obtain an insight into the mechanism causing the fragmentation it is instructive to examine the surface roughness of the videotape to determine what might lead to the observed spatial fluctuation in the magnetic field.

7.1.4 Surface Quality of the Videotape Material

A piece of un-recorded tape from the same cassette as the videotape used on the atom chip was examined by Dr. E. A. Curtis, Dr. S. Eriksson and F. Ramirez-Martinez using an atomic force microscope in tapping mode with a tip radius of 15 nm and a front-angle of $25\,^\circ$. The tape was orientated so that the magnetic side was scanned. Several scans of the surface were made sampling regions between 50 and $100\,\mu$m wide to gain an overall impression of the surface

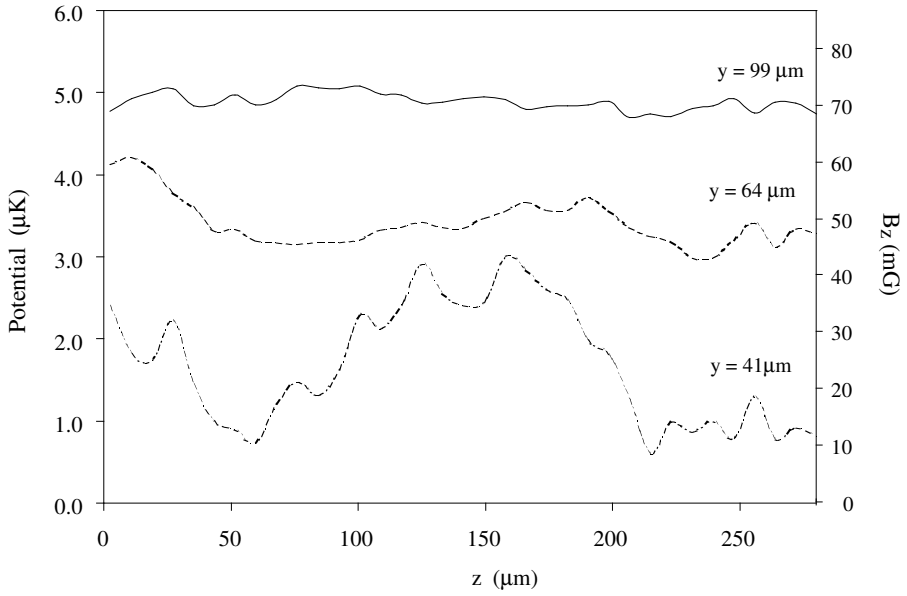

Figure 7.2: Fragmentation potentials for three different distances from the videotape surface. These are obtained from absorption image density profiles by subtracting the known axial potential using the Boltzmann law expressed in units of temperature. The plots are offset from each other for clarity. The field fluctuations are greatest close to the surface.

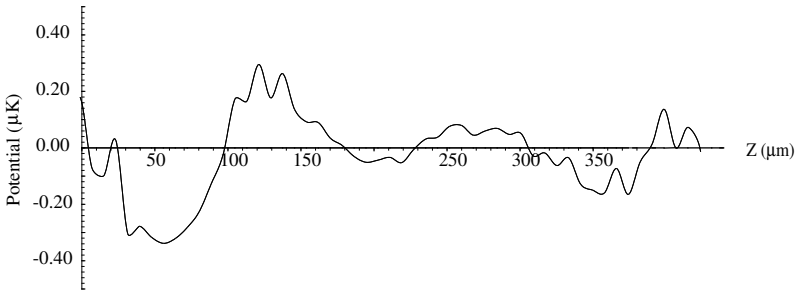

Figure 7.3: The determined fragmentation potential at 85 μm shows amplitude variations over $\sim \pm 300$ nK. The profile corresponds to the data shown in Figure 7.1.

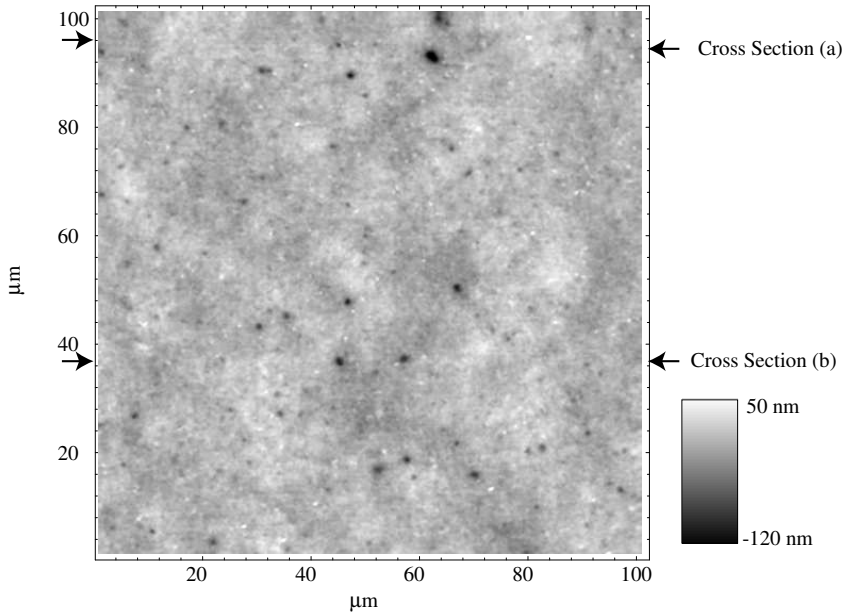

Figure 7.4: Atomic force microscope scan of a piece of videotape covering $100 \times 100\,\mu$m. The small dark features are defects on the surface of the tape approximately 100 nm deep. The arrows depict the rows shown in cross-section in Figure 7.5.

topography of the tape. The largest available scan, covering an area of $100 \times 100\,\mu$m, is shown in Figure 7.4. Broad background features with a spacing of tens of microns seen in the image are probably due to the inability of the tape to lie absolutely flat. However, the most striking feature of the scan is the many small, deep holes scattered throughout the surface of the tape. The origin of these defects is likely to be bubbles forming in the glue during the videotape manufacturing process. The typical spacing of the defects is $10\,\mu$m although there are also larger defects occurring every few tens of microns. Cross sections through some of these defects are shown in Figure 7.5. In scan (a) a cross section through one of the more prominent defects is shown, with a close-up of the defect itself in the inset. The defect is approximately $6\,\mu$m wide and 120 nm deep. In part (b) two of the smaller defects are shown on in the same cross section. In this case the defects are also around 100 nm deep and 4-5 μm wide.

It seems entirely possible at first sight that the resultant effect of these defects, distributed across the surface of the videotape, might be to cause an inhomogeneous magnetic field above the surface. This possibility is further considered in the following section.

7.1.5 Origin of the Videotape Fragmentation

The fragmentation potentials extracted from the data reveal a fluctuation in the z-component of the total magnetic field. It is necessary to determine how the defects in the magnetic surface of the tape could cause such a fluctuating field. The videotape is magnetised in plane and along the direction we call x. The magnetic layer, as mentioned previously, is formed by iron-

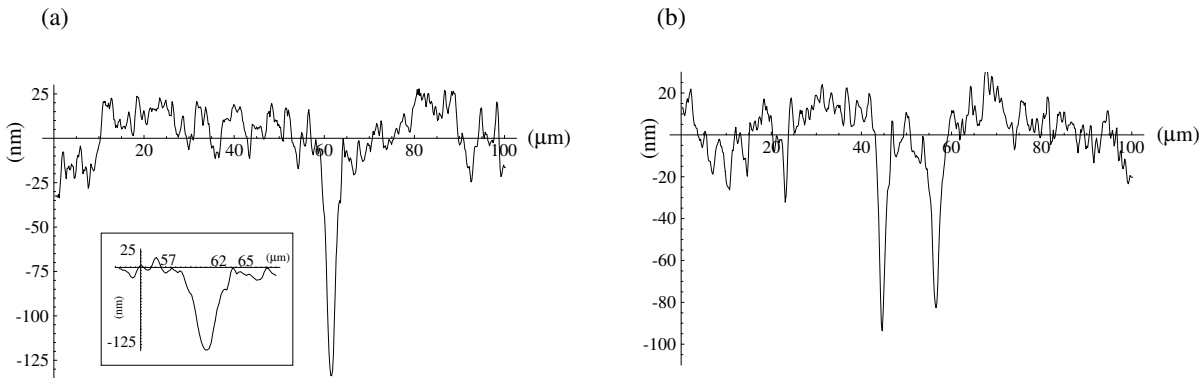

Figure 7.5: Cross sections through the AFM scan shown in Figure 7.4. (a) A section though one of the large defects at the top of the scan. The inset shows an enlarged profile of the defect, indicating a base-length of $\sim 6\,\mu$m. (b) A scan showing two slightly smaller defects that lie in the same row of the AFM scan. In both cases the defect depth is roughly 100 nm.

composite needles 100 nm long and set in glue. The simplest picture of a surface defect, from the point of view of the magnetic behaviour of the tape, is to consider it as a region of missing magnetisation. However, if the defects are indeed a consequence of bubbles expanding in the glue as it sets, then the situation is somewhat less straightforward. The magnetic needles would therefore be free to move within the setting glue, resulting in a potentially complex distribution of orientations of the magnetised needles around the edges of the defect. This situation will not be considered directly here since there is no reliable way to gain a detailed understanding of the actual needle orientations in the presence of a defect. However, the simpler case of missing magnetisation can be used to obtain some further insight.

Consider a rectangular slab with uniform in-plane magnetisation along the x-direction containing a disc-shaped defect recessed into the slab. At the edges of the recess the magnetic field changes direction and takes on a component along the z-direction, perpendicular to the magnetisation direction (x-direction). In Figure 7.6 the *z component* of the magnetic field is plotted above the surface. In this example, the recess has a radius of 1 mm and a depth of 0.1 mm and the field is plotted at a height of 0.15 mm above the surface of the slab. The defects in the surface of the videotape probably have a very similar magnetic behaviour to that shown in Figure 7.6 albeit on a microscopic scale. The approximation that the magnetisation is uniform in the slab surrounding the defect is valid in this case since the defects observed experimentally are much smaller than the videotape magnetisation wavelength of $100\,\mu$m meaning that variations due to the sinusoidal nature of the recording do not have to be taken into account.

It can be seen in Figure 7.6 that the field varies in size and sign across the x-z plane in the vicinity of a recess in the slab. If a number of such defects possessing similar magnetic properties were distributed randomly across the surface, the spatially varying B_z field components would interfere constructively and destructively resulting in a complicated field distribution across the surface, decaying with increasing vertical distance y, thus leading to fragmentation of cold

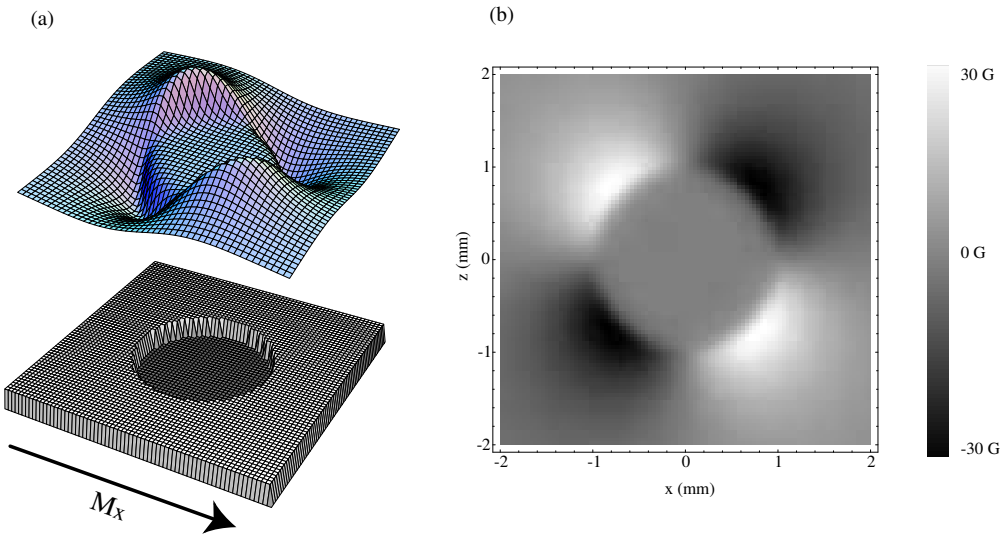

Figure 7.6: The z component of the magnetic field plotted above a circular recess in a uniformly magnetised slab. In (a) the slab and recess are shown with B_z plotted above. In (b) the same field is plotted in grey-scale. The field can be seen to vary in magnitude and sign in a plane above the recess.

atom clouds. In order to investigate this further it is necessary to consider multiple defects.

A section of missing magnetisation in a uniformly magnetised medium can be conveniently considered as a dipole source of field. In this case, the effect of the defects can be treated as a distribution of permanent dipoles in free space instead of a distribution of recesses in the magnetised material. This offers a useful simplification to the problem because the contribution of the videotape field does not have to be taken into account explicitly when calculating the total anomalous z-component due to the defects. A flat piece of tape magnetised in plane along x does not make any contribution to the field along z except at the edges of the tape, which can be ignored for sufficiently large areas. Therefore, in order to estimate the effect of the defects it is possible to make a simple model by considering them as a set of miniature dipoles with parallel magnetisation distributed on a planar surface. The main parameters of the system that can be varied are the geometry of the dipole (its shape and size) and the spatial number density of the distribution of dipoles in the plane. By constructing a numerical model and varying these parameters it is possible to estimate the magnetic contribution of the defects by evaluating the field above the surface of the tape due to the multiple defects.

To construct this simple model of the surface defects the ESRF Radia magneto-statics package was used in conjunction with Wolfram Scientific's Mathematica to generate and distribute the dipoles. To check the reliability of the system, a model of the magnetic videotape itself was constructed that reproduced the known analytical and experimental behaviour very well, valid for distances greater than 10 μm from the surface. Defects could be simulated by reversing the videotape magnetisation, however, as discussed above, it was simpler to remove the videotape

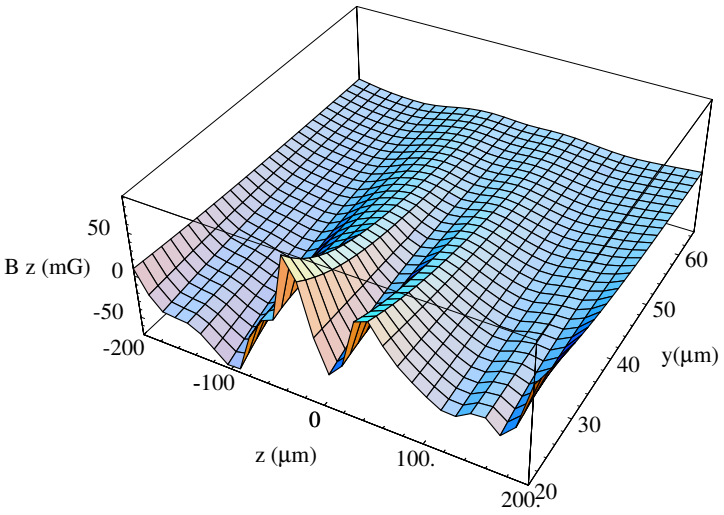

Figure 7.7: The B_z field along the z-axis plotted for increasing distance from the surface. The field shown is the result of a collection of circular magnetic dipoles distributed randomly across the surface in order to simulate the presence of surface defects. The field structure shows features similar to the experimentally obtained fragmentation potentials above videotape.

contribution altogether and consider only magnetised blocks replicating the defects, generated in the model and distributed in the x-z-plane. A number of different geometries of defect were constructed including magnetised rectangles, diamonds and discs, although the circular disc case was predominantly considered since that matches the shape of defects seen in the AFM scans most closely.

The size of the features that could be modelled stably was limited to approximately $10\,\mu$m. This is slightly larger than the features observed experimentally but nonetheless may be used to broadly determine the collective effect of defects. The magnitude of the resulting B_z field at a given point above the surface depends on the depth of the defect so quantitative comparison may be made by scaling the resulting field magnitude. Figure 7.7 shows the B_z component of field along the z-direction for increasing distance from the surface, evaluated at $x = 0$. The spatial density distribution was chosen so that there were approximately 2 defects per $100 \times 100\,\mu$m area, in line with the occurrence of the larger defects seen in the AFM scans. In the plot shown in Figure 7.7 a total of 8 of these large defects were randomly distributed over a $100 \times 400\,\mu$m area in the x-z plane. It can be seen that the resulting field has an irregular structure with characteristic scale of $100\,\mu$m, which deviates around the $B_z = 0$ point, reminiscent of the experimentally obtained fragmentation potentials. The magnitude of the field decays with increasing distance from the surface and the size of the field variations are a few tens of milli-Gauss, being 40 mG at $y = 40\,\mu$m. This demonstrates that randomly distributed surface defects are a feasible origin of the fragmentation phenomenon. A more accurate model would utilise smaller defects with varying sizes. A more sophisticated treatment could also consider more complex defect geometries such as cones and might possibly include some contribution due to

Group	Material	$\Delta B/B$
Heidelberg, Germany [111]	Microfrabricated gold conductors	$< 2 \times 10^{-4}$
Swinburne, Australia 2005 [53]	TbGdFeCo Magnetic Film	10^{-2}
London, UK	Betamax Videotape	5×10^{-3}

Table 7.1: Comparison between reports of $\Delta B/B$

the likely disordered orientation of the magnetic needles in the magnetic tape in the vicinity of a defect. It is of course also possible that the fragmentation observed in the experiments arises from the presence of much larger defects local to the trapping region that are not represented in the AFM scans available. In addition, a number of other phenomena could also contribute to the fragmentation effect including thickness variations of the videotape magnetic layer. However, based on the arguments given above it seems likely that the surface defects play a dominant role.

7.1.6 Discussion

Fragmentation of cold atom clouds in the videotape microtraps is an undesirable but seemingly unavoidable effect. There is a possibility that the region of videotape used in the experiments might induce particulary bad fragmentation and that by using another area of the tape the effect might be reduced. However, as the AFM scans show that the distribution of imperfections is reasonably regular and due to their collective effect, neighbouring defects displaced from the trap axis still have influence on the fragmentation. Nevertheless, it is still possible that an exceptionally high quality area of tape might be available for use.

If permanent magnetic materials are to continue to play a role in atom-chip technology it will be important to select the materials carefully with surface quality in mind. Magneto-optical thin films [112] might offer a suitable solution in this respect, as the surface quality is excellent in comparison to videotape. However, recent reports involving similar materials [53] indicate severe fragmentation is also present, due to the manner in which the edges of the film are manufactured.

Finally, it is worthwhile noting the severity of fragmentation depth in comparison to other microtrap technologies. The quantity most readily used to compare anomalous fields is $\Delta B/B$, where ΔB is the typical variation of B_z and B is the magnetic field produced by the surface at the height of the trap. Table 7.1 displays this ratio for three different materials, including the videotape described here. The fragmentation amplitude of videotape falls roughly between the best reported wire microtraps [111] and the particularly severe fragmentation observed using TbGdFeCo magnetic film [53]. It is encouraging that the potential roughness of the videotape is not severely limiting but further improvements in the materials chosen for generating permanent-magnet microtraps will have to be sought if this powerful method of trapping is to be used to its full advantage.

7.2 Part 2: Spin-Flip Lifetime near the Surface

The close vicinity of ultracold trapped clouds to the surface of atom chips has further implications beyond those associated with inhomogeneous trapping potentials. The accomplishment of confining atoms at micro-Kelvin temperatures just a few tens of microns from a material at room temperature is a remarkable one, but not without consequences that arise from these contrasting temperature scales. The most notable effect from an experimental perspective is the coupling of an atomic spin to thermal radiation modes generated by the surface, resulting in trap loss due to the increased probability of transitions into un-trapped spin states. This was first considered theoretically for microtraps by Henkel *et. al.* in 1999 [35] and has led to a number of reports of experimental observations of this effect [19, 21, 30, 31, 113]. The physics of the interaction is fundamental in origin but the ultimate bearing on the technical capability of atom chips to perform the tasks required of them involves attending to specific aspects of material choice, working distances and substrate temperatures. The following sections present results of the contribution of videotape microtraps to the area of surface-dependent lifetime. This begins with a summary of the mechanism responsible for spin-flip loss, which is followed by the results of experimental measurements of the lifetimes of thermal clouds held close to the videotape atom chip. The results are then compared to recent theoretical advances applicable to the system and followed by a short discussion of the implications of the results for atom chip microtraps in general.

7.2.1 Thermal Fluctuations and Spin-Flips

Reduced trap lifetimes as atom clouds were brought near to the surface of an atom chip were first reported in detail by Jones *et. al.* [19] for atoms trapped above a cylindrical copper wire. The authors were able to show that the distance dependence of the increased loss rate was not consistent with technical noise produced in the wire, but was rather a result of the coupling of the atomic spins to thermal fluctuations in the metallic surface. The lifetimes of atoms close to current-carrying wires have been studied under a number of experimental conditions but the results amount to a common situation; conducting materials significantly reduce the lifetime close to the surface. Reducing the material conductivity or using dielectric materials is a natural solution to the problem. The potential power of this was demonstrated by Harber *et. al.* [31] who verified the greatly improved lifetime near a dielectric compared to other higher conductivity surfaces. Although Harber *et. al.* were able to measure lifetimes close to a dielectric surface, it should be noted that the surface itself played no role in providing the atomic confinement. This is in contrast to atom-chip microtraps where the surface itself is the source of the confining potential. Gold coated videotape provides a unique situation in which to study the combined effect of a dielectric material and a thin conducting layer. The long background-gas-limited lifetimes achieved in the work presented here provided an opportunity to measure the contribution of the chip surface to the trap loss rate with good resolution and in potentials generated by the surface itself.

Initial investigations of the lifetime of atoms trapped in videotape indicated that the lifetime on the atom chip was not constant but instead had a dependence on height and should therefore be studied in more detail. Experimental results relating to the lifetime close to videotape are presented later in this section but first the physical mechanism behind thermal spin-flip loss and some theoretical treatments that are of relevance to interpreting the experimental data are briefly considered.

7.2.2 Loss Mechanism

Confinement in a magnetic trap requires that an atom remains in the same hyperfine spin state for long periods of time. If the spin spontaneously flips, or is caused to flip by an external perturbation, the atom will be rapidly lost from the trap when it transfers to an un-trapped state. In free space at zero temperature the rate of transitions is given by Fermi's golden rule:

$$\Gamma_{i\to f} = \frac{\mu_0}{3\pi\hbar c^3}\omega_{if}^3|\mu_{if}|^2, \tag{7.2}$$

where i and f denote the initial and final states, ω_{if} is the transition frequency and μ_{if} is the matrix element of the transition. For ^{87}Rb in the $|2,2\rangle$ hyperfine state flipping into the $|2,1\rangle$ state this rate is extremely low, only $5\times10^{-25}\,\mathrm{s}^{-1}$ at 1 MHz. The rate is modified at finite temperature T by the factor $\tilde{n}_{th} = \frac{1}{e^{\hbar\omega/k_BT}-1}$ which increases the rate to just $3\times10^{-18}\,\mathrm{s}^{-1}$ at 300 K. This contribution to the spin-changing transition rate does not therefore influence the trap lifetime on the timescale of experiments. However, the situation in close proximity to a surface is somewhat different.

Fluctuating thermal currents in the material produce a fluctuating field outside the surface which considerably modifies the transition rate for an atom in a magnetic trap through the associated fluctuating magnetic field. The critical factor that must be determined is $B_{ij}(\omega)$, the spectral density of the fluctuating field noise in the locality of the trapped atom, which depends on physical properties of the radiating material, including the geometrical shape. Length scales of importance are the skin depth of the material δ at the transition frequency ω and the characteristic dimensions (principally thickness) of the material, which determine in a simple picture the extent to which the fluctuating field penetrates the vacuum. The third length scale of note is the atom-surface distance which influences the fluctuating field strength at the position of the atom. A method of numerically interpolating the loss rate for a planar geometry has been available for some time [35] and has described experimental results reasonably well. Provided that $\delta \gg d \gg h$ this gives the dependence of the spin-flip rate on the material skin-depth δ, thickness, h and atom-surface distance d as $\Gamma \propto \frac{h}{d^2\delta^2}$ [10]. In an effort to develop a theory readily applicable to any geometry (in particular a cylindrical wire) the authors of Reference [114] used a different approach to calculate the spin-flip rate based on the calculation of the fluctuating radiation field at the observation point using a Green tensor method. This approach also ultimately requires numerical integration to obtain the spin-flip rate under arbitrary conditions, but in certain limits that are of relevance to atom chips, fully

quantitative analytical expressions for the rate can be obtained [115]. The particular limit of interest here is the case of a thin conducting film, such as the gold on the videotape atom chip. In this case the spin-flip rate is given by [115]

$$\Gamma_{|2,2\rangle\rightarrow|2,1\rangle} = \left(\frac{3}{8}\right)^2 \frac{\tilde{n}_{th}+1}{\tau_0}\left(\frac{c}{\omega}\right)^3 \frac{2h}{\delta^2 d^2} \tag{7.3}$$

where $1/\tau_0$ is the free space rate given in Equation 7.2. The relation is valid in the limit $\delta \gg d \gg h$. The recent theory has also been used to successfully re-analyse previous experimental results [19,21,114,115] and full reconciliation between the interpolation approach [35] and that of [114] has also recently been obtained [116]. The conclusion regarding the question of how to limit the spin-flip loss rate on atom chips is this. In the case of metals it is necessary to minimise the thickness of conducting materials and to carefully choose the resistivity and hence skin depth [117] or better still, use insulating materials. Cooling the substrate, for example by cryogenic methods, would also assist but adds unnecessary complication. Using super-conducting wires could potentially help the situation but there is some question as to whether this is the best strategy in practise due to subtleties revealed by the recent theory [115]. Working far from the surface is clearly a possible option but not one that allows chips to fulfill their full potential.

Using a dielectric material such as videotape and keeping any necessary conducting layers thin would seem to be a simple way to greatly reduce the spin-flip loss rate. In order to gain further insights into the loss mechanisms at play and to gauge the influence of these factors, experimental investigation is required, and this is the subject of the rest of this chapter.

7.2.3 Experimental Measurements Close to Videotape

The lifetime of trapped atoms close to the videotape atom chip was measured with thermal clouds. The procedure for measuring the lifetime was to prepare a cloud in a videotape trap far from the surface in the usual way by evaporative cooling. The cloud was then adiabatically transferred towards the videotape surface by ramping the B_x bias field over 3 s from its initial to final value. The end-wire current was reduced from 15 to 5 A during the ramp to reduce the amount of heating in the wires. Typical measurements could entail holding the cloud for times in excess of 100 s so the lower current was chosen to reduce outgassing and over-heating during lifetime measurements. The atom cloud was then held in the trap for a variable amount of time before the ramps were reversed and the cloud was brought away from the surface over 3 s to a bias field of 2.2 G. The cloud was then imaged by absorption *in situ*, or after release, to obtain the relative remaining atom number. This process was repeated for different hold times in the trap to obtain a set of data constituting a single lifetime measurement. The length of the hold times were chosen so that a reasonably long sample of the decay was obtained and probed out to hold times of usually more than twice the $1/e$ decay time. This measurement process was repeated for traps at varying distances from the surface with the aim of determining

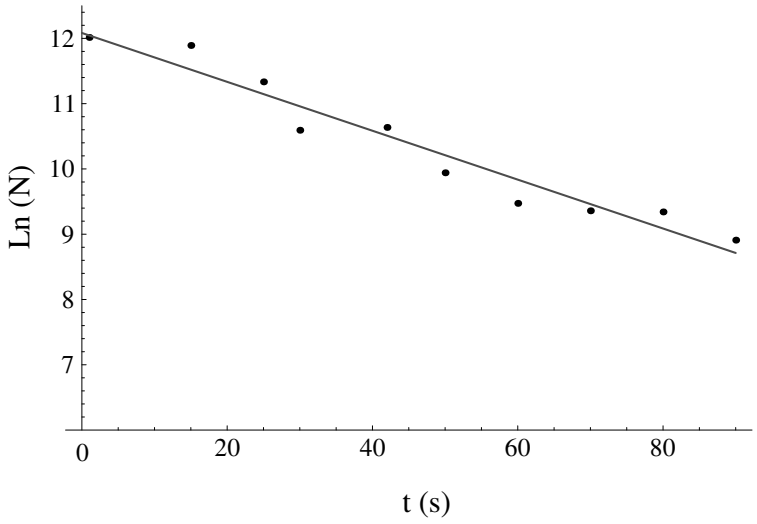

Figure 7.8: An example of a lifetime measurement made in a videotape microtrap. The trap is 72 μm form the surface and the $1/e$ decay time is 27.0 ± 2.4 s.

how the lifetime varied with distance from the surface of the atom chip. The measurements at different distances were performed in a random order to eliminate the effect of losses due to outgassing from the end wires. The atom-surface distance could be measured directly from a separate absorption image taken in the trap under investigation, obtained from the double image or calculated from the bias field used for the measurement. The initial temperature of the thermal clouds used in lifetime data sets ranged between 5 and 20 μK. During adiabatic transfer towards the surface the temperature should increase in proportion to the geometric mean of the trap frequencies and this corresponds to a factor up to ~ 6. The measurements were carried out at low densities such that 3-body loss did not play a role.

An example of a single lifetime measurement is shown in Figure 7.8. In this particular measurement the atom cloud was held 72 μm from the surface. The natural log of the atom number is plotted as a function of hold time in the trap. A least squares fit to the linear decay is used to obtain the lifetime from the gradient of the line and for the example shown in Figure 7.8 the $1/e$ lifetime is 27 ± 2s. In order to test the lifetime dependence on the distance from the surface a number of measurements were made at different distances. A set of lifetime measurements for different distances to the surface are shown in Figure 7.9. It can be seen that there is a marked reduction in lifetime as the surface is approached. In this data set the measured lifetime drops by a factor of 5 over a distance range of 85 μm. As this effect is not particularly subtle, it raises a question regarding the origin of the reduced trap lifetime. It is worthwhile to note even in this initial measurement that despite the *relative* increase in trap loss rate over this distance, the absolute values of the loss rates still compare very favourably with similar measurements close to thick metallic wires. It seems that, even without further consideration of the situation, that the use of a dielectric material and a thin gold layer already

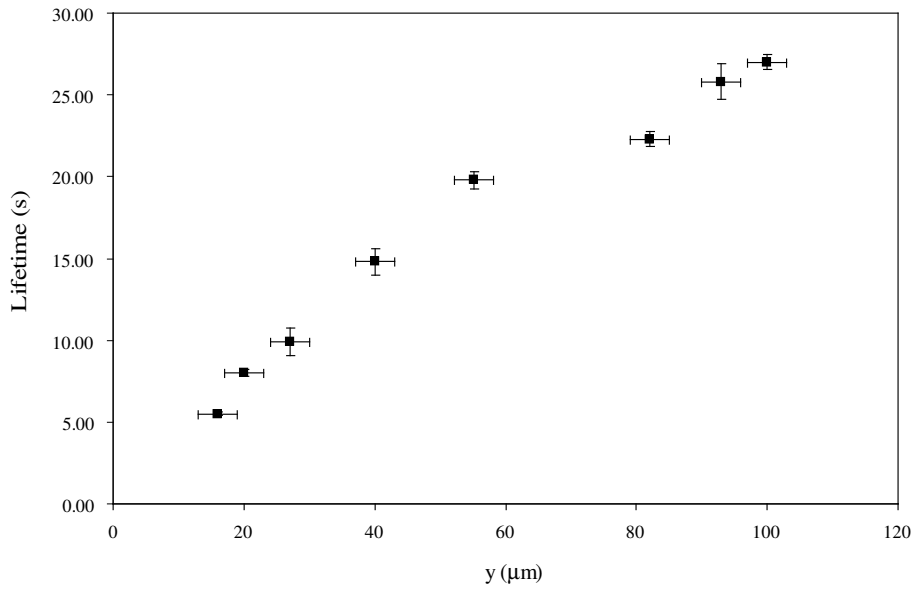

Figure 7.9: The lifetime of atoms trapped in a videotape microtrap plotted as a function of the distance y from the surface of the chip. It can be seen that the lifetime is reduced by about a factor of 5 over this range.

has some positive effect. Even so, it is of interest to determine if this is already a fundamental limit on the lifetime set by the rate of thermally induced spin-flips or is due to another effect essentially technical in origin. In either case, it is worth examining if further improvement on the lifetime can be achieved by making appropriate modifications to the available parameters. It was found that improvement in the lifetime was indeed possible and this is the subject of the following sections, but first the issue of technical noise is discussed.

7.2.4 Technical Noise

The only available method of changing the atom-surface distance in the videotape microtraps is to adjust the magnitude of the applied bias field. Wire-based traps have the added capability of adjusting the trap height by changing the current flowing in the wire. However, technical noise on the current in the wire is potentially an additional means of exciting spin-flip losses or increasing heating rates. Videotape should be less susceptible to such effects although this makes the task of eliminating technical-noise-related losses rather different because in principle they do not couple directly to the radial trapping potential, as is the case with wires. It might seem then that the most likely way technical noise could have an influence with a height dependence is if it were present on the bias field itself although this would have a different scaling with height than say, for example, thermal spin-flip loss. However, considering and eliminating possible sources of technical noise is important, the most relevant contribution being from rf noise at the Larmor frequency of trapped atoms.

Noise in the megahertz frequency range was investigated using an rf spectrum analyser, both with a pick-up coil and by measuring across the sense resistors in the circuits controlling the various current-carrying wires and magnetic-field coils used in the experiment. A very prominent source of broadband rf-noise was the vacuum ionisation gauge and controller unit (Varian UHV-24 L8350301 Multi-Gauge) which is used to measure the pressure in the main chamber. This produces ambient noise that is picked up by many of the devices in the laboratory and it was therefore ensured that all measurements were performed with the device switched off. Additional steps were also taken to ensure that the high-voltage ion pump supplies were not generating significant rf radiation. With these sources of noise eliminated, very sensitive measurements of the contribution of remaining rf signals could be made. It was possible to identify and rectify contributions from an oscillating photodiode power supply at 3.1 MHz and a 5 V power supply oscillating at 1.45 MHz. Beyond this, the only detectable source of rf noise in the vicinity of the vacuum chamber was due to another ionisation gauge in the laboratory with a center frequency of 4.8 MHz, contributing -70 dBm in a 300 kHz bandwidth.

After taking all practical steps to reduce rf noise, no change in the experimental trap lifetimes was observed, providing a good basis on which to be confident that the observed trap lifetime reduction close to the surface was due to another effect such as spin-flips induced by the surface. With the aim of achieving the longest trap lifetimes possible, further investigation of the microtrap lifetime dependence on parameters under experimental control was made.

Briefly, it is also worthwhile noting the possible processes that set an upper-limit on the lifetime. Collision with hot atoms in the background gas is the most prominent loss-mechanism. The long MOT lifetime and measurements of base pressure in the main chamber both indicate that this rate should be low. In practise the upper limit of the magnetic trap lifetime was around 35 s. Although this is in itself very good and sufficiently long for most experiments, it is conceivable that despite the excellent UHV base pressure, local outgassing in the vicinity of the atom chip due to heating in the centre wire and end wires during the earlier stages of the experiment actually determines the background gas limited lifetime rather than the base pressure. Indeed, after prolonged periods of running current through the wires some increase in the gauge pressure reading was noticeable due to outgassing. Another possible limiting factor on the lifetime is stray resonant light. When present, even in very small amounts, this leads to a dramatic reduction in lifetime. Every effort was made to eliminate possible sources and it is thought that this bears little or no influence in these measurements.

7.2.5 Adjusting the Axial Bias Field

The most significant influence on the lifetime was achieved by adjusting the magnitude of the axial bias field B_z. Normally this field was used to cancel the contribution of the end wires and reduce the net axial field. However, by adding a field along z rather than subtracting it, net axial bias fields of up to 25 G could be obtained. This has the effect of changing the Larmor frequency of magnetically trapped atoms and consequently adjusting their sensitivity

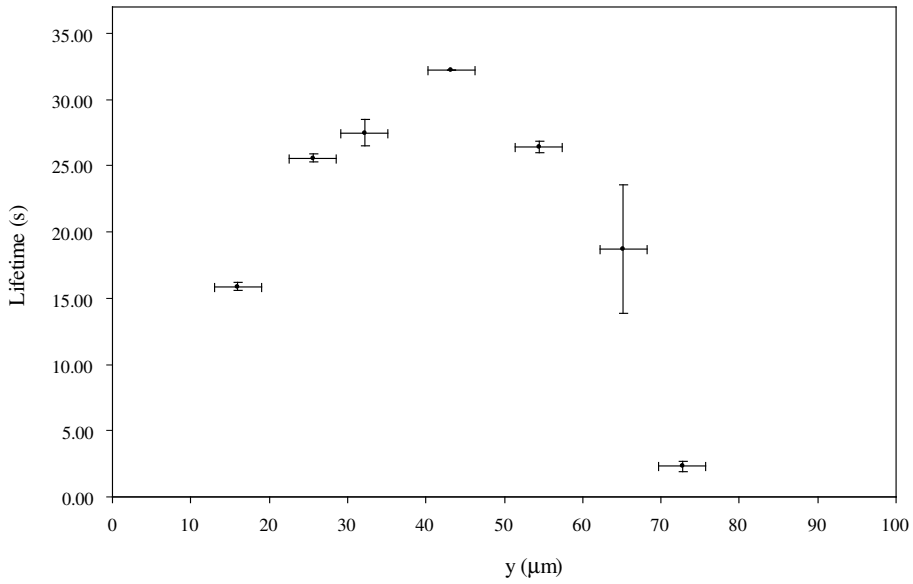

Figure 7.10: Lifetime of atoms in a videotape trap measured as a function of distance from the surface with a net axial bias field of 12 G. Close to the surface the trap lifetime is increased by the application of the axial field and far from the surface atoms are rapidly lost from the trap due to evaporation at finite trap depth (see text).

to rf fields capable of ejecting atoms from the trap.

The axial field was supplied by the pair of Helmholtz coils mounted outside the main chamber and added to the B_z component of field produced by the end wires. In order to apply the axial field during a lifetime measurement, the B_z field was ramped up during the 3 s transfer towards the surface and ramped off again during the 3 s ramp out of the trap in question before the image is taken. The lifetime close to the surface, where the loss rate is apparently not dominated by background collisions was monitored as a function of applied B_z field. It was found that the lifetime steadily increased up as the applied B_z field was increased to 12 G beyond which point no further improvement was obtained for fields up to 20 G. *In situ* images were taken to check that the addition of this field had no effect on the atom-surface distance. Having established that larger axial fields improved the lifetime close to the surface, the height dependence of this effect was sought. Lifetimes measured as a function of height with an net axial bias field of 12 G are shown in Figure 7.10. Two main features of this trend are in contrast to the plot previously shown in Figure 7.8. First, the lifetime at small distances from the surface ($y < 45\mu$m) is longer than those measured without the large axial bias field as mentioned above. Second, and perhaps more surprisingly, the lifetime far from the surface is greatly reduced and becomes negligibly small at distances beyond 75 μm. It is of experimental interest to be able to improve the lifetime of trapped atoms in this way but also curious to also observe a new loss mechanism. The increased lifetime close to the surface is discussed further below, but first the reason for the loss far from the surface is considered.

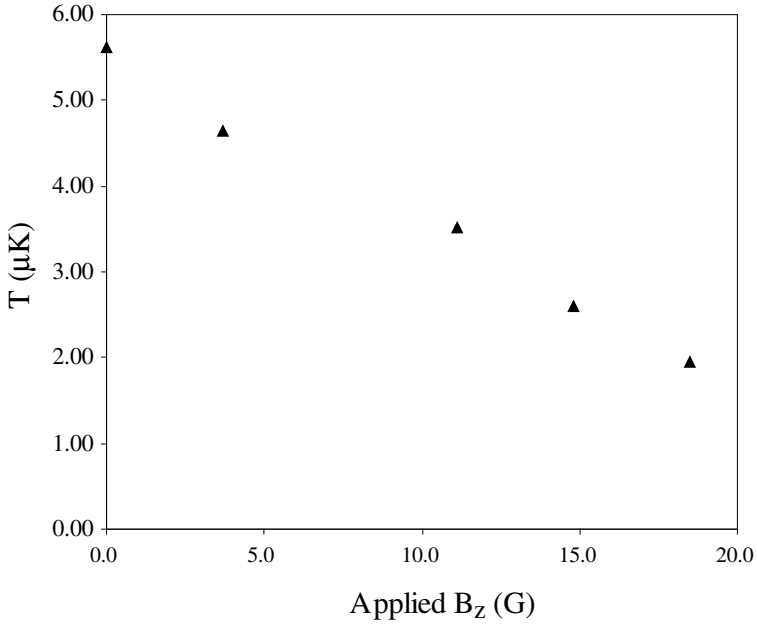

Figure 7.11: Reduction of the temperature after being held in a trap with a bias field of 2.2 G for 25 s as a function of the applied axial bias field B_z. The temperature falls with increasing field.

7.2.6 Evaporation Losses at Low Trap Depth

The loss rate of atoms from the microtrap increases dramatically far from the surface when a large axial bias field is applied. However, this is not the only observed effect under these conditions. As well as rapid atom loss, the length of the cloud in the image is seen to shrink, indicating the trapped cloud has a lower temperature after each measurement has been made. The reduction in temperature was greatest for the largest applied axial fields. The reduction in temperature suggests that an evaporative cooling process is taking place, which would account for both the temperature drop and atom loss. Reduced radial trap depth at high axial bias fields is the likely cause. The reduction in temperature is illustrated in Figure 7.11 in which the temperature is plotted versus the applied field after holding the cloud in a trap 60 μm from the surface for a constant time of 25 s. In Figure 7.12 the reduction in temperature as a function of hold time is shown at a B_z field of 21 G. The cloud reduces in temperature slowly in the trap as time progresses. The increase of cooling and trap loss with increase in axial bias field strongly suggest the effects are linked and caused by evaporative cooling at reduced radial trap depth. When a large axial bias field is applied, the consequence in the z direction is simply to offset the field upwards. However, the radial trap depth is reduced in the y-direction. The radial trap depth in this direction is given by $U = \mu_B(\sqrt{B_x^2 + B_z^2} - B_z)$ so when B_z becomes much greater than B_x the trap depth can become very shallow, resulting in truncation of the thermal energy distribution $\eta = \frac{U}{k_B T}$. For instance, for the case of the trap used in Figure 7.11 the trap depth is reduced to 130 mG at the largest B_z, which for a cloud with an initial

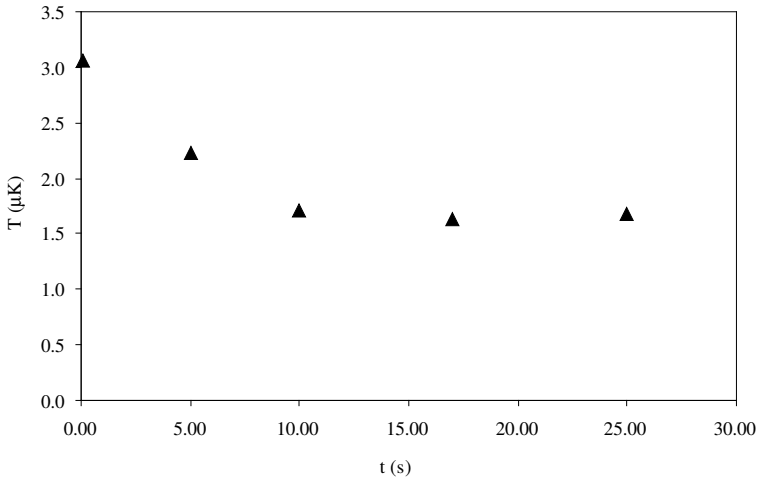

Figure 7.12: Time-dependent reduction of the temperature as a function of hold time in the microtrap for $B_x = 2.2\,\mathrm{G}$ and $B_z = 21\,\mathrm{G}$. The temperature can be seen to reduce with time until it reaches equilibrium after about 15 s.

temperature of $5\,\mu$K represents a truncation parameter of $\eta \simeq 1.7$. This would be expected to result in very clear evaporation and subsequent thermalisation to a lower temperature through collisions. The data in our case suggests that evaporation-induced losses become negligible for B_x bias fields greater than $\sim 10\,\mathrm{G}$ in these experiments. One dimensional evaporation is a mechanism that has previously been used to describe losses due to Casimir-Polder limited trap depth less than $2\,\mu$m from a dielectric [21]. In our case however, trap-depth limited lifetime is an artefact of the experimental set-up that could in principle be reduced by changing the parameters of the system. It does not yield insight into the extent to which fundamental processes such as thermally induced spin-flips play a role in the videotape atom chip lifetimes. In order to examine this aspect further, the next section returns to the issue of the lifetime near the surface.

7.2.7 Comparison with Theory for Thermal Spin-Flips

It was seen in Section 7.2.5 that the lifetime close to the surface could be improved up to a point by applying a large axial bias field, beyond which no further increase was obtained. This strongly suggests that the lifetime is fundamentally limited by another process, most likely thermally induced spin-flips and this situation is considered further in this section.

The two materials closest to the trapped atoms are the videotape itself and the gold and chromium layers coated onto the videotape surface. Although the videotape magnetic layer contains iron composite needles, the glue separating them means that the videotape is effectively an insulator. Indeed, crude measurement indicates that the resistivity of the videotape is at least a million times that of gold. The dominant contribution to thermal noise should therefore be from the gold layer. The thickness of the gold layer was not measured before installation

of the tape and must be estimated from the recollections of B. V. Hall and J. A. Retter about the coating process. An agreed value is $400\,^{+100}_{-300}$ nm. This will be determined more precisely when the chip is finally removed from the experiment next year. The chromium adhesion layer was 5-10 nm thick. The gold layer is much thinner than the conducting layers used on most atom chips, typically 3-5 μm, and therefore should result in a significantly decreased spin-flip loss rate as appears to be the case. To test whether the measured lifetimes are consistent with thermal spin-flips caused by the gold layer the results were compared with theory describing the spin-flip loss rate.

The advances reported in Reference [115] allow us to compare the experimentally obtained data close to the surface with the derived analytical expression in the appropriate limit, given in Equation 7.3. The parameters required by the analytical solution are the temperature of the material and the thickness of the conducting layer. The temperature of the chip is estimated to be 350 ± 50 K, based on heating due to the wires onboard the chip which are turned on for 12 s or more during a typical experimental cycle. To compare the data directly with theory, a background limited lifetime of 35 s is also included via the relation

$$\frac{1}{\tau_{\text{total}}} = \frac{1}{\tau_{\text{spin-flip}}} + \frac{1}{\tau_{\text{bg}}} \tag{7.4}$$

The spin-flip loss is assumed to take place as a cascade from $|2,2\rangle \rightarrow |2,1\rangle \rightarrow |2,0\rangle$. The $|2,1\rangle$ state is also magnetically trapped and so to describe the experimental data an effective lifetime that sums the two populations is used. By considering the relative transition strengths and solving the population rate equations the normalised magnetically trapped population is given by $P_{|2,2\rangle+|2,1\rangle} = \frac{1}{5}\left(6e^{\frac{-t\Gamma_{2\rightarrow1}}{2}} - e^{-3t\Gamma_{2\rightarrow1}}\right)$, using the fact $\frac{\Gamma_{2\rightarrow1}}{\Gamma_{1\rightarrow0}} = \frac{2}{3}$. Assuming equal detection efficiency for the two states and relating the time-evolution of this solution to the experimental method, the theoretically calculated lifetime is multiplied by a factor of 1.7 to compare it directly with the data.

Figure 7.13 shows the four data points taken closest to the surface of the chip that were previously plotted in Figure 7.10. Five theory curves are also added to this plot based on the analytical expression given in Equation 7.3. The thick solid line is plotted for a 400 nm layer of gold at a temperature of 350 K. The two thick dashed lines to either side denote $\pm$50K. The short dashed lines represent $\pm$100 nm boundaries on the gold thickness. It can be seen that there is good agreement between the theoretical prediction and the data including the various uncertainties in the relevant parameters. The dot-dashed line shows how loss due to technical noise would scale if it were directly proportional to the applied bias field B_x, offset to pass through one of the data points. In this treatment, no contribution from the videotape material is included since it is likely to be very small. Although the Larmor frequency generally plays a role in the theoretical model it does not in the limit of Equation 7.3 we consider here because the quantity $\tau_0\omega^3\delta^3$ is proportional to ω^{-1} and so is $\tilde{n}_{th} + 1 \simeq \tilde{n}_{th}$. Primarily, the results show that the presence of the gold layer can explain the trap loss dependence on atom-surface

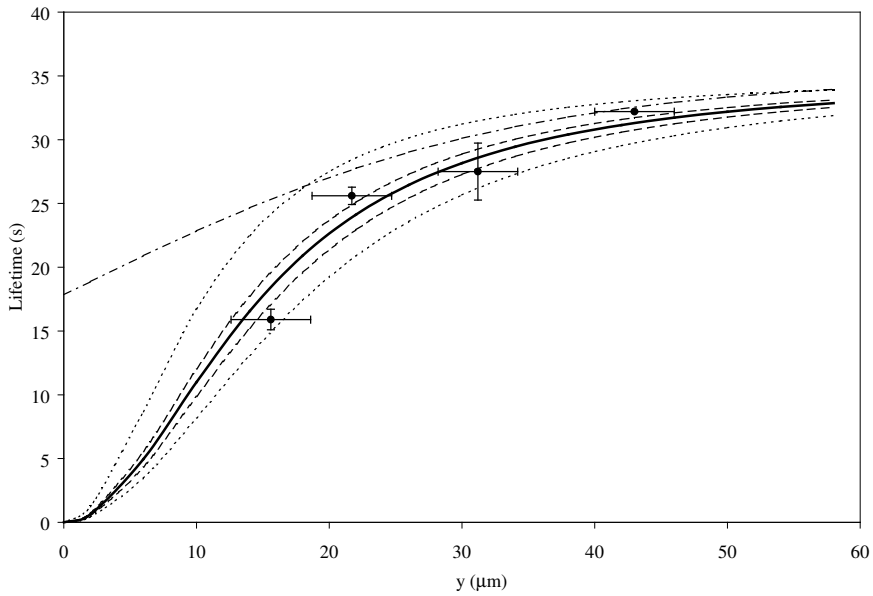

Figure 7.13: Comparison of measured lifetimes with the theory for thermally induced spin-flips. Data points: experimentally measured lifetimes. Solid Line: theory for 400 nm of gold at 350 K and ±50 K (thick dashed lines) and ±100 nm (thin dotted lines). The dot-dashed line is the scaling for technical noise if it were proportional to the applied bias field B_{bias} offset to pass through a data point.

distance over this range. The large axial bias field is most likely required to tune the spin-flip Larmor frequency in a manner that is not taken into account in the theoretical treatment. This may indeed be due to an auxiliary thermal spin-flip contribution from the videotape material that could be clarified with experiments with a thinner gold layer or by further development of the theory. This presently remains an open question.

7.3 Conclusion

In conclusion, the videotape offers an environment in which atoms may be trapped close to a surface with long lifetimes. However, it seems that if the full potential of videotape as a dielectric material is to be exploited in future, the metallic layer must be reduced or eliminated entirely, potentially allowing background limited lifetimes at all heights. This could be achieved by using a dielectric coating to make the mirror on the videotape rather than gold. Even so, the videotape atom chip used in these experiments has proven to be very suitable for forming atom traps in the respect that the lifetimes achieved compare extremely favourably with its current-carrying wire based counterparts. For example Jones *et. al.* reported spin-flip limited lifetimes of only a few seconds over a similar distance range to that investigated here [19]. Videotape and other dielectric materials clearly have an important role to play in future applications where long trapping times are required. If the fragmentation effects close to the surface can also

be reduced further by appropriate material choice then permanent magnetic microtraps will continue to be able to contribute profitably to the field of atom optics on a chip.

Chapter 8

Conclusions and Outlook

8.1 Conclusion

In this thesis Bose-Einstein condensation of a rubidium vapour on an atom chip constructed from a piece of periodically magnetised videotape was described. This is the first time BEC has been prepared in a microscopic surface trap based on permanent magnetisation and opens the door to future investigations of quantum gases in more complex permanent magnetic potentials or in lower dimensions. An essential part of achieving BEC was to begin with large collections of atoms under excellent vacuum conditions, for which purpose a high-power laser system and double MOT system was implemented as described in Chapters 3 and 4. In order to load a small volume microtrap close to the videotape surface a suitable method of capturing and transferring cold atoms into a microtrap was required as described in Chapter 5. Evaporative cooling in a videotape microtrap allowed small clouds to be prepared in order to examine the properties of the traps, aided significantly by the ability to image atoms in a microtrap close to the surface, utilising the gold mirror on the atom chip. Further cooling resulted in Bose-Einstein condensation of around 10^4 atoms and static properties of the condensate were obtained by comparing non-interacting bimodal Thomas-Fermi density distributions and expansion scaling factors to time of flight data.

In an effort to establish a comparison between videotape and other atom chip technologies that display some undesirable technical and fundamental limitations, the magnetic homogeneity of the waveguides and trap lifetime close to the surface were studied, as presented in Chapter 7. It was found that some fragmentation of atom clouds occurs at low temperatures close to the surface due to waveguide roughness and an explanation for this effect was offered, based on measurements of the videotape surface quality. The lifetimes of cold clouds held in the videotape microtraps were much longer than those previously reported on atom chips. The trend describing the reduction of lifetime as the surface was approached was in good agreement with theory based on thermally induced spin-flips due to the gold mirror on the surface. The long lifetimes provide a direct demonstration of one of the very positive features of permanent magnetic microtraps, providing encouragement for their continued use on atom chips.

Overall, it seems that videotape microtraps are suitable for tightly trapping cold atoms and condensates close to a surface and that further development of permanent-magnet microtrapping methods holds great promise for the future.

8.2 Future Directions

A number of exciting avenues for future work are available - both with videotape and with other magnetic materials and integrated optical devices. A few of these possibilities are outlined below.

Atomic Conveyor Belt It was proposed some time ago that it is possible to translate atoms trapped in videotape microtraps across the surface of the chip by rotating the applied bias field in the x-y plane [41,45]. This could be achieved with the present videotape atom chip and would demonstrate the ability to transport cold atoms or condensates from a preparation region to an interaction region which will be essential for nearly all future experiments.

Dynamics in a Disorder Potential The collective dynamics of cold atoms and condensates in a videotape trap have been studied in a rudimentary way [52]. However, expansion and oscillation appeared to be inhibited by the inhomogeneous waveguide potential. The effect of transport in so-called 'disorder potentials' has been the source of some recent interest in the community. Two publications have reported studies of the expansion of condensates in disorder imposed by laser-speckle [118,119] in the hope that comparisons with other condensed matter systems might be drawn. The inhomogeneous potential in the videotape waveguides might also provide a possible setting in which to study similar effects.

Low-Dimensional Quantum Gases The videotape traps can be formed with very high trap aspect ratios, making it possible to enter a regime in which effects due to the low-dimensionality of the system become interesting. Observing the behaviour of condensates in this regime, by measurement of collective oscillation frequencies in the first instance, will allow a thorough investigation of these effects. However, a practical realisation is likely require an improvement to the homogeneity of the trapping field (see below).

Magneto-Optical Thin Films Magneto-optical (MO) films based on Pt/Co multi-layers have been developed in our laboratory as a method of forming atom traps [112]. It is possible to 'paint' arbitrarily complex magnetic patterns on a one-micron length scale, greatly enhancing the sophistication of the trapping and guiding geometries available and allowing extremely tight transverse oscillation frequencies. Perhaps most importantly, MO-films are deposited in thin layers on a silicon substrate and appear to have a much better surface quality than videotape, potentially eliminating the effect of fragmentation altogether.

Integrated Optical Elements Atom chip technology is developing fast. The realisation of many of the interesting applications of chips will depend on the ability to include optical devices on the chip for detection of single atoms or for cavity QED [12]. This task is already well underway in our laboratory [120] where it is now possible to create small volume, open access high-finesse cavities capable of detecting a single atom [121]. Incorporating such devices onto atom chips is now a priority. The prospect of using fibre-coupled light to form miniature optical dipole traps on the chip is also very appealing. A condensate loaded into a standing-wave created by opposing fibres on the chip could be made to undergo the transition into a Mott insulator phase [122], resulting in a single atom per lattice site, an exciting starting point for further quantum manipulation.

Overall, the prospects for Bose-Einstein condensates in microtraps on chips are very promising indeed.

Appendix A

Rubidium Structure

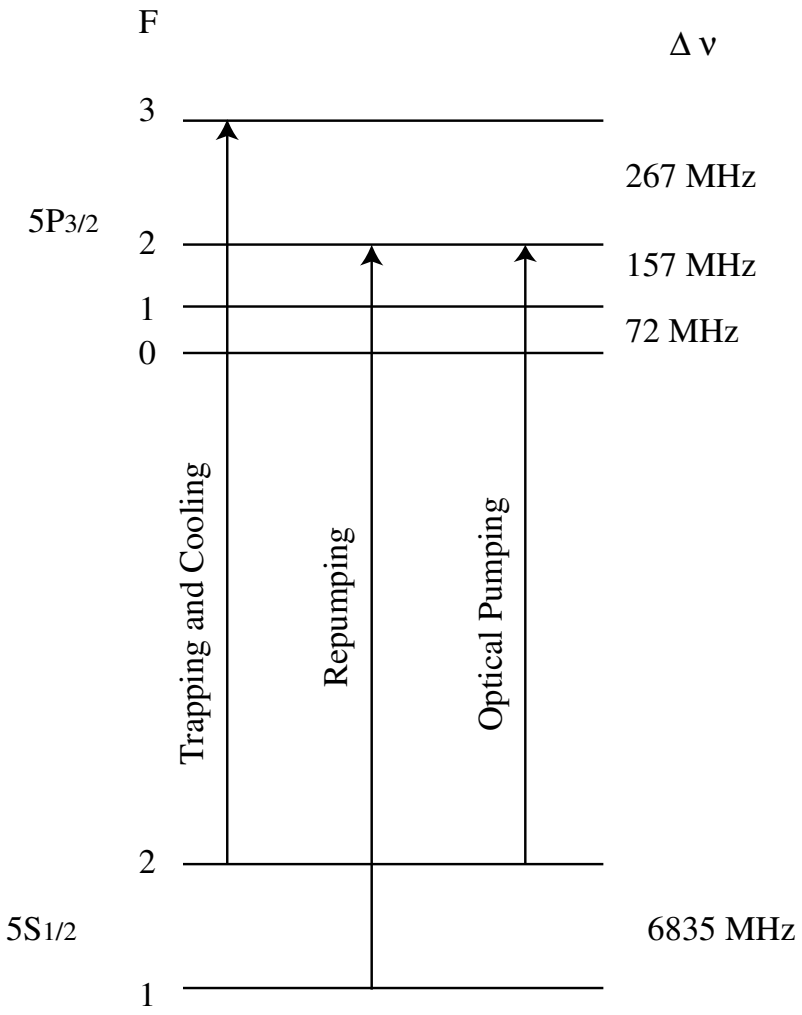

Energy level spacing of ^{87}Rb. Hyperfine splitting values as reported in References [123] and [124].

Appendix B

Achieving Ultra-High Vacuum

It is necessary to open the vacuum chamber intermittently to perform maintenance or alterations. When the vacuum system is sealed again a careful procedure must be followed to ensure that ultra-high-vacuum conditions can be achieved. This process involves ensuring the system is free from contaminants which can outgas, thus compromising the vacuum. Therefore the system was heated (baked) to remove water vapour and other contaminants from the walls. The pump-down and baking processes are described in this appendix.

When opening to atmosphere, the system is vented with argon or nitrogen so that the first gas to come into contact with the chamber walls is not room air, which contains substantial water vapour. A minimal flow of gas is maintained at all times to create a small positive pressure within the chamber. When closing the chamber again the gas flow is removed and all bolts are tightened evenly to form clean knife-edge seals with the copper gaskets. Usually some anti-seize grease is applied to the bolts and plate-nuts, taking great care not to let any grease come into contact with the surfaces of the flanges. Next, the pump-down and baking can commence.

The limiting temperature of the bake is 120 °C, determined by the videotape and epoxy used on the atom chip. All components used in the vacuum system are thoroughly cleaned with detergent and water and then with methanol in an ultrasonic bath and handled only with powder-free latex gloves.

All of the coils and optics mounted on the outside chamber are removed to allow access to the surface. The chamber is heated evenly to avoid any cool spots where contaminants can accumulate. Probably the best way to achieve uniform heating would be to enclose the whole chamber in a well-insulted baking oven equipped with electric heating elements and thermal feedback. In early tests with prototype LVIS chamber designs, such an oven was used to bake for short periods. However, the large physical dimensions of the fully assembled vacuum system prevented the use of a bakeout oven. Instead, the chamber remains on the optical table and is baked *in situ* by wrapping it evenly with heater tape. Care is taken to ensure the tape was applied evenly to the chamber surface area. Special care is taken to unifromly heat the bellows on the atom chip mount. Without sufficient baking of the bellows it was not possible to obtain

final vacuum pressures better that 1×10^{-10} torr due to outgassing from material trapped in the bellows.

Once wrapped in tape, connections are made to the various electrical feedthroughs so that current can be run through the wires, dispensers and NEG pump during the bake. The ion pumps on the LVIS and main-chambers are connected with bakeable cables so they can be activated while the chamber is hot. K-type thermocouples are attached at various points to allow the chamber temperature to be monitored throughout the bake. Lens tissue is placed over each window and the entire chamber is wrapped with several layers of aluminum foil to assist in trapping the heat. Fibrefrax Durablankets are then wrapped around the chamber to provide further thermal insulation. The bellows connecting the gate valve to the pumping station are also wrapped in heater tape, foil and a blanket. A residual gas analyser (RGA) is connected in series with the turbo pump to monitor the gas evolved during the bake.

Once the system is sealed and the argon flow disconnected the pumping station can be started. A 70 l/s turbo pump (Varian Turbo-Dry 70), backed by a diaphragm roughing pump was used to pump down the system. Providing no serious leaks are present, the turbo pump spins up to full speed in just a few minutes. It is prudent to turn on the RGA at this point and perform some helium leak checking.

After several hours of pumping with the turbo, the bake commences. The chamber is brought up to the desired equilibrium temperature over several hours by slowly increasing the voltage applied to the heater tape. The viewports cannot be heated any faster than the manufacturers specification of 3 degrees per minute. Slow heating of the system also helps to prevent accidental overshoot of the final baking temperature that could damage the atom chip. During the early stages of heating the mass spectrum measured by the RGA is usually dominated by water and carbon dioxide.

Between 5 and 7 Amps are run through the atom chip wires to ensure they are not the coldest part of the chamber. The voltage required to draw this current is monitored to check for evidence of thermal runaway. During the bake 2 A (just below the threshold for rubidium production) is normally run through the dispensers.

After achieving the desired bake temperature the system is usually left to pump with the turbo alone for 24 hours or longer. At this point the ionisation gauge is switched on to monitor the pressure. Typically the pressure is in the mid 10^{-6} torr region at this stage.

The ionisation gauge is usually degassed for 15 minutes using the facility provided by the controller unit. At this stage the NEG pump filament is reactivated using its integral heater cartridge. The current in the heater is increased over 40 minutes from 1 A to 4 A and held at 4 A for an hour or longer. During the reactivation of the NEG the RGA mass spectrum is almost entirely dominated by hydrogen released from the surface of the filament and the pressure rises to typically 1×10^{-5} torr. After turning off the heater element the refreshed NEG starts to pump very effectively and the pressure drops rapidly into the mid 10^{-7} torr range.

After the degassing and getter activation the ion pumps are turned on. Normally the ion pumps on the LVIS and main chambers are left to pump in tandem with the turbo for up to

24 hours before the gate valves to the turbo pump are closed finger tight. The chamber pressure continues to fall into the mid 10^{-8} torr range over a day or so. The heat is then turned down over several hours and normally left overnight to return to room temperature. At this stage it is usually apparent if UHV conditions had been achieved.

The gate valves are closed with a torque wrench to 10 ftlb before turning off the turbo pump. To reduce the differential pressure between the UHV side and atmospheric pressure, the cavity behind the valve is rough pumped to $\sim 10^{-2}$ torr and sealed with a threaded valve finger tight.

The pressure then continues to drop over several days until the final equilibrium base pressure is reached. The lowest base pressures reached were below 1×10^{-11} torr.

Bibliography

[1] Peter J. Mohr and Barry N. Taylor. CODATA recommended values of the fundamental physical constants: 1998. *Rev. Mod. Phys.*, **72**, 351495 (2000).

[2] M. H. Anderson, J .R. Ensher, M. R. Matthews, C. E. Wieman and E. A. Cornell. Observation of Bose-Einstein condensation in a dilute atomic vapor. *Science*, **269**, 198 (1995).

[3] K.B. Davis, M.-O. Mewes, M.R. Andrews, N.J. van Druten, D.S. Durfee, D.M Kurn and W. Ketterle. Bose-Einstein condensation in a gas of sodium atoms. *Phys. Rev. Lett.*, **75**, 3969 (1995).

[4] C. C. Bradley, C. A. Sackett, J. J. Tollett and R. G. Hulet. Evidence of Bose-Einstein condensation in an atomic gas with attractive interactions. *Phys. Rev. Lett.*, **75**, 1687 (1995).

[5] M. R. Andrews, C. G. Townsend, H.-J. Miesner, D. S. Durfee, D. M. Kurn and W. Ketterle. Observation of interference between two Bose condensates. *Science*, **275**, 637 (1997).

[6] M.-O. Mewes, M. R. Andrews, D. M. Kurn, D. S. Durfee, C. G. Townsend and W. Ketterle. Output coupler for Bose-Einstein condensed atoms. *Phys. Rev. Lett.*, **78**, 582 (1997).

[7] D. M. Harber, J. M. Obrecht, J. M. McGuirk and E. A. Cornell. Measurement of the Casimir-Polder force through center-of-mass oscillations of a Bose-Einstein condensate. *Phys. Rev. A*, **72**, 033610 (2005).

[8] Markus Greiner, Cindy A. Regal and Deborah S. Jin. Fermionic condensates. In *Atomic Physics 19: XIX International Conference on Atomic Physics; ICAP 2004*, pages 209–217 (2004).

[9] E. A. Hinds and I. G. Hughes. Magnetic atom optics, mirrors, guides, traps and chips for atoms. *J. Phys. D, Appl. Phys.*, **32**, R119 (1999).

[10] Ron Folman, Peter Krüger, Jörg Schmiedmayer, Johannes Denschlag and Carsten Henkel. Microscopic atom optics: From wires to an atom chip. *Adv. At. Mol. Opt. Phys.*, **48**, 236 (2002).

[11] T. Calarco, E. A. Hinds, D. Jaksch, J. Schmiedmayer, J. I. Cirac and P. Zoller. Quantum gates with neutral atoms: Controlling collisional interactions in time-dependent traps. *Phys. Rev. A*, **61**, 022304 (2000).

[12] Peter Horak, Bruce G. Klappauf, Albrecht Haase, Ron Folman, Joerg Schmiedmayer, Peter Domokos and E. A. Hinds. Possibility of single-atom detection on a chip. *Phys. Rev. A*, **67**, 043806 (2003).

[13] E. A. Hinds, C. J. Vale and M. G. Boshier. Two-wire waveguide and interferometer for cold atoms. *Phys. Rev. Lett.*, **86**, 1462 (2001).

[14] W. Hänsel, J. Reichel, P. Hommelhoff and T. W. Hänsch. Trapped-atom interferometer in a magnetic microtrap. *Phys. Rev. A*, **64**, 063607 (2003).

[15] J. Reichel. Microchip traps and Bose Einstein condensation. *Appl. Phys. B*, **74**, 469 (2002).

[16] W. Hänsel, P. Hommelhoff and J. Reichel. Bose-Einstein condensation on a microelectronic chip. *Nature*, **413**, 498 (2001).

[17] H. Ott, J. Fortágh, G. Schlotterbeck, A. Grossmann and C. Zimmermann. Bose-Einstein condensation in a surface microtrap. *Phys. Rev. Lett.*, **87**, 230401 (2001).

[18] S. Schneider, A. Kasper, Ch. vom Hagen, M. Bartenstein, B. Engeser, T. Schumm, I. Bar-Joseph, R. Folman, L. Feenstra and J. Schmiedmayer. Bose-Einstein condensation in a simple microtrap. *Phys. Rev. A*, **67**, 023612 (2003).

[19] M. P. A. Jones, C. J. Vale, D. Sahagun, B. V. Hall and E. A. Hinds. Spin coupling between cold atoms and the thermal fluctuations of a metal surface. *Phys. Rev. Lett.*, **91**, 080401 (2003).

[20] A. E. Leanhardt, Y. Shin, A. P. Chikkatur, D. Kielpinski, W. Ketterle and D. E. Pritchard. Bose-Einstein condensates near a microfabricated surface. *Phys. Rev. Lett.*, **90**, 100404 (2003).

[21] Y. J. Lin, Igor Teper, Cheng Chin and Vladan Vuletić. Impact of the Casimir-Polder potential and Johnson noise on Bose-Einstein condensate stability near surfaces. *Phys. Rev. Lett.*, **92**, 050404 (2004).

[22] C. J. Vale, B. Upcroft, M. J. Davis, N. R. Heckenberg and H. Rubinsztein-Dunlop. Foil-based atom chip for Bose-Einstein condensates. *J. Phys. B: At. Mol. Opt. Phys.*, **37**, 2959 (2004).

[23] Ying-Ju Wang, Dana Z. Anderson, Victor M. Bright, Eric A. Cornell, Quentin Diot, Tetsuo Kishimoto, Mara Prentiss, R. A. Saravanan, Stephen R. Segal and Saijun Wu. Atom michelson interferometer on a chip using a Bose-Einstein condensate. *Phys. Rev. Lett.*, **94**, 090405 (2005).

[24] Shengwang Du, Matthew B. Squires, Yutaka Imai, Leslie Czaia, R. A. Saravanan, Victor Bright, Jakob Reichel, T. W. Hänsch and Dana Z. Anderson. Atom-chip Bose-Einstein condensation in a portable vacuum cell. *Phys. Rev. A*, **70**, 053606 (2004).

[25] W. Hänsel, J. Reichel, P. Hommelhoff and T.W. Hänsch. Magnetic conveyor belt for transporting and merging trapped atom clouds. *Phys. Rev. Lett.*, **86**, 608 (2001).

[26] H. Ott, J. Fortágh, S. Kraft, A. Günther, D. Komma and C. Zimmermann. Nonlinear dynamics of a Bose-Einstein condensate in a magnetic waveguide. *Phys. Rev. Lett.*, **91**, 040402 (2003).

[27] Svenja Knappe, Vishal Shah, Peter D. D. Schwindt, Leo Hollberg, John Kitching, Li-Anne Liew and John Moreland. A microfabricated atomic clock. *Appl. Phys. Lett*, **85**, 1460 (2004).

[28] Peter D. D. Schwindt, Svenja Knappe, Vishal Shah, Leo Hollberg and John Kitching. Chip-scale atomic magnetometer. *Appl. Phys. Lett*, **85**, 6409 (2004).

[29] T. Schumm, S. Hofferberth, L. M. Andersson, S. Wildermuth, S. Groth, I. Bar-Joseph, J. Schmiedmayer and P. Krüger. Matter-wave interferometry in a double well on an atom chip. *Nature Phys.*, **1**, 57 (2005).

[30] J. Fortágh, H. Ott, S. Kraft and C. Zimmermann. Surface effects on a Bose-Einstein condensate on a magnetic microtrap. *Phys. Rev. A*, **66**, 041604(R) (2002).

[31] D. M. Harber, J. M. McGuirk, J. M. Obrech and E. A. Cornell. Thermally induced losses in ultra-cold atoms magnetically trapped near room-temperature surfaces. *J. Low. Temp. Phys.*, **133**, 229 (2003).

[32] M. P. A. Jones, C. J. Vale, D. Sahagun, B. V. Hall, C. C. Eberlein, B. E. Sauer, K. Furusawa, D. Richardson and E. A. Hinds. Cold atoms probe the magnetic field near a wire. *J. Phys. B: At. Mol. Opt. Phys.*, **37**, L15 (2004).

[33] S Kraft, A Günther, H Ott, D Wharam, C Zimmermann, and J Fortágh. Anomalous longitudinal magnetic field near the surface of copper conductors. *J. Phys. B: At. Mol. Opt. Phys.*, **35**, L469 (2002).

[34] J. Estève, C. Aussibal, T. Schumm, C. Figl, D. Mailly, I. Bouchoule, C. I. Westbrook and A. Aspect. Role of wire imperfections in micromagnetic traps for atoms. *Phys. Rev. A*, **70**, 043629 (2004).

[35] C. Henkel, S. Poetting and M. Wilkens. Loss and heating of particles in small and noisy traps. *Appl. Phys. B*, **69**, 379 (1999).

[36] Matthew P. A. Jones. *Bose-Einstein Condensation on an Atom Chip.* Ph.D. thesis, University of Sussex (2003).

[37] T. M. Roach, H. Abele, M. G. Boshier, H. L. Grossman, K. P. Zetie and E. A. Hinds. Realization of a magnetic mirror for cold atoms. *Phys. Rev. Lett.*, **75**, 629 (1995).

[38] I. G. Hughes, P. A. Barton, T. M. Roach, M. G. Boshier and E. A. Hinds. Atom optics with magnetic surfaces: I. storage of cold atoms in a curved 'floppy disk'. *J. Phys. B: At. Mol. Opt. Phys.*, **30**, 647 (1997).

[39] I. G. Hughes, P. A. Barton, T. M. Roach and E. A. Hinds. Atom optics with magnetic surfaces: II. microscopic analysis of the 'floppy disk' mirror. *J. Phys. B: At. Mol. Opt. Phys.*, **30**, 2119 (1997).

[40] C. V. Saba, P. A. Barton, M. G. Boshier, I. G. Hughes, P. Rosenbusch, B. E. Sauer and E. A. Hinds. Reconstruction of a cold atom cloud by magnetic focusing. *Phys. Rev. Lett.*, **82**, 468 (1999).

[41] P. Rosenbusch, B. V. Hall, I. G. Hughes, C. V. Saba and E. A. Hinds. Manipulation of cold atoms using a corrugated magnetic reflector. *Phys. Rev. A*, **61**, 031404(R) (2000).

[42] P. Rosenbusch, B.V. Hall, I.G. Hughes, C. V. Saba and E. A. Hinds. Manipulation of cold atoms by an adaptable magnetic reflector. *Appl. Phys. B*, **70**, 709 (2000).

[43] Benjamin Lev, Yves Lassailly, Chungsok Lee, Axel Scherer and Hideo Mabuchi. Atom mirror etched from a hard drive. *Appl. Phys. Lett.*, **83**, 395 (2003).

[44] D. C. Lau, R. J. McLean, A. I. Sidorov, D. S. Gough, J. Koperski, W. J. Rowlands, B. A. Sexton, G. I. Opat and P. Hannaford. Magnetic mirrors with micron-scale periodicities for slowly moving neutral atoms. *J. Opt. B*, **1**, 371 (1999).

[45] E. A. Hinds. Controlling cold atoms above a magnetic reflector. *Phil. Trans. Royal Soc. Lon. A*, **357**, 1409 (1999).

[46] L. Pricoupenko, H. Perrin and M. Olshanii, editors. *Quantum Gases in Low Dimensions J Phys IV (France)*, volume 116 (2004).

[47] Jocelyn A. Retter. *Cold Atom Microtraps above a Videotape Surface.* Ph.D. thesis, University of Sussex (2002).

[48] C. D. J. Sinclair, J. A. Retter, E. A. Curtis, B. V. Hall, I. Llorente Garcia, S. Eriksson, B. E. Sauer and E. A. Hinds. Cold atoms in videotape micro-traps. *Eur. Phys. J. D*, **35**, 105 (2005).

[49] I. Barb, R. Gerritsma, Y. T. Xing, J. B. Goedkoop and R. J. C. Spreeuw. Creating Ioffe-Pritchard micro-traps from permanent magnetic film with in-plane magnetization. *Eur. Phys. J. D*, **35**, 75 (2005).

[50] B.V. Hall, S. Whitlock, F. Scharnberg, P. Hannaford and A. Sidorov. A permanent magnetic film atom chip for Bose-Einstein condensation. *J. Phys. B: At. Mol. Opt. Phys.*, **39**, 27 (2005).

[51] S. A. Hopkins, E. A. Hinds and M. G. Boshier. UHV-compatible magnetic material for atom optics. *Appl. Phys. B*, **73**, 51 (2001).

[52] C. D. J. Sinclair, E. A. Curtis, I Llorente Garcia, J. A. Retter, B. V. Hall, S. Eriksson, B. E. Sauer and E. A. Hinds. Bose-Einstein condensation on a permanent-magnet atom chip. *Phys. Rev. A*, **72**, 031603(R) (2005).

[53] B.V. Hall, S. Whitlock, F. Scharnberg, P. Hannaford and A. Sidorov. Bose-Einstein condensates on a permanent magnetic film atom chip. arXiv:cond-mat/0509091 (2005).

[54] G. Breit and I.I. Rabi. Measurement of nuclear spin. *Phys. Rev.*, **38**, 2082 (1931).

[55] W. Ketterle, D. S. Durfee and D. M. Stamper-Kurn. Making, probing and understanding Bose-Einstein condensates. In M Inguscio, S. Stringari and C. E. Wieman, editors, *Bose-Einsten Condensation in Atomic Gases*, pages 66–176. OPS Press, Amsterdam (1999).

[56] John David Jackson. *Classical Electrodynamics*. John Wiley & Sons, Inc (1999).

[57] I.S. Gradshteyn and I.M. Ryzhik. *Table of Integrals, Series and Products*. Academic Press, Inc. (1965).

[58] David E. Pritchard. Cooling neutral atoms in a magnetic trap for precision spectroscopy. *Phys. Rev. Lett.*, **51** (1983).

[59] Kerson Huang. *Statistical Mechanics*. John Wiley & Sons (1963).

[60] Lev Pitaevskii and Sandro Stringari. *Bose-Einstein Condensation*. Clarendon Press (2003).

[61] Franco Dalfovo, Srefano Giorgini, Lev P. Pitaevskii and Sandro Stringari. Theory of Bose-Einstein condensation in trapped gases. *Rev. Mod. Phys.*, **71**, 463 (1999).

[62] C. J. Pethick and H. Smith. *Bose-Einstein Condensation in Dilute Gases*. Cambridge University Press (2002).

[63] Vanderlei Bagnato, David E. Pritchard and Daniel Kleppner. Bose-Einstein condensation in an external potential. *Phys. Rev. A*, **35**, 4354 (1987).

[64] N. J. van Druten and Wolfgang Ketterle. Two-step condensation of the ideal Bose gas in highly anisotropic traps. *Phys. Rev. Lett.*, **79**, 549 (1997).

[65] Gordon Baym and C. J. Pethick. Ground-state properties of magnetically trapped Bose-condensed rubidium gas. *Phys. Rev. Lett.*, **76**, 6 (1996).

[66] Y. Castin and R. Dum. Bose-Einstein condensates in time dependent traps. *Phys. Rev. Lett.*, **77**, 5315 (1996).

[67] Yu. Kagan, E. L. Surkov and G. V.Shlyapnikov. Evolution of a Bose gas in anisotropic time-dependent traps. *Phys. Rev. A*, **55**, R18 (1997).

[68] U. Ernst, J. Schuster, F. Schreck, A.Marte, A. Kuhn and G. Rempe. Free expansion of a Bose-Einstein condensate from an Ioffe-Pritchard magnetic trap. *Appl. Phys. B*, **67**, 719 (1998).

[69] C.E. Wieman and L. Hollberg. Using diode lasers for atomic physics. *Rev. Sci. Inst.*, **62**, 1 (1991).

[70] K.B. MacAdam, A. Steinbach and C Wieman. A narrow-band tunable diode laser system with grating feedback and a saturated absorption spectrometer for Cs and Rb. *Am. J. Phys.*, **60**, 1098 (1992).

[71] Wolfgang Demtröder. *Laser Spectroscopy.* Springer (2003).

[72] C. Wieman and T. W. Hänsch. Doppler-free laser polarization spectroscopy. *Phys. Rev. Lett.*, **36**, 1170 (1976).

[73] C.P. Pearman, C.S. Adams, S.G. Cox, P.F. Griffin, D.A. Smith and I.G. Hughes. Polarization spectroscopy of a closed atomic transition: applications to laser frequency locking. *J. Phys. B*, **35**, 5141 (2002).

[74] A.S. Arnold, J.S. Wilson and M.G. Boshier. A simple extended-cavity diode laser. *Rev. Sci Inst.*, **69**, 1236 (1998).

[75] U. Shcünemann, H. Engler, R. Grimm, M. Weidemüller and M. Zielonkowski. Simple scheme for tunable frequency offset locking of two lasers. *Rev. Sci. Inst.*, **70**, 242 (1999).

[76] Toptica Photonics, Frauunhoferstrasse 14 82152 Martinsreid/Germany. *DL100 Diode Laser System Manual* (August 2002).

[77] SAES Getters. *SAES Getters NEG Sorb-AC Manual.*

[78] Ken Arnold, James Gosling and David Holmes. *The Java Programming Language.* Addison-Wesley (1996).

[79] National Instruments. *NI-DAQ Function Reference Manual for PC Compatibles.*

[80] Kathy Walrath, Mary Campione, Alison Huml and Sharon Zakhour. *The JFC Swing Tutorial*. Addison-Wesley (2000).

[81] Peter Rosenbusch. *Atom Optics with an Adaptable Magnetic Reflector*. Ph.D. thesis, University of Sussex (2000).

[82] C. S. Adams and E. Riis. Laser cooling and trapping of neutral atoms. *Prog. Quant. Elec.*, **21**, 1 (1997).

[83] Harold J. Metcalf and Peter van Straten. *Laser Cooling and Trapping*. Springer (1999).

[84] Z.T. Lu, K.L. Corwin, M.J. Renn, M.H. Anderson, E.A. Cornell and C.E. Wieman. Low-velocity intense source of atoms from a magneto-optical trap. *Phys. Rev. Lett.*, **77**, 3331 (1996).

[85] J. Reichel, W. Hänsel and T.W. Hänsch. Atomic micromanipulation with magnetic surface traps. *Phys. Rev. Lett.*, **83**, 3398 (1999).

[86] William D. Phillips and Harold Metcalf. Laser deceleration of an atomic beam. *Phys. Rev. Lett.*, **48**, 596 (1982).

[87] Steven Chu, L. Hollberg, J. E. Bjorkholm, Alex Cable and A. Ashkin. Three-dimensional viscous confinement and cooling of atoms by resonance radiation pressure. *Phys. Rev. Lett.*, **55**, 48 (1985).

[88] E.L. Raab, M. Prentiss, A. Cable, S. Chu and D. Pritchard. Trapping of neutral sodium atoms with radiation pressure. *Phys. Rev. Lett.*, **59**, 2631 (1987).

[89] C. Monroe, W. Swann, H. Robinson and C. Wieman. Very cold atoms in a vapor cell. *Phys. Rev. Lett.*, **65**, 1571 (1990).

[90] R.N. Watts and C.E. Wieman. Manipulating atomic velocites using diode lasers. *Opt. Lett.*, **11**, 291 (1986).

[91] C. J. Myat, N. R. Newbury, R. W. Ghrist, S. Loutzenhiser and C. E. Wieman. Multiply loaded magneto-optical trap. *Opt. Lett.*, **21**, 290 (1996).

[92] J. Fortágh, A Grosman, T.W. Hänsch and C. Zimmerman. Fast loading of a magneto-optical trap from a pulsed thermal source. *J. Appl. Phys.*, **84**, 6499 (1998).

[93] Kai Dieckmann. *Bose-Einstein Condensation with High Atom Number in a Deep Magnetic Trap*. Ph.D. thesis, University of Amsterdam (2001).

[94] K. Dieckmann, R.J.C. Spreeuw, M. Weiemüller and J.T.M. Walvern. Two-dimensional magneto-optical trap as a source of slow atoms. *Phys. Rev. A*, **58**, 3891 (1998).

[95] Dirk Müller, Dana Z. Anderson, Randal J. Grow, Peter D. D. Schwindt and Eric A. Cornell. Guiding neutral atoms around curves with lithographically patterned current-carrying wires. *Phys. Rev. Lett.*, **83**, 5194 (1999).

[96] J.M. Vogels, T. Lahaye, C.F. Roos, J. Dalibard and D. Guéry-Odelin. How to reach the collisional regime on a magnetically guided atomic beam. In L. Pricoupenko, H. Perrin and M. Olshanii, editors, *J. Phys. IV France*, volume 116, pages 259–264 (2004).

[97] John H. Moore, Christopher C. Davis and Michael A. Coplan. *Building Scientific Apparatus*. Perseus Books (1991).

[98] Myung Sim Jun, Chang Yong Park and D. Cho. Low velocity intense source of rubidium atoms. *J. Kor. Phys. Soc.*, **33**, 260 (1998).

[99] L. Cacciapuoti, A. Castrillo, M. de Angelis and G. M. Tino. A continuous cold atomic beam from a magneto-optical trap. *Eur. Phys. J. D*, **15**, 245 (2001).

[100] Yuri B. Ovchinnikov. Compact magneto-optical sources of slow atoms. *Opt. Comm.*, **249**, 473 (2005).

[101] David S. Weiss, Erling Riis, Yaakov Shevey, Jeffery P. Ungar and Steven Chu. Optical molasses and multilevel atoms: experiment. *J. Opt. Soc. Am. B*, **6**, 2072 (1989).

[102] M. Arndt, M. Ben Dahn, Guéry-Odelin, M. W. Reynolds and J. Dalibard. Observation of a zero-energy resonance in Cs-Cs collisions. *Phys. Rev. Lett.*, **79**, 625 (1997).

[103] E. G. M. van Kempen, S. J. J. M. F. Kokkelmans, D. J. Heinzen and B. J. Verhaar. Interisotope determination of ultracold rubidium interactions from three high-precision experiments. *Phys. Rev. Lett.*, **88**, 093201 (2002).

[104] O. J. Luiten, M. W. Reynolds and J.T.M Walvern. Kinetic theory of the evaporative cooling of trapped gas. *Phys. Rev. A*, **53**, 381 (1996).

[105] K. B. Davis, M. O. Mewes and W. Ketterle. An analytical model for evaporative cooling of atoms. *Appl. Phys. B*, **60**, 155 (1995).

[106] W. Ketterle and N.J. van Druten. Evaporative cooling of trapped atoms. *Adv. At. Mol. Opt. Phys.*, **37**, 181 (1996).

[107] Aidan Arnold. *Preparation and Manipulation of a ^{87}Rb Bose-Einstein Condensate*. Ph.D. thesis, University of Sussex (1999).

[108] Rudolf Grimm, Matthias Weidemuller and Yurii B Ovchinnikov. Optical dipole traps for neutral atoms. *Adv. At. Mol. Opt. Phys.*, **42**, 95 (2000).

[109] David M. Harber. *Experimental investigation of interactions between ultracold atoms and room-temperature surfaces*. Ph.D. thesis, University of Colorado (2005).

[110] T. Schumm, J. Estève, C. Figl, J.-B. Trebbia, C. Aussibal, H. Nguyen, D. Mailly, I. Bouchoule, C.I. Westbrook and A. Aspect. Atom chips in the real world: the effects of wire corrugation. *Eur. Phys J. D*, **32**, 171 (2005).

[111] P. Krüger, L. M. Andersson, S. Wildermuth, S. Hofferberth, E. Haller, S. Aigner, S. Groth, I. Bar-Joseph and J. Schmiedmayer. Disorder potentials near lithographically fabricated atom chips. arXiv:cond-mat/0504686 (2005).

[112] S. Eriksson, F. Ramirez-Martinez, E. A. Curtis, B. E. Sauer, P. W. Nutter, E. W. Hill and E. A. Hinds. Micron-sized atom traps made from magneto-optical thin films. *Appl. Phys. B*, **79**, 811 (2004).

[113] A.E. Leanhardt, A.P. Chikkatur, D. Kielpinski, Y. Shin, T.L. Gustavson, W. Ketterle and D.E. Pritchard. Propagation of Bose-Einstein condensates in a magnetic waveguide. *Phys. Rev. Lett.*, **89**, 040401 (2002).

[114] P. K. Rekdal, S. Scheel, P. L. Knight and E. A. Hinds. Thermal spin flips in atom chips. *Phys. Rev. A*, **70**, 013811 (2004).

[115] S. Scheel, P. K. Rekdal, P. L. Knight and E. A. Hinds. Atomic spin decoherence near conducting and superconducting films. *Phys. Rev. A*, **72**, 042901 (2005).

[116] C. Henkel. Magnetostatic field noise near metallic surfaces. *Eur. Phys. J. D*, **35**, 59 (2005).

[117] V. Dikovsky, Y. Japha, C. Henkel and R. Folman. Reduction of magnetic noise in atom chips by material optimization. *Eur. Phys. J. D*, **35**, 87 (2005).

[118] J. E. Lye, L. Fallani, M. Modugno, D. S. Wiersma, C. Fort and M. Inguscio. Bose-Einstein condensate in a random potential. *Phys. Rev. Lett.*, **95**, 070401 (2005).

[119] David Clement, Andres F Varon, Mathilde Hugbart, Jocelyn Retter, Philippe Bouyer, Laurent Sanchez-Palencia, Dimitri M Gangardt, Georgy V Shlyapnikov and Alain Aspect. Suppression of transport of an interacting elongated Bose-Einstein condensate in a random potential. *Phys. Rev. Lett.*, **95**, 170409 (2005).

[120] S. Eriksson, M. Trupke, H. F. Powell, D. Sahagun, C. D. J. Sinclair, E. A. Curtis, B. E. Sauer, E. A. Hinds, Z. Maktadir, C. O. Gollasch and M. Kraft. Integrated optical components on atom chips. *Eur. J. Phys. D*, **35**, 135 (2005).

[121] M. Trupke, E. A. Hinds, S. Eriksson, E. A. Curtis, Z. Moktadir, E. Kukharenka and M. Kraft. Microfabricated high-finesse optical cavity with open access and small volume. *Appl. Phys. Lett.*, **87**, 211106 (2005).

[122] Markus Greiner, Olaf Mandel, Tilman Esslinger, Theodor W. Hänsch and Immanuel Bloch. Quantum phase transition from a superfluid to a Mott insulator in a gas of ultracold atoms. *Nature*, **415**, 39 (2002).

[123] S. Bize, Y. Sortais, M. S. Santos, C. Mandache, A. Clairon and C. Salomon. High-accuracy measurement of the ^{87}Rb ground-state hyperfine splitting in an atomic fountain. *Europhys. Lett.*, **45**, 558 (1999).

[124] Jun Ye, Steve Swartz, Peter Jungner and John L. Hall. Hyperfine structure and absolute frequency of the ^{87}Rb $5P_{3/2}$ state. *Opt. Lett.*, **21**, 1280 (1996).